JOURNAL OF COMPUTATIONAL PHYSICS **131,** 109–148 (1997)
ARTICLE NO. CP965581

Microstructural Evolution in Inhomogeneous Elastic Media

H.-J. Jou,* P. H. Leo,† and J. S. Lowengrub‡

*Division of Engineering, Colorado School of Mines, Golden, Colorado 80401; †Department of Aerospace Engineering and Mechanics, University of Minnesota, Minneapolis, Minnesota 55455; ‡School of Mathematics, University of Minnesota, Minneapolis, Minnesota 55455
E-mail: lowengrb@math.umn.edu

Received August 25, 1995; revised July 2, 1996

We simulate the diffusional evolution of microstructures produced by solid state diffusional transformations in elastically stressed binary alloys in two dimensions. The microstructure consists of arbitrarily shaped precipitates embedded coherently in an infinite matrix. The precipitate and matrix are taken to be elastically isotropic, although they may have *different* elastic constants (elastically inhomogeneous). Both far-field applied strains and mismatch strains between the phases are considered. The diffusion and elastic fields are calculated using the boundary integral method, together with a small scale preconditioner to remove ill-conditioning. The precipitate–matrix interfaces are tracked using a nonstiff time updating method. The numerical method is spectrally accurate and efficient. Simulations of a single precipitate indicate that precipitate shapes depend strongly on the mass flux into the system as well as on the elastic fields. Growing shapes (positive mass flux) are dendritic while equilibrium shapes (zero mass flux) are squarish. Simulations of multiparticle systems show complicated interactions between precipitate morphology and the overall development of microstructure (i.e., precipitate alignment, translation, merging, and coarsening). In both single and multiple particle simulations, the details of the microstructural evolution depend strongly on the elastic inhomogeneity, misfit strain, and applied fields.

1. INTRODUCTION

In this paper, we simulate the diffusional evolution of microstructures produced by solid state diffusional transformations in elastically stressed binary alloys. Many important structural materials such as steel, aluminum, and nickel-based alloys are products of solid state diffusional transformations. These transformations occur when a thermodynamically stable mixture of solids is driven from equilibrium by a sudden lowering of temperature. The system re-equilibrates by nucleating second phase precipitates which then evolve diffusionally until the process either reaches equilibrium or is stopped by quenching. This diffusional evolution consists of two distinct phases—growth and equilibration. Growth occurs to satisfy a *local* mass balance relation at each precipitate interface. Equilibration occurs when a *global* mass balance is achieved and involves a dynamic rearrangement of mass in the system so as to minimize a global energy. The diffusional evolution produces a detailed arrangement of distinct constituents at the microscopic level which is referred to as microstructure. The details of the microstructure greatly influence the material properties of the alloy (i.e., stiffness, strength, and toughness).

Experimental observations of these microstructures, especially in nickel-based superalloys, indicate that the equilibria and kinetics of their diffusional evolution can be influenced (and controlled) by elastic effects as well as by surface energy and nucleation density effects [4, 9, 36, 39, 50, 57]. For example, equilibrium microstructures in these alloys often take the form of cuboidal precipitates aligned in precise crystallographic directions, consistent with minimizing a global energy functional involving the sum of the elastic and surface energies of the system. These microstructures may be altered by applying loads to the system during the transformation. Recent experiments indicate that precipitate shapes and alignment depend strongly on the nucleation density of precipitates, that is, the number of precipitates in a small region of the alloy (number density). At low nucleation densities there is a relatively large mass flux to each individual precipitate, while at high nucleation densities the mass flux to each precipitate becomes vanishingly small. The experiments show that in the low nucleation density (large mass flux) regime, precipitates tend to have dendritic shapes. In contrast, for high nucleation densities (small mass flux), precipitates tend to have cuboidal shapes [57].

From an engineering point of view, one of the most important problems in alloy production is to understand how to dynamically stabilize a microstructure during the equilibration process. Typically during equilibration, the mass of small precipitates is diffused to large precipitates leading to a monodisperse microstructure consisting of a few large precipitates. This is referred to as coarsening or Ostwald ripening [52]. The subsequent decrease in number density of precipitates can lead to the failure of the material. One such place this can occur is in alloys used in the turbine blades of jet engines. There, the high temperatures and stresses can lead to coarsening and a catastrophic failure of the blades. It is hoped that elastic effects will provide

0021-9991/97 $25.00

a stabilizing mechanism against such a severe decrease in precipitate number density. Theoretically this is possible because elasticity influenced coarsening may not favor the largest precipitates. Ideally, one would like to understand the situations where a microstructure consisting of many, nearly equally sized particles is energetically favorable over a microstructure consisting of one or a few large particles. In part, we view our work as a step towards understanding such processes.

The particular problem we consider in this paper is that of the development of a two-phase microstructure in a two-dimensional binary alloy. The microstructure consists of arbitrarily shaped precipitates growing diffusionally in an elastically stressed matrix. The precipitate–matrix interfaces are assumed to be coherent with isotropic surface energy. Diffusion of the solute is taken to occur in the matrix only and is assumed to be quasi-static so that the mass composition of the diffusing species in the matrix phase obeys Laplace's equation. Both the precipitate and matrix are taken to be elastically isotropic, although they may have *different* elastic constants (elastically inhomogeneous). Elastic stresses may be generated by either far-field applied strains or by mismatch strains between the phases. The elasticity and composition fields are assumed to interact through an elastic energy term in a generalized Gibbs–Thomson boundary condition for the composition field. This implies that the atomic volumes of the two chemical species in the alloy are the same, so that both stress generated by compositional inhomogeneity and diffusion fluxes generated by varying stress fields are negligible.

The evolution of microstructure is studied by first computing the elastic fields. These are then used to obtain the generalized Gibbs–Thomson boundary condition for the composition in the matrix at the precipitate–matrix interface. With this information, the diffusion field in the matrix is computed and the normal velocity of each precipitate–matrix interface is found through a flux balance at that interface. The interfacial positions are updated and the process is repeated. We model the effect of nucleation density and, hence, the difference between growth and equilibration, by allowing for an arbitrary flux of mass into the system. Growth is modeled using a positive mass flux and equilibration is modeled using a zero mass flux.

Both the diffusion and elasticity problems for a multiphase system are reformulated in terms of boundary integral equations. The integral equations for the diffusion problem are obtained by using a modified dipole formulation [38]. This results in a second kind Fredholm equation for each interface, which is solved by using the techniques of Greenbaum, Greengard, and McFadden [11].

The inhomogeneous elasticity problem is much more difficult to solve. A direct boundary integral representation involving both monopoles and dipoles is used for the elastic fields. Integral equations are obtained for each interface by using the coherency conditions at the interface, i.e., continuity of both displacements and tractions. These integral equations, unlike those for diffusion, are not Fredholm as they involve Cauchy, logarithmic, and smooth kernels. This leads to a discretized linear system that is ill-conditioned. We treat this problem by developing a preconditioning scheme based on an explicit small scale decomposition of the integral equations to remove the ill-conditioning.

Finally, the solutions of the diffusion and elasticity problems are used to calculate the normal velocity of the precipitate–matrix interfaces. The resulting motion of the interfaces is tracked by using a nonstiff method developed by Hou, Lowengrub, and Shelley [17].

Previous work on simulating the evolution of two phase microstructures has followed two approaches based on whether the precipitate–matrix interfaces are treated as sharp or smooth. In the sharp interface approach (which is followed here) the equations describing the motion of the interface (see Section 2) are solved numerically and the interface motion is tracked [1, 22–24, 20, 46–48, 52, 53]. The smooth interface approach removes the need to track interfaces by relying on a set of mesoscopic field equations designed to mimic the diffusion and elasticity field equations [27, 37, 54, 56, 32, 31].

The smooth interface approach is very successful at simulating microstructures with large numbers of particles and at capturing topological transitions, such as particle merging, splitting, and vanishing. However, the results appear to be sensitive to the parameters that determine the thickness of the interfacial regions and so they cannot be easily reconciled with sharp interfaces.

In contrast, the sharp interface approach cannot straightforwardly handle topological transitions. However, the advantage of this approach is that the field equations, the boundary conditions and interfacial motion are formulated exactly. Moreover, the boundary integral formulation (BIF) reduces the dimensionality of the problem. As a consequence, in theory the BIF is more efficient than other methods where the fields are solved everywhere throughout the domain.

In practice, the numerical implementation of the BIF is made difficult by the complicated structure of the equations for the elastic fields *and* the presence of high order time step stability constraints (stiffness) that arise when interfaces with surface tension are tracked. In fact, until this paper, the BIF has been limited to simulating elastically anisotropic, but homogeneous, systems consisting of relatively few (less than five) particles. Homogeneous elastic systems are easier to treat than inhomogeneous systems because in the homogeneous case the elastic fields can be determined by evaluating an integral [53]. In contrast, in inhomogeneous systems, the elastic fields require the solu-

tion of integral equations. Further, the stiffness associated with interface tracking has led some investigators [49] to develop an iterative approach to determine equilibrium morphologies without recourse to dynamics. Alternatively, some researchers have simplified the dynamics by constraining the precipitate shapes to be circles [24, 2, 1, 15]. Our results indicate that such a shape constraint may be unreasonably severe.

By removing the stiffness and using efficient and accurate methods to compute the diffusion and isotropic elastic fields, we can overcome the difficulties usually associated with the BIF and *include* elastic inhomogeneities. This allows us to study the effect of elastic inhomogeneities on microstructural evolution and to simulate many more precipitates than has previously been possible. This is the first time, to our knowledge, that the inhomogeneous elasticity problem has been solved in arbitrary geometries for isotropic elasticity. Solutions in special geometries, of course, have been obtained previously (see, for example, [41, 14]). The implementation of both elastic inhomogeneity *and* anisotropy is more difficult, although it should be possible in our general framework.

The paper is organized as follows. In Section 2 the governing equations for diffusion and elasticity are presented. In addition, a boundary integral representation for the system energy is derived and the tangent angle formulation of interface motion in the scaled arclength frame is presented. In Section 3 a small-scale analysis of both the diffusion and elasticity integral equations is performed. In Section 4 the numerical implementation of the model is given, including the discretization and the preconditioning based on the small-scale analysis. In Section 5 the effectiveness of the preconditioner is demonstrated and numerical tests confirming the convergence of the scheme are given. In Section 6 some numerical results are given. Finally, in Section 7 some conclusions are made.

2. FORMULATION

In this section, the field equations for the diffusion and elasticity problems are presented and reformulated as boundary integral equations. A boundary integral representation for the total energy of the system and its time derivative is given. Also, the motion of the interface boundaries in the scaled arclength frame is given.

For both the diffusion and elasticity problems, the matrix and precipitate phases occupy the two-dimensional plane R^2; see Fig. 1. The matrix phase Ω^M extends to infinity, while the precipitate phase Ω^P consists of p separate particles occupying a finite area. The interface between the two phases consists of p disjoint closed curves, Γ_i, $i = 1 \cdots p$, with $\Gamma = \bigcup_{i=1}^{p} \Gamma_i$ denoting the whole interface. Each Γ_i is assumed smooth and the unit normal vector n on each interface is defined such that it is the outward normal for the precipitates and the inward normal for the matrix; see Fig. 1. Also, it is convenient to take a circular far boundary Γ_∞ with radius R_∞ and inward normal n that encloses all the precipitates. This boundary is fictitious and appears in the problem formulation only in the limit $R_\infty \to \infty$.

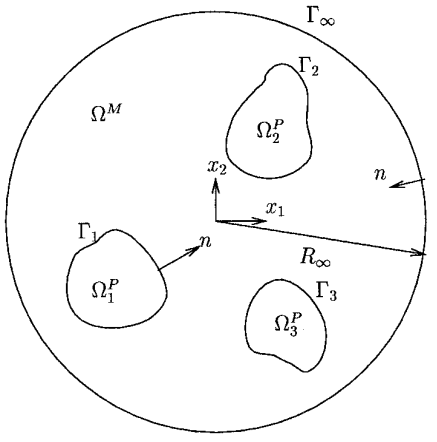

FIG. 1. A two-phase domain with three precipitates ($p = 3$).

In what follows, we work entirely in dimensionless variables. See Appendix A for the nondimensionalization.

2.1. Diffusion and Problem Specification

Let U be the composition field of the diffusing species in the matrix phase. It is assumed that the evolution of the precipitates is quasi-static, and so U obeys Laplace's equation,

$$\nabla^2 U = 0 \quad \text{in } \Omega^M. \tag{2.1}$$

This composition field is subject to both a boundary condition on the Γ_k and a far-field condition. The boundary condition is taken to be a generalized Gibbs–Thomson equation, as derived by Larché and Cahn [29, 30], Johnson and Alexander [21], and Leo and Sekerka [34, 35], among others. The condition is

$$U = \kappa + ZG^{\text{el}} \quad \text{on } \Gamma. \tag{2.2}$$

Here, κ is the mean curvature and Z is a parameter that characterizes the relative contribution of the elastic and surface energies. G^{el}, given in Eq. (2.13), is a local elastic energy density that must be found from the elastic fields. Roughly speaking, this boundary condition reflects the idea that changing the shape of a precipitate changes the energy of the system both through the additional surface area, κ, and also through the change in elastic energy of the system, ZG^{el}.

Because both growth and equilibration of the system of precipitates are to be considered, the far-field condition is taken to be

$$\lim_{R_\infty \to \infty} \int_{\Gamma_\infty} (-\nabla U \cdot n)\, ds = 2\pi J, \tag{2.3}$$

where s is arclength and $2\pi J$ is the total external mass flux supplied. The mass flux will be taken to be positive for growth conditions and zero for equilibration. Finally, the motion of the interfaces is determined from a mass balance on each interface,

$$V_i = (\nabla U \cdot n)|_{\Gamma_i}, \tag{2.4}$$

where V_i is the normal velocity of the interface Γ_i.

Equations (2.1)–(2.4) specify an exterior diffusion problem with Dirichlet boundary conditions in a multiply-connected domain. To complete the specification of the problem, we need to obtain G^{el} and update the positions of the interfaces. The calculation of G^{el} is addressed in Section 2.2 while the motion of the interfaces is discussed in Section 2.4.

2.1.1. *Boundary Integral Formulation for Diffusion*

Equations (2.1)–(2.4) can be formulated in terms of boundary integrals as follows. Let the composition field be $U = U(z)$, where $z = x_1 + ix_2$ is the complex position in the matrix. Following Mikhlin [38], introduce a dipole density ϕ on Γ, p source terms $A_1, ..., A_p$, and write $U(z)$ as

$$\begin{aligned} U(z) = \frac{1}{2\pi} \int_\Gamma \phi(s') \left[\frac{\partial}{\partial n(s')} \ln|z(s') - z| + 1 \right] ds' \\ + \sum_{k=1}^{p} A_k \ln|z - S_k|, \quad z \in \Omega^M, \end{aligned} \tag{2.5}$$

where $n(s')$ is the unit normal at the integration point $z(s')$, s' is the arclength along Γ, and $S_k = x^s_{1k} + ix^s_{2k}$ is a point inside the closed curve Γ_k. The representation (2.5) automatically satisfies Eq. (2.1). Further, letting $z \to z(s) \in \Gamma$ and using the boundary condition (2.2) and far-field flux condition (2.3) leads immediately to the set of boundary integral equations

$$\mathscr{A}[\phi, A_1, ..., A_p] = b, \tag{2.6}$$

where $\mathscr{A} = (\mathscr{A}_1, \mathscr{A}_2, \mathscr{A}_{3,1}, ..., \mathscr{A}_{3,p-1})$ and the right-hand side vector b are given by

$$\begin{aligned} \mathscr{A}_1[\phi, A_1, ..., A_p] = \left(-\frac{1}{2} I + K \right) [\phi] \\ + \sum_{k=1}^{p} A_k \log|z(s,t) - S_k| \end{aligned} \tag{2.7}$$

$$\mathscr{A}_2[\phi, A_1, ..., A_p] = \sum_{k=1}^{p} A_k \tag{2.8}$$

$$\mathscr{A}_{3,j}[\phi, A_1, ..., A_p] = \int_{\Gamma_j} \phi(s', t)\, ds' \quad \text{for } j = 1, ..., p-1 \tag{2.9}$$

$$b = (\kappa + ZG^{\mathrm{el}}, J, 0, ..., 0). \tag{2.10}$$

See [11, 38] for details. The K in Eq. (2.7) denotes the integral operator

$$\begin{aligned} K[\phi](s,t) = \frac{1}{2\pi} \int_\Gamma \phi(s', t) \\ \left[\frac{\partial}{\partial n(s', t)} \log|z(s', t) - z(s, t)| + 1 \right] ds'. \end{aligned} \tag{2.11}$$

The system (2.6) is invertible [38] and so the unknown quantities ϕ and A_k can be determined uniquely once G^{el} is found. Since the integral kernel of K is smooth, the system (2.6) is a modified second-kind Fredholm equation. The modification to the usual second-kind structure is due to the sources A_k. If this system is discretized, one finds that the condition number of the discretized system increases as p increases, but is essentially independent of N, the total number of grid points [11]. Thus, we say that (2.6) is ill-conditioned with respect to p. We note that the condition number also increases as the minimum distance between precipitates decreases (precipitate merging) and as the area of the smallest precipitate decreases (precipitate vanishing). In Section 3.1, the system is reformulated using a small scale decomposition to remove the ill-conditioning with respect to p. The ill-conditioning with respect to precipitate merging and vanishing is not ameliorated by the reformulation and is inherent in the boundary integral formulation.

Finally, given the solution to (2.6), the normal velocity V_i on each Γ_i is calculated by using the Dirichlet–Neumann map,

$$\begin{aligned} V_i(s) = \frac{1}{2\pi} \int_\Gamma \phi_{,s'} \frac{\partial}{\partial s} \log|z(s') - z(s)|\, ds' \\ + \sum_{k=1}^{p} A_k \frac{(x_1(s) - x^s_{1k}) x_{2,s} - (x_2(s) - x^s_{2k}) x_{1,s}}{(x_1(s) - x^s_{1k})^2 + (x_2(s) - x^s_{2k})^2}, \end{aligned} \tag{2.12}$$

with $V_i(s) = V_i(z(s))$, $\phi_{,s'} = \partial\phi(s')/\partial s'$, $x_{j,s} = \partial x_j(s)/\partial s$ for $j = 1, 2$ and $z(s) \in \Gamma_i$. The integral is interpreted as a principal value integral because of the Cauchy singularity

of $(\partial/\partial s)\log|z(s') - z(s)|$ when both $z(s), z(s') \in \Gamma_i$. See [11], for example.

2.2. Elasticity

As we have seen, the solution to the diffusion problem requires that one first calculate the term G^{el} that enters the boundary condition (2.2). On Γ, G^{el} is given by

$$G^{\mathrm{el}} = \tfrac{1}{2}\sigma_{ij}^{\mathrm{P}}(\varepsilon_{ij}^{\mathrm{P}} - \varepsilon_{ij}^{\mathrm{T}}) - \tfrac{1}{2}\sigma_{ij}^{\mathrm{M}}\varepsilon_{ij}^{\mathrm{M}} + \sigma_{ij}^{\mathrm{M}}(\varepsilon_{ij}^{\mathrm{M}} - \varepsilon_{ij}^{\mathrm{P}}).^{1} \tag{2.13}$$

See [34] or the references below for a derivation. Here, ε_{ij} and σ_{ij} are the strains and stresses in the matrix (superscript "M") and precipitate (superscript "P") and $\varepsilon_{ij}^{\mathrm{T}}$ is the transformation (misfit) strain of the precipitate. The transformation strain arises because the crystal lattice of the precipitate is different, in general, from that of the matrix. G^{el} is closely related to the energy momentum tensor introduced by Eshelby [10]. G^{el} can also be found from variational models of crystal–crystal equilibrium [29, 21, 35].

The calculation of G^{el} requires a full solution to the two-phase elasticity problem for the domain shown in Fig. 1. This problem is specified as follows. Both the precipitate and matrix phases are taken to be linear elastic and isotropic, although with different elastic constants. Taking the misfit strain into account, the constitutive equation for the precipitate is given by

$$\sigma_{ij}^{\mathrm{P}} = C_{ijkl}^{\mathrm{P}}(\varepsilon_{kl}^{\mathrm{P}} - \varepsilon_{kl}^{\mathrm{T}}), \tag{2.14}$$

whereas that for the matrix is given by

$$\sigma_{ij}^{\mathrm{M}} = C_{ijkl}^{\mathrm{M}}\varepsilon_{kl}^{\mathrm{M}}. \tag{2.15}$$

Implicit in this choice is that the reference state is taken to be the unstressed lattice of the matrix so that the transformation strain $\varepsilon_{ij}^{\mathrm{T}}$ maps the unstressed precipitate lattice to that of the matrix.

The strains ε_{ij} are calculated from the displacement u_i by the kinematic equation

$$\varepsilon_{ij}^{\chi} = \tfrac{1}{2}[u_{i,j}^{\chi} + u_{j,i}^{\chi}] \tag{2.16}$$

for χ either "P" or "M." A consequence of isotropy is that the stiffness tensor C_{ijkl} is given by

$$C_{ijkl}^{\chi} = 2\mu^{\chi}\left[\frac{\nu^{\chi}}{1-2\nu^{\chi}}\delta_{kl}\delta_{ij} + \delta_{ik}\delta_{jl}\right], \tag{2.17}$$

where $\mu^{\mathrm{M}} = 1$ and μ^{P} are the dimensionless shear moduli (see Appendix A), ν^{M} and ν^{P} are the Poisson ratios, and δ_{ij} is the Kronecker delta.

The field equations for elasticity are

$$\sigma_{ij,j}^{\chi} = 0 \quad \text{in } \Omega^{\chi} \tag{2.18}$$

in the absence of body forces. The boundary conditions at the precipitate–matrix interfaces are those appropriate to a coherent interface, i.e., continuity of displacement across the interface,

$$u_i^{\mathrm{P}} = u_i^{\mathrm{M}} \quad \text{on } \Gamma, \tag{2.19}$$

and continuity of traction across the interface

$$t_i^{\mathrm{P}} = \sigma_{ij}^{\mathrm{P}}n_j = \sigma_{ij}^{\mathrm{M}}n_j = t_i^{\mathrm{M}} \quad \text{on } \Gamma. \tag{2.20}$$

The far-field condition is

$$\lim_{r\to\infty}\varepsilon_{ij}^{\mathrm{M}} = \varepsilon_{ij}^{0}, \tag{2.21}$$

where ε_{ij}^{0} is the applied far-field strain. Last, the displacement in each precipitate is assumed to be bounded. Equations (2.14)–(2.21) define an inhomogeneous two-phase elasticity problem for precipitate domains of arbitrary shape.

In the next section, we will present the boundary integral reformulation of Eqs. (2.14)–(2.21). Special care will be taken to properly include misfit strains in the precipitate and applied strains in the matrix. Further, the displacement at infinity will be specified, guaranteeing the uniqueness of solutions to (2.14)–(2.21).

2.2.1. *Boundary Integral Formulation*

In this section, we derive the boundary integral equations for the elastic fields using the weighted residual method [7] and the continuity conditions across Γ. Other approaches using Goursat functions [38] could certainly be adapted to this problem; however, because of the coherent boundary conditions, we believe that the approach presented here is the most natural.

Precipitate. Write Eq. (2.18) in an integral form by multiplying $\sigma_{kj,j}^{\mathrm{P}} = 0$ by a test function $u_k^{\mathrm{P}*}$ and integrating over Ω_i^{P}, the region occupied by the ith precipitate. This gives

$$\int_{\Omega_i^{\mathrm{P}}}\sigma_{kj,j}^{\mathrm{P}}u_k^{\mathrm{P}*}\,da = 0. \tag{2.22}$$

Integrating by parts twice, using the divergence theorem and Eqs. (2.14) and (2.16), yields

[1] Einstein summation convention is used throughout the paper, with indices running from 1 to 2.

$$\int_{\Omega_i^{\mathrm{P}}} u_k^{\mathrm{P}} \sigma_{kj,j}^{\mathrm{P}*}\, da + \int_{\Gamma_i} (t_k^{\mathrm{P}} + t_k^{\mathrm{T}}) u_k^{\mathrm{P}*}\, ds = \int_{\Gamma_i} t_k^{\mathrm{P}*} u_k^{\mathrm{P}}\, ds, \quad (2.23)$$

where $\sigma_{kj}^{\mathrm{P}*} = C_{kjlm}^{\mathrm{P}} \varepsilon_{lm}^{\mathrm{P}*} = C_{kjlm}^{\mathrm{P}} u_{l,m}^{\mathrm{P}*}$. Further, $t_k^{\mathrm{P}} = \sigma_{kj}^{\mathrm{P}} n_j$, $t_k^{\mathrm{T}} = \sigma_{kj}^{\mathrm{T}} n_j = C_{kjlm}^{\mathrm{P}} \varepsilon_{lm}^{\mathrm{T}} n_j$, and $t_k^{\mathrm{P}*} = \sigma_{kj}^{\mathrm{P}*} n_j$ are the appropriate surface tractions. The function $u_k^{\mathrm{P}*}$ is then chosen to be the fundamental solution (Kelvin's solution) to the PDE

$$\sigma_{lj,j}^{\mathrm{P}*} + \delta(z) e_l = 0, \quad z \in \Omega_i^{\mathrm{P}},$$

where e_l is an arbitrary unit direction and $\delta(z)$ is a Dirac delta function at z. The displacement $u_k^{\mathrm{P}*}$ and traction $t_k^{\mathrm{P}*}$ are given in terms of the fundamental solutions $u_{lk}^{\mathrm{P}*}$ and $t_{lk}^{\mathrm{P}*}$ by $u_k^{\mathrm{P}*} = u_{lk}^{\mathrm{P}*} e_l$ and $t_k^{\mathrm{P}*} = t_{lk}^{\mathrm{P}*} e_l$, where

$$\begin{aligned} u_{lk}^{\mathrm{P}*}(z, z') &= \frac{1}{8\pi\mu^{\mathrm{P}}(1-\nu^{\mathrm{P}})}\left[(3-4\nu^{\mathrm{P}}) \ln\left(\frac{1}{r}\right)\delta_{lk} + r_{,l'} r_{,k'}\right] \\ t_{lk}^{\mathrm{P}*}(z, z') &= \frac{-1}{4\pi(1-\nu^{\mathrm{P}})r}\left[\frac{\partial r}{\partial n'}\left((1-2\nu^{\mathrm{P}})\delta_{lk} + 2 r_{,l'} r_{,k'}\right)\right. \\ &\quad \left. + (1-2\nu^{\mathrm{P}})(n_l' r_{,k'} - n_k' r_{,l'})\right], \end{aligned} \quad (2.24)$$

with $r = |z' - z|$, $r_{,k'} = \partial r / \partial x_k'$, and $n_k' = n_k(s')$. See Brebbia [7] for details. Using these choices, Eq. (2.23) becomes

$$\begin{aligned} u_l^{\mathrm{P}}(z) + \int_{\Gamma_i} u_k^{\mathrm{P}}(z(s')) t_{lk}^{\mathrm{P}*}(z, z(s'))\, ds' &= \int_{\Gamma_i} (t_k^{\mathrm{P}}(z(s')) \\ + t_k^{\mathrm{T}}(z(s'))) u_{lk}^{\mathrm{P}*}(z, z(s'))\, ds', &\quad z \in \Omega_i^{\mathrm{P}}. \end{aligned} \quad (2.25)$$

Equation (2.25) is simply a potential formulation for u_l^{P} with displacement serving as the dipole density and surface traction as the monopole density. A boundary integral equation is derived by taking $z \to z(s)$ on the interface Γ_i:

$$\begin{aligned} \frac{1}{2} u_l^{\mathrm{P}}(s) + \int_{\Gamma_i} u_k^{\mathrm{P}}(s') t_{lk}^{\mathrm{P}*}(z(s), z(s'))\, ds' \\ - \int_{\Gamma_i} t_k^{\mathrm{P}}(s') u_{lk}^{\mathrm{P}*}(z(s), z(s'))\, ds' \\ = \int_{\Gamma_i} t_k^{\mathrm{T}}(s') u_{lk}^{\mathrm{P}*}(z(s), z(s'))\, ds', \end{aligned} \quad (2.26)$$

where $u_l^{\mathrm{P}}(s) = u_l^{\mathrm{P}}(z(s))$ and similarly for t_l^{P} and t_l^{T}. This procedure is repeated for each Ω_i^{P} with $i = 1, ..., p$. Note that with $z(s)$, $z(s') \in \Gamma_i$, the kernels $u_{lk}^{\mathrm{P}*}$ and $t_{lk}^{\mathrm{P}*}$ contain smooth functions as well as functions with logarithmic and Cauchy singularities. Moreover, part of the integral involving $t_{lk}^{\mathrm{P}*}$ is interpreted as a principal value integral because of the Cauchy singularity in $(n_l' r_{,k'} - n_k' r_{,l'})/r$.

Finally, since t_k^{T} is given, the integral equation (2.26) contains the two unknowns u_k^{P} and t_k^{P} on Γ_i. To determine them, we obtain an analogous expression to (2.26) in the matrix domain and use the continuity conditions (2.19), (2.20) across each Γ_i.

Matrix. Since the matrix phase is infinite in extent, we separate the far-field behavior of the elastic fields as follows. Write

$$\begin{aligned} \varepsilon_{kj}^{\mathrm{M}} &= \bar{\varepsilon}_{kj} + \varepsilon_{kj}^0, \\ \sigma_{kj}^{\mathrm{M}} &= \bar{\sigma}_{kj} + \sigma_{kj}^0, \\ u_j^{\mathrm{M}} &= \bar{u}_j + u_j^0, \end{aligned} \quad (2.27)$$

where the superscript "0" denotes the given constant applied fields. Because the applied strains ε_{kj}^0 are given, the corresponding applied stress σ_{kj}^0 and surface traction $t_k^0 = \sigma_{kj}^0 n_j$ can be calculated through the constitutive law (2.15). Also, the applied displacement u_k^0 can be calculated up to a translation and rigid body rotation through the kinematic equation (2.16). Without loss of generality, we require no translation or rotation at infinity and in this way we completely specify u_k^0, i.e.,

$$u_1^0(x_1, x_2) = \varepsilon_{11}^0 x_1 + \varepsilon_{12}^0 x_2 \quad (2.28)$$

$$u_2^0(x_1, x_2) = \varepsilon_{12}^0 x_1 + \varepsilon_{22}^0 x_2. \quad (2.29)$$

Physically, we interpret this decomposition as the solution to the problem of uniform applied fields in a *homogeneous* media, denoted by "0," plus the fields induced by *inhomogeneity,* denoted with the bar. The integral formulation is applied only to the barred quantities. The barred stresses, strains, and displacement vanish at infinity.

Proceeding as in the precipitate phase, one multiplies the field equation $\bar{\sigma}_{kj,j} = 0$ by the test function $u_k^{\mathrm{M}*}$ and integrates over $\tilde{\Omega}^{\mathrm{M}}$, the region between the precipitates Ω_i^{P} and Γ_∞. This yields

$$\int_{\tilde{\Omega}^{\mathrm{M}}} \bar{\sigma}_{kj,j} u_k^{\mathrm{M}*}\, da = 0, \quad (2.30)$$

As before, integrating by parts yields the boundary integral

$$\int_{\tilde{\Omega}^{\mathrm{M}}} \bar{u}_k \sigma_{kj,j}^{\mathrm{M}*}\, da + \int_{\Gamma+\Gamma_\infty} \bar{u}_k u_k^{\mathrm{M}*}\, ds = \int_{\Gamma+\Gamma_\infty} \bar{t}_k t_k^{\mathrm{M}*}\, ds, \quad (2.31)$$

where $\sigma_{kj}^{\mathrm{M}*} = C_{kjlm}^{\mathrm{M}} \varepsilon_{lm}^{\mathrm{M}*} = C_{kjlm}^{\mathrm{M}} u_{l,m}^{\mathrm{M}*}$. Further, $\bar{t}_k = \bar{\sigma}_{kj}^{\mathrm{M}} n_j$ and $t_k^{\mathrm{M}*} = \sigma_{kj}^{\mathrm{M}*} n_j$ are the appropriate surface tractions. The test functions $u_k^{\mathrm{M}*}$ and $t_k^{\mathrm{M}*}$ are again chosen as Kelvin's solution (Eq. (2.24)), except with the elastic constants of the matrix. Equation (2.31) is then written as

$$\begin{aligned} -\bar{u}_l(z) + \int_{\Gamma+\Gamma_\infty} \bar{u}_k(z(s')) t_{lk}^{\mathrm{M}*}(z, z(s'))\, ds' \\ = \int_{\Gamma+\Gamma_\infty} \bar{t}_k(z(s')) u_{lk}^{\mathrm{M}*}(z, z(s'))\, ds', \quad z \in \tilde{\Omega}^{\mathrm{M}}. \end{aligned} \quad (2.32)$$

The boundary integrals in Eq. (2.32) involve integration along both the precipitate–matrix interfaces Γ and the far-field boundary Γ_∞. It turns out that the integral over Γ_∞ can be removed using the fact that

$$\lim_{R_\infty \to \infty} \int_{\Gamma_\infty} (\bar{u}_k t_{lk}^{\mathrm{M}*} - \bar{t}_k u_{lk}^{\mathrm{M}*})\, ds' = 0. \tag{2.33}$$

See Brebbia [7], for example. Thus, in the limit $R_\infty \to \infty$ one obtains

$$\begin{aligned} -\bar{u}_l(z) + \int_\Gamma \bar{u}_k(z(s'))t_{lk}^{\mathrm{M}*}(z, z(s'))\, ds' \\ = \int_\Gamma \bar{t}_k(z(s'))u_{lk}^{\mathrm{M}*}(z, z(s'))\, ds', \quad z \in \tilde{\Omega}^{\mathrm{M}}. \end{aligned} \tag{2.34}$$

Now, taking $z \to z(s)$ on Γ, one obtains

$$\begin{aligned} -\frac{1}{2}\bar{u}_l(s) + \int_\Gamma \bar{u}_k(s')t_{lk}^{\mathrm{M}*}(z(s), z(s'))\, ds' \\ = \int_\Gamma \bar{t}_k(s')u_{lk}^{\mathrm{M}*}(z(s), z(s'))\, ds'. \end{aligned} \tag{2.35}$$

As in the precipitate case, $\bar{u}_l(s) = \bar{u}_l(z(s))$, and similarly for $\bar{t}$. Moreover, part of the integral involving $t_{lk}^{\mathrm{M}*}$ is a principal value integral. Finally, using Eqs. (2.27) and (2.35), one finds that the actual elastic fields satisfy

$$\begin{aligned} -\frac{1}{2}u_l^{\mathrm{M}}(s) + \int_\Gamma u_k^{\mathrm{M}}(s')t_{lk}^{\mathrm{M}*}(z(s), z(s'))\, ds' \\ - \int_\Gamma t_k^{\mathrm{M}}(s')u_{lk}^{\mathrm{M}*}(z(s), z(s'))\, ds' \\ = -\frac{1}{2}u_l^0(s) + \int_\Gamma u_k^0(s')t_{lk}^{\mathrm{M}*}(z(s), z(s'))\, ds' \\ - \int_\Gamma t_k^0(s')u_{lk}^{\mathrm{M}*}(z(s), z(s'))\, ds', \end{aligned} \tag{2.36}$$

where $t_k^{\mathrm{M}} = \sigma_{kj}^{\mathrm{M}} n_j$.

Because the far-field displacement u_k^0 and surface traction t_k^0 are given, this equation contains only two unknowns u_k^{M} and t_k^{M} on Γ. We now match Eq. (2.36) with the precipitate equation (2.26) using the continuity conditions.

Continuity Conditions. The continuity conditions require that the displacements and tractions vary continuously across each Γ_i. Therefore, on each Γ_i, we write $u_l = u_l^{\mathrm{P}} = u_l^{\mathrm{M}}$ and $t_l = t_l^{\mathrm{P}} = t_l^{\mathrm{M}}$. Then, the quantities u_l and t_l satisfy *both* the precipitate and matrix equations (2.26) and (2.36). Together, this system can be written as

$$\mathscr{A}[u, t](\alpha, t) = b(\alpha, t), \tag{2.37}$$

where $u = (u_1, u_2)$, $t = (t_1, t_2)$, and $\mathscr{A} = (\mathscr{A}_{1,1,1}, ..., \mathscr{A}_{1,1,p}, \mathscr{A}_{1,2,1}, ..., \mathscr{A}_{1,2,p}, \mathscr{A}_{2,1}, \mathscr{A}_{2,2})$ with the components $\mathscr{A}_{1,l,j}$ coming from the jth precipitate equation and $\mathscr{A}_{2,l}$ from the matrix equation, i.e.,

$$\begin{aligned} \mathscr{A}_{1,l,j}[u, t] = \tfrac{1}{2}u_l + T_{lkj}^{P}[u_k] - U_{lkj}^{\mathrm{P}}[t_k] \\ \text{for } l = 1, 2; j = 1, ..., p, \end{aligned} \tag{2.38}$$

$$\begin{aligned} \mathscr{A}_{2,l}[u, t] = -\tfrac{1}{2}u_l + T_{lk}^{\mathrm{M}}[u_k] - U_{lk}^{\mathrm{M}}[t_k] \\ \text{for } l = 1, 2. \end{aligned} \tag{2.39}$$

The operators T and U are given by

$$\begin{aligned} T_{lkj}^{\chi}[\mu](s, t) = \int_{\Gamma_j} \mu(s')t_{lk}^{\chi*}(z(s), z(s'))\, ds', \\ U_{lkj}^{\chi}[\sigma](s, t) = \int_{\Gamma_j} \sigma(s')u_{lk}^{\chi*}(z(s), z(s'))\, ds', \end{aligned} \tag{2.40}$$

where $u_{lk}^{\chi*}$ and $t_{lk}^{\chi*}$ are the fundamental solutions given in Eqs. (2.24) with $\chi = P, M$. Further, if $\chi = M$, then Γ_j is replaced by Γ and the additional subscript j is dropped.

Finally, the right-hand side vector $b = (b_{1,1,1}, ..., b_{1,l,p}, b_{1,2,1}, ..., b_{1,2,p}, b_{2,1}, b_{2,2})$ is given by

$$b_{1,l,j} = T_{lkj}^{\mathrm{P}}[t_k^{\mathrm{T}}] \tag{2.41}$$

$$b_{2,l} = -\tfrac{1}{2}u_l^0 + U_{lk}^{\mathrm{M}}[u_k^0] - T_{lk}^{\mathrm{M}}[t_k^0]. \tag{2.42}$$

We note that the system (2.37) is actually not of Fredholm type since t_{lk}^{*} contains a term with a Cauchy singularity. Nevertheless, it can be shown that (2.37) is uniquely solvable. This follows from the fact that the equations can be transformed to a second-kind Fredholm system using the small-scale decomposition given in Section 3.2. This obviates the need to directly formulate integral equations in second-kind form, using Goursat functions, for example [38]. Fredholm theory then shows that uniqueness guarantees existence [42]. Uniqueness is obtained since the displacement is uniquely specified at infinity.

Further, if Eq. (2.37) is discretized directly, the presence of the log terms in $u_{lk}^{\chi*}$ causes the condition number of the discrete system to increase at least linearly with N. The condition number also increases slowly as p increases. Thus, (2.37) is ill-conditioned with respect to both N and p, although the ill-conditioning with respect to p is weak. As in the diffusion case, we note that the condition number is sensitive to the minimum spacing between and the size of precipitates. In Section 3.2, Eq. (2.37) is reformulated using a small scale decomposition to remove the ill-conditioning with respect to N, the primary source of ill-conditioning.

It should be emphasized that this formulation is valid for both singly and multiply connected domains and can

be easily extended to the multiple phase case where the precipitates all have different elastic constants.

G^{el} Calculation. Once the displacements u_j and tractions t_j on Γ are found from Eq. (2.37), G^{el} must be calculated through Eq. (2.13). Thus, the limiting components of stress and strain on the interface (from both the precipitate and matrix sides) must be obtained from the displacements and tractions.

It is natural to calculate G^{el} in a local normal-tangent coordinate system on each interface. Let the unit normal and tangent vectors on each interface be n and s, respectively. The solutions $u = (u_1, u_2)$ and $t = (t_1, t_2)$ are converted from the global 1–2 coordinate system to the local $n - s$ system by

$$\begin{aligned} t_n &= t \cdot n, \\ t_s &= t \cdot s, \end{aligned} \tag{2.43}$$

and similarly for u. Notice that in the $n - s$ system (where the subscripts are not summed)

$$\begin{aligned} \sigma_{nn}^{P} &= \sigma_{nn}^{M} = t_n, \\ \sigma_{ns}^{P} &= \sigma_{ns}^{M} = t_s. \end{aligned} \tag{2.44}$$

Next, the calculation of ε_{ss}^{χ} on the interface is as follows: First, $\varepsilon_{ss}^{P} = \varepsilon_{ss}^{M}$ on Γ since coherency requires no slippage along Γ. Second, observe that

$$\varepsilon_{ss}^{\chi} = \varepsilon_{ij}^{\chi} s_i s_j = (\nabla u) s \cdot s = \frac{\partial u}{\partial s} \cdot s. \tag{2.45}$$

The considerations above yield the stress and strain components $\sigma_{nn}^{\chi}, \sigma_{ns}^{\chi}, \varepsilon_{ss}^{\chi}$ for each phase. The other three strain and stress components are recovered directly from the constitutive equations (2.14) and (2.15) in the precipitate and matrix, where the misfit strain must also be transformed to the local $n - s$ coordinate system. The remaining stresses and strains in the matrix phase are given by

$$\varepsilon_{nn}^{M} = \frac{1}{1 - \nu^{M}} \left[\frac{1 - 2\nu^{M}}{2\mu^{M}} t_n - \nu^{M} \varepsilon_{ss}^{M} \right] \tag{2.46}$$

$$\varepsilon_{ns}^{M} = \frac{1}{2\mu^{M}} t_s \tag{2.47}$$

$$\sigma_{ss}^{M} = \frac{1}{\nu^{M}} [(1 - \nu^{M}) t_n - 2\mu^{M} \varepsilon_{nn}^{M}] \tag{2.48}$$

and in the precipitate phase by

$$\varepsilon_{nn}^{P} = \frac{1}{1 - \nu^{P}} \left[\frac{1 - 2\nu^{P}}{2\mu^{P}} t_n - \nu^{P} (\varepsilon_{ss}^{P} - \varepsilon_{ss}^{T}) \right] + \varepsilon_{nn}^{T} \tag{2.49}$$

$$\varepsilon_{ns}^{P} = \frac{1}{2\mu^{P}} t_s + \varepsilon_{ns}^{T} \tag{2.50}$$

$$\sigma_{ss}^{P} = \frac{1}{\nu^{P}} [(1 - \nu^{P}) t_n - 2\mu^{P} (\varepsilon_{nn}^{P} - \varepsilon_{nn}^{T})]. \tag{2.51}$$

Once all the stress and strain components are found, G^{el} (on each interface) is obtained directly from Eq. (2.13) by summing on the indices $i, j = n, s$.

2.3. Surface and Elastic Energies

The total energy of our evolving multiphase system is the sum of the surface and elastic energies. It is well known that in the presence of an applied field, the elastic energy in an unbounded domain is infinite (as is the case here). However, by subtracting off the infinite energy associated with a homogeneous medium (with elastic constants of the matrix) under the same applied field, one obtains a finite part of the elastic energy that can be used to study the behavior of our system [41]. Let ZW_{el} be this finite part. Then the corresponding finite part of the total energy is given by

$$W_{tot} = W_{\Gamma} + ZW_{el}, \tag{2.52}$$

where the surface energy W_{Γ} is naturally given by the boundary integral

$$W_{\Gamma} = \int_{\Gamma} ds \tag{2.53}$$

so that W_{Γ} is simply the sum of the lengths of the precipitate–matrix interfaces. In this section, we derive a boundary integral representation for W_{el}. This is efficient computationally. In addition, in the absence of a far-field flux ($J = 0$, equilibration), we show that W_{tot} is nonincreasing in time.

Consider the elastic energy $\tilde{W}_{el}$ in a finite domain $\tilde{\Omega}$ that is the union of Ω^{P} and the part of Ω^{M} bounded by the circle Γ_{∞}, i.e., $\tilde{\Omega} = \Omega^{P} \cup \tilde{\Omega}^{M}$. $\tilde{W}_{el}$ is given by

$$\tilde{W}_{el} = \frac{1}{2} \int_{\tilde{\Omega}} \sigma_{ij} e_{ij} \, dA, \tag{2.54}$$

where e_{ij} is the elastic part of the strain and is given by

$$e_{kl} = \begin{cases} \varepsilon_{kl} - \varepsilon_{kl}^{T} & \text{in } \Omega^{P} \\ \varepsilon_{kl} & \text{in } \Omega^{M} \end{cases} \tag{2.55}$$

with the ε_{ij} given in Eq. (2.16). Then, W_{el} is given by the finite part of the limit $\lim_{R_{\infty} \to \infty} \tilde{W}_{el}$ which we give below.

We now write $\tilde{W}_{el}$ as a boundary integral. Following Christensen [8], one can obtain

$$\begin{aligned} \tilde{W}_{el} = W_0 &+ \frac{1}{2} \int_{\Gamma} (t_i u_i^0 - t_i^0 u_i) \, ds - \frac{1}{2} \int_{\Gamma} t_i^{T} (u_i - u_i^{T}) \, ds \\ &- \int_{\Gamma_{\infty}} t_i^0 \bar{u}_i \, ds - \frac{1}{2} \int_{\Gamma_{\infty}} \bar{t}_i \bar{u}_i \, ds, \end{aligned} \tag{2.56}$$

where the barred quantities are given by the decomposition in Eq. (2.27). W_0 is the energy associated with a homogeneous medium under the applied stress σ^0_{ij} and is given by

$$W_0 = \frac{1}{2}\int_{\tilde{\Omega}} \sigma^0_{ij} u^0_{i,j}\, dA. \tag{2.57}$$

In deriving Eq. (2.56), we have carefully taken into account the fact that neither Dirichlet nor Neumann boundary conditions are typically met on the finite outer boundary Γ_∞.

We now consider the limit as $R_\infty \to \infty$. Since σ^0_{ij} and $u^0_{i,j}$ are constant, we see that $W_0 = O(R_\infty^2)$ as $R_\infty \to \infty$ and is independent of the positions of the precipitate–matrix interfaces. Further, on Γ_∞ it can be shown that

$$\bar{u}_i = O(R_\infty^{-1}) \tag{2.58}$$

$$\bar{t}_j = O(R_\infty^{-2}) \tag{2.59}$$

$$ds = O(R_\infty) \tag{2.60}$$

as $R_\infty \to \infty$. Therefore $\tilde{W}_{\rm el} - W_0$ is finite in the limit as $R_\infty \to \infty$. However, as $R_\infty \to \infty$ the integral $\int_{\Gamma_\infty} t^0_i \bar{u}_i\, ds$ approaches a constant that depends on the interface positions and the elastic fields.

Based on the above results, we define $W_{\rm el}$ to be

$$\begin{aligned} W_{\rm el} &= \lim_{R_\infty\to\infty} (\tilde{W}_{\rm el} - W_0) \\ &= \frac{1}{2}\int_\Gamma (t_i u^0_i - t^0_i u_i)\, ds - \frac{1}{2}\int_\Gamma t^{\rm T}_i (u_i - u^{\rm T}_i)\, ds - I_\infty, \end{aligned} \tag{2.61}$$

where I_∞ is given by the limit

$$I_\infty = \lim_{R_\infty\to\infty} \int_{\Gamma_\infty} t^0_i \bar{u}_i\, ds. \tag{2.62}$$

It now remains to consider I_∞. In the special case where the applied traction at infinity is zero, then $t^0_i = 0$ (Neumann condition at infinity) and $I_\infty = 0$. Note that in this case, $W_0 = 0$ as well. I_∞ would also vanish if Dirichlet conditions were imposed on the barred displacements on *every* Γ_∞ as well. However, this is *not true* in general since $\bar{u}_l$ is given by

$$\begin{aligned} \bar{u}_l(z) = &\int_\Gamma (u_k(s') - u^0_k(s')) t^{\rm M*}_{lk}(z, z(s'))\, ds' \\ &- \int_\Gamma (t_k(s) - t^0_k(s')) u^{\rm M*}_{lk}(z, z(s'))\, ds', \end{aligned} \tag{2.63}$$

for $z \in \Omega^{\rm M}$ and where u_k and t_k satisfy the integral equations (2.37)–(2.42). See Eq. (2.34), for example. Thus I_∞ is zero only in the absence of applied fields.

Fortunately, given the $u_k(s)$ and $t_k(s)$ on Γ, it is straightforward to expand $\bar{u}_l$ in powers of $1/R_\infty$ for $z = R_\infty e^{i\alpha} \in \Gamma_\infty$. In Appendix B, we obtain an explicit expression for the $O(1/R_\infty)$ coefficient. This coefficient depends on trigonometric functions of α, the first moments of the t_k on Γ and modified first moments of u_k on Γ. An explicit expression for I_∞ is obtained by multiplying the coefficient by t^0_i (which is $O(1)$ in R_∞) and integrating over α, where $d\alpha = ds/R_\infty$. We refer the reader to Appendix B for the details, as well as for the final formula for I_∞. This formula is rather complicated and is given in Eq. (B.43).

We remark that, unlike the formula given on page 29 in [8], our result for $W_{\rm el}$ given in Eqs. (2.61) and (B.43) is appropriate for an infinite domain under general loading conditions. To our knowledge, this formula for the finite part of the elastic energy in an unbounded domain has not been obtained previously.

Finally, it is useful to also calculate the time rate of change of the finite part of the total energy,

$$\frac{dW_{\rm tot}}{dt} = \frac{dW_\Gamma}{dt} + Z\frac{dW_{\rm el}}{dt}. \tag{2.64}$$

It is well known that for W_Γ given by Eq. (2.53),

$$\frac{dW_\Gamma}{dt} = \int_\Gamma \kappa V\, ds, \tag{2.65}$$

where V is the normal velocity of Γ. A straightforward calculation yields the result

$$\frac{dW_{\rm el}}{dt} = \int_\Gamma G^{\rm el} V\, ds, \tag{2.66}$$

where $G^{\rm el}$ is the elastic energy density given by Eq. (2.13). Hence,

$$\frac{dW_{\rm tot}}{dt} = \int_\Gamma (\kappa + ZG^{\rm el}) V\, ds. \tag{2.67}$$

Note that on Γ, $U = \kappa + ZG^{\rm el}$ and $\nabla U \cdot n = V$. Therefore,

$$\frac{dW_{\rm tot}}{dt} = \int_\Gamma U(\nabla U \cdot n)\, ds. \tag{2.68}$$

If $J = 0$, then using the fact that U is harmonic in $\Omega^{\rm M}$, U is bounded at infinity, and ∇U decays rapidly ($1/R_\infty^2$) at infinity, the divergence theorem yields

$$\frac{dW_{\rm tot}}{dt} = -\int_{\Omega^{\rm M}} \nabla\cdot(U\nabla U)\, dA = -\int_{\Omega^{\rm M}} |\nabla U|^2\, dA \le 0. \tag{2.69}$$

This shows that, in the absence of a far-field flux, the finite part of the total energy W_{tot} is nonincreasing in time.

2.4. Scaled Arclength Frame and Tangent Angle Formulation

In this section, we describe the scaled arclength reference frame used to evolve Γ. The scaled arclength frame specifies that along a parameterized curve $(x_1(\alpha, t), x_2(\alpha, t))$, the local variation of the arclength $s_{,\alpha} = \sqrt{x_{1,\alpha}^2 + x_{2,\alpha}^2}$ is proportional to the length of the interface. Further, the equations of motion are reposed in terms of the tangent angle and the length of the interface. These choices allow us to use the nonstiff time-updating scheme developed by Hou, Lowengrub, and Shelley [17].

Consider the motion of a single interface Γ_i, with $x_i = (x_{1i}(\alpha, t), x_{2i}(\alpha, t)) \in \Gamma_i$. The subscript i refers to the interface and is not summed in the equations below. Suppose the normal velocity is given by V_i, obtained from Eq. (2.12), for example. Write the tangential velocity as T_i and observe that the shape of Γ_i is independent of T_i. The velocity T_i merely specifies the frame of the parametrization of Γ_i and here is chosen as

$$T_i(\alpha, t) = T_i(0, t) + \int_0^\alpha s_{i,\alpha'} \kappa_i V_i \, d\alpha' - \frac{\alpha}{2\pi} \int_0^{2\pi} s_{i,\alpha'} \kappa_i V_i \, d\alpha', \tag{2.70}$$

where κ_i denotes the curvature of Γ_i. The motion of the curve is given by

$$\frac{d}{dt} x_i(\alpha, t) = V_i(\alpha, t) n_i + T_i(\alpha, t) s_i, \tag{2.71}$$

where n_i and s_i are the normal and tangent vectors to Γ_i. This is called the scaled arclength frame because $s_{i,\alpha}(\alpha, t) = L_i(t)/2\pi$, where $L_i(t)$ is the total length of Γ_i. The primary advantage of this frame is that it prevents local clustering of the parametrization in time. For further details, see [17].

The prominent role of the curvature in Eq. (2.2) for the boundary condition of the diffusion field suggests that in the scaled arclength frame, each interface Γ_i may be more naturally described using the tangent angle $\theta_i = \tan^{-1}(x_{2i,\alpha}/x_{1i,\alpha})$, and length L_i, as the dynamical variables rather than $x_i = (x_{1i}, x_{2i})$ since $\kappa_i = 2\pi\theta_{i,\alpha}/L_i$. The curve position x_i is recovered by integrating

$$x_{i,\alpha} = \frac{L_i}{2\pi} (\cos(\theta_i(\alpha, t)), \sin(\theta_i(\alpha, t))), \tag{2.72}$$

where the constants of integration are chosen by evolving another piece of information about the curve, such as its endpoint or the center of mass of the region it encloses. We have implemented both procedures. In summary, the $\theta - L$ formulation of the equations of motion for each interface Γ_i are given by

$$L_{i,t} = -\int_0^{2\pi} \theta_{i,\alpha'} V_i(\alpha', t) \, d\alpha' \tag{2.73}$$

$$\theta_{i,t} = \frac{2\pi}{L_i} (V_{i,\alpha} + T_i \theta_{i,\alpha}). \tag{2.74}$$

In Section 4.1, we follow [17] and use this $\theta - L$ formulation to obtain a nonstiff time-updating scheme to evolve each Γ_i in time.

3. SMALL-SCALE DECOMPOSITIONS

Computing solutions to the diffusion and elasticity integral equations is a delicate matter due to the ill-conditioning of their discretized counterparts. In this section, we present reformulations of the diffusion and elasticity integral equations that result in well-conditioned discretized systems. The reformulation consists of separating and inverting the dominant terms at small spatial scales to yield equivalent but "preconditioned" systems. This is referred to as the "small-scale decomposition" (SSD). The SSD, however, does not ameliorate ill-conditioning associated with precipitate merging or vanishing, as these difficulties are inherent in the boundary integral formulation. The SSD presented here is similar in spirit to that presented in [17] to remove high order time step constraints.

The idea of the SSD is the following. Consider the system

$$K\mu = f \quad \text{with } K = \mathscr{L} + R, \tag{3.1}$$

where $\mathscr{L}$ dominates the small scales of K. If $\mathscr{L}$ is invertible, then Eq. (3.1) can be reformulated as

$$(I + \mathscr{L}^{-1} R)\mu = \mathscr{L}^{-1} f. \tag{3.2}$$

Moreover, if $\mathscr{L}$ is easy to invert, then the reformulation (3.2) involves little additional computational cost. Note that if $\mathscr{L}^{-1}R$ involves smooth integral kernels, then Eq. (3.2) is a second-kind Fredholm integral equation, even if the original system (3.1) is not Fredholm. Further, because the conditioning of a system is determined by its behavior at small scales, the reformulation is well-conditioned because the dominant behavior at small scales ($\mathscr{L}$) is inverted exactly. The resulting second-kind structure guarantees that the eigenvalues/singular values accumulate at $\lambda = 1$ [42]. In our reformulated equations, if the precipitates are well-separated and not too small, the eigenvalues cluster around 1, since the appropriate R's are infinite order smoothing operators (defined below). Such clustering is

important for the rapid convergence of certain iterative methods such as GMRES [44].

In the diffusion system, $\mathscr{L}$ is inverted in physical space as the small scale terms are local. This SSD was originally performed by Greenbaum, Greengard, and McFadden [11]. In the elasticity system, on the other hand, $\mathscr{L}$ is inverted in Fourier space. In that case the small scale terms are *nonlocal,* but are diagonalized by the Fourier transform. Computing $\mathscr{L}^{-1}$ involves inverting a 4×4 matrix (in Fourier space) for each interface.

We note that a related nonlocal preconditioning strategy was employed by Jeon for the biharmonic problem [18]. However, in that work, only a few of the dominant terms at small scales were separated, leading to a second-kind Fredholm system whose kernels possessed only a finite degree of smoothness. In general, the smoother the kernels in a second-kind Fredholm system, the more rapid is the convergence rate using (GMRES) iteration.

The small-scale decomposition of the integral equations is based on the following analysis of the three types of integral operators that appear in the equations: The operators involve integration against smooth kernels, logarithmic kernels, and Cauchy kernels and are given by

$$E[\mu](\alpha, t) = \frac{1}{\pi}\int_0^{2\pi} \mu(\alpha', t) e(\alpha, \alpha', t)\, d\alpha' \tag{3.3}$$

$$\mathscr{T}[\mu](\alpha, t) = \frac{1}{\pi}\int_0^{2\pi} \mu(\alpha', t) \log|z(\alpha', t) - z(\alpha, t)|\, d\alpha' \tag{3.4}$$

$$\mathscr{G}[\mu](\alpha, t) = \frac{1}{\pi}\int_0^{2\pi} \mu(\alpha') \frac{z_{,\alpha'}(\alpha', t)}{z(\alpha, t) - z(\alpha', t)}\, d\alpha', \tag{3.5}$$

where $e(\alpha, \alpha', t)$ is a smooth function of the parameters α and α' and time t. Further, in $\mathscr{G}$, the integral is interpreted as a principal value integral due to the Cauchy singularity of the kernel $z_{,\alpha'}/(z(\alpha, t) - z(\alpha', t))$.

We begin with the operator E. It involves integration against a smooth kernel. In [17], it was shown that E is an infinite order smoothing operator.

LEMMA 1 (Infinite Order Smoothing Operators). *Suppose that $e(\alpha, \alpha', t)$ is a real analytic function of both α and α' for $0 \le t \le T$ and the strip of analyticity is given by $|\mathrm{Im}\,\alpha|, |\mathrm{Im}\,\alpha'| \le \rho$. Then, for any μ, the Fourier transform of E, $\hat{E}[\mu](k)$, satisfies*

$$\hat{E}[\mu](k) = O\left(e^{-\rho|k|}\sum_l \hat{\mu}(l) e^{-\rho|l|}\right); \tag{3.6}$$

i.e.,

$$|\hat{E}[\mu](k)| \le C e^{-\rho|k|}\sum_l |\hat{\mu}(l)| e^{-\rho|l|} \tag{3.7}$$

for large $|k|$. This defines an infinite order smoothing operator.

We now motivate the form of the small scale decompositions for both $\mathscr{T}$ and $\mathscr{G}$. Our original intuition was that if the interface $\Gamma = z(\alpha, t)$ is smooth then the small scale behavior of these integrals could be obtained simply by retaining the first term in an expansion of the kernels about a circular interface. This intuition is justified in the following way. Let $\Gamma = z(\alpha, t)$ be *any* smooth, nonintersecting interface with $s_{,\alpha} = |z_{,\alpha}| > 0$. Then, we can write

$$\log|z(\alpha', t) - z(\alpha, t)| = \log 2\left|\sin\left(\frac{\alpha' - \alpha}{2}\right)\right| + \left[\log\frac{|z(\alpha', t) - z(\alpha, t)|}{2\left|\sin\left(\frac{\alpha' - \alpha}{2}\right)\right|}\right] \tag{3.8}$$

$$\frac{z_{,\alpha'}(\alpha', t)}{z(\alpha, t) - z(\alpha', t)} = \frac{1}{2}\cot\left(\frac{\alpha - \alpha'}{2}\right) + \left[\frac{z_{,\alpha'}(\alpha', t)}{z(\alpha, t) - z(\alpha', t)} - \frac{1}{2}\cot\left(\frac{\alpha - \alpha'}{2}\right)\right]. \tag{3.9}$$

The first terms in Eqs. (3.8) and (3.9) are those resulting from the circular interface $z = e^{i\alpha}$. Observe that the terms in brackets are smooth functions of α and α' (i.e., have removable singularities at $\alpha = \alpha'$). Therefore, $\mathscr{T}$ and $\mathscr{G}$ may be rewritten as

$$\mathscr{T}[\mu](\alpha, t) = \frac{1}{\pi}\int_0^{2\pi} \mu(\alpha', t) \log 2\left|\sin\left(\frac{\alpha' - \alpha}{2}\right)\right| d\alpha' + \frac{1}{\pi}\int_0^{2\pi} \mu(\alpha', t) e_1(\alpha, \alpha', t)\, d\alpha' \tag{3.10}$$

$$\mathscr{G}[\mu](\alpha, t) = \frac{1}{2\pi}\int_0^{2\pi} \mu(\alpha', t)\cot\left(\frac{\alpha - \alpha'}{2}\right) d\alpha' + \frac{1}{\pi}\int_0^{2\pi} \mu(\alpha', t) e_2(\alpha, \alpha', t)\, d\alpha', \tag{3.11}$$

where e_1 and e_2 are the bracketed terms in Eqs. (3.8) and (3.9), respectively. We recognize the first term in $\mathscr{G}$ to be the periodic Hilbert transform which we denote by $\mathscr{H}[\mu](\alpha, t)$. Moreover, introducing ξ by $\xi_{,\alpha} = \mu - \overline{\mu}$, with $\overline{\mu} = \hat{\mu}(0)/2\pi$, then integration by parts shows that the first term of $\mathscr{T}$ is given by $\mathscr{H}[\xi](\alpha, t)$ since $\int_0^{2\pi} \log 2|\sin((\alpha' - \alpha)/2)|\, d\alpha' = 0$. Combining these results and using Lemma 1, we obtain

LEMMA 2 (Small Scale Behavior of $\mathscr{T}$ and $\mathscr{G}$). *Suppose that the coordinates of the interface Γ, $(x_1(\alpha, t), x_2(\alpha, t))$,*

are real analytic functions of α *for* $0 \le t \le T$. *Suppose that the strip of analyticity about the real axis is given by* $|\mathrm{Im}\ \alpha| \le \rho$ *with* $\rho > 0$. *Suppose further that* Γ *does not self-intersect and* $s_{,\alpha} > 0$. *Then*

$$\mathscr{T}[\mu](\alpha, t) = \mathscr{H}[\xi](\alpha, t) + E_1[\mu](\alpha, t), \tag{3.12}$$

where $\xi_{,\alpha} = \mu - \overline{\mu}$;

$$\mathscr{G}[\mu](\alpha, t) = \mathscr{H}[\mu](\alpha, t) + E_2[\mu](\alpha, t), \tag{3.13}$$

where E_1 *and* E_2 *are infinite order smoothing operators and satisfy estimates analogous to* (3.6) *and* (3.7). *The smooth kernels of* E_1 *and* E_2 *are given by* e_1 *and* e_2.

The results (3.6), (3.7) and (3.13) were first given in [17] in a slightly different form. We refer the reader there for further details. It is important to note that lemmas 1 and 2 hold *for any* μ for which the Fourier transform is defined. As in [17], we define the notation $f \sim g$ to mean that their difference is a smoothing operator, i.e. $f \sim g \Leftrightarrow f - g = E[f, g]$ and hence g is the dominant term of f at small spatial scales. Thus, lemma 2 shows that $\mathscr{T}[\mu] \sim \mathscr{H}[\xi]$ and $\mathscr{G}[\mu] \sim \mathscr{H}[\mu]$. Using that the Fourier transform of $\mathscr{H}$ is given by $\hat{\mathscr{H}} = -i\mathrm{sgn}(k)$, the real advantage of this analysis is it shows that the leading terms of $\hat{\mathscr{T}}$ and $\hat{\mathscr{G}}$ are diagonal in Fourier space at small scales and thus $\mathscr{T}$ and $\mathscr{G}$ simplify enormously at these scales.

We now consider the diffusion and elasticity systems in detail.

3.1. Small Scale Analysis of the Diffusion System

In this section, we give the small-scale decomposition of the dipole formulation of the quasi-steady exterior diffusion problem (2.6) given in Section 2.1.1. We first analyze the integral operator part. Recall that

$$\mathscr{A}_1[\phi, A_1, ..., A_p] = \left(-\frac{1}{2}I + K\right)[\phi] + \sum_{k=1}^{p} A_k \log|z(s,t) - S_k|, \tag{3.14}$$

where K is the integral operator,

$$K[\phi](s,t) = \frac{1}{2\pi}\int_\Gamma \phi(s',t)\left[\frac{\partial}{\partial n(s',t)}\log|z(s',t) - z(s,t)| + 1\right] ds', \tag{3.15}$$

with $\Gamma = \cup_i \Gamma_i$ and $s = s(\alpha, t)$ is the arclength. Now, if Γ is a smooth, nonintersecting curve (or the union of smooth nonintersecting curves) with $s_{,\alpha} > 0$, then the integral kernel in Eq. (3.15),

$$\frac{\partial}{\partial n(s')}\log|z(s') - z(s)| + 1 = \mathrm{Im}\left\{\frac{z_{,s'}}{z(s) - z(s')} + i\right\}, \tag{3.16}$$

is a smooth function of α and α', even if $z(s) = z(s(\alpha))$ and $z(s') = z(s(\alpha'))$ lie on the same Γ_i. Thus, from Lemma 1, we see that the integral operator K is of type E, an infinite-order smoothing operator. Therefore,

$$(-\tfrac{1}{2}I + K) \sim -\tfrac{1}{2}I. \tag{3.17}$$

Thus, $\mathscr{A}_1[\phi, A_1, ..., A_p] \sim -\phi/2 + \sum_{k=1}^{p} A_k \log|z(s,t) - S_k|$. This suggests the decomposition of $\mathscr{A}$ in Eq. (2.6),

$$\mathscr{A} = \mathscr{L} + R, \tag{3.18}$$

where $R = \mathscr{A} - \mathscr{L}$, and $\mathscr{L} = (\mathscr{L}_1, \mathscr{L}_2, \mathscr{L}_{3,1}, ..., \mathscr{L}_{3,p-1})$, where the $\mathscr{L}_k$ are given by

$$\mathscr{L}_1[\phi, A_1, ..., A_p] = -\frac{1}{2}\phi + \sum_{k=1}^{p} A_k \log|z(\alpha,t) - S_k|, \qquad \mathscr{L}_2 = \mathscr{A}_2, \quad \mathscr{L}_{3,j} = \mathscr{A}_{3,j}. \tag{3.19}$$

Thus, $\mathscr{L}$ dominates the small scales of $\mathscr{A}$ and $R = (K, 0, 0, .., 0)$ is an infinite-order smoothing operator. Moreover, solving the system $\mathscr{L}[\phi, A_1, ..., A_p] = b = (b_1, b_2, b_3, ..., b_{p+1})$ involves inverting the $p \times p$ system for the A_k given by

$$\sum_{k=1}^{p} A_k \int_{\Gamma_j} \log|z(s',t) - S_k|\, ds' = \sum_{k=1}^{p} \int_{\Gamma_j} b_1(s',t)\, ds' + \frac{1}{2} b_{j+2} \quad \text{for } j = 1, ..., p-1, \tag{3.20}$$

$$\sum_{k=1}^{p} A_k = b_2, \tag{3.21}$$

and then constructing ϕ by

$$\phi(s,t) = 2\sum_{k=1}^{p} A_k \log|z(s,t) - S_k| - 2b_1(s,t). \tag{3.22}$$

This is much simpler than solving the original system (2.6). The system (3.20)–(3.21) can be solved using Gaussian elimination, for example. Now, inverting $\mathscr{L}$ as above yields the equivalent system to (2.6) given by

$$(I + \mathscr{L}^{-1}R)[\phi, A_1, ..., A_p] = \mathscr{L}^{-1}b. \tag{3.23}$$

This is the SSD and was first introduced to this quasi-steady diffusion problem by Greenbaum, Greengard, McFadden [11]. Notice that the SSD is a fully second-kind Fredholm system and $\mathscr{L}^{-1}R$ is an infinitely smoothing operator, since R itself is infinitely smoothing. Therefore, its discretization will be well-conditioned.

Finally, we comment on the effects of precipitate merging or vanishing on the above analysis. If precipitates merge or vanish, then a topological singularity occurs. The kernel of K is no longer smooth and thus the application of K is not smoothing. Consequently, the hypothesis of Lemma 1 breaks down (the strip of analyticity vanishes) and K becomes important at small spatial scales. Moreover, neither the SSD nor the original system (2.6) are then Fredholm because of the kernel singularity. In computations, this difficulty is reflected by a rapid increase in condition number and, hence, iteration count when the particles become very close or very small. In practice, we also find that to keep the iteration count(s) low, the interface(s) must be well-resolved.

We now turn to the elasticity integral equations.

3.2. Small-Scale Analysis of Elasticity Integral Equations

In this section, we present the SSD for the integral equations arising from the multiphase elasticity boundary integral equations given in (2.37)–(2.39). Recall that they are given in terms of the operators T and U with

$$\begin{aligned} T^{\chi}_{lkj}[\mu](s,t) &= \int_{\Gamma_j} \mu(s') t^{\chi*}_{lk}(z(s), z(s'))\, ds', \\ U^{\chi}_{lkj}[\sigma](s,t) &= \int_{\Gamma_j} \sigma(s') u^{\chi*}_{lk}(z(s), z(s'))\, ds', \end{aligned} \tag{3.24}$$

where $\chi = P, M$. If $\chi = M$, Γ_j is replaced by Γ and the subscript j is dropped. Recall that the integral kernels are given by

$$u^{\chi*}_{lk}(z,z') = \frac{1}{8\pi\mu^{\chi}(1-\nu^{\chi})}\left[(3-4\nu^{\chi})\ln\left(\frac{1}{r}\right)\delta_{lk} + r_{,l'}r_{,k'}\right] \tag{3.25}$$

$$\begin{aligned} t^{\chi*}_{lk}(z,z') = \frac{-1}{4\pi r(1-\nu^{\chi})}\Bigg[&\frac{\partial r}{\partial n'}\left((1-2\nu^{\chi})\delta_{lk} + 2r_{,l'}r_{,k'}\right) \\ &+ (1-2\nu^{\chi})(n'_l r_{,k'} - n'_k r_{,l'})\Bigg], \end{aligned} \tag{3.26}$$

with $r = |z' - z|$ with $r_{,k'} = \partial r/\partial x'_k$. These kernels involve smooth functions, logarithms, and functions with Cauchy singularities.

We begin the analysis by considering T and U. Our first observation is that if $z \in \Gamma_i$ and $z' \in \Gamma_j$ with $j \neq i$, then both $u^{\chi*}_{lk}$ and $t^{\chi*}_{lk}$ are smooth functions of $s = s(\alpha, t)$. Using Lemma 1 this implies that the self-induction integrals dominate the small spatial scales; i.e.,

$$\begin{aligned} T^{\chi}_{lkj}[\mu](s,t) &\sim \int_{\Gamma_j} u(s') t^{\chi*}_{lk}(z(s), z(s'))\, ds', \\ U^{\chi}_{lkj}[\sigma](s,t) &\sim \int_{\Gamma_j} \sigma(s') u^{\chi*}_{lk}(z(s), z(s'))\, ds', \end{aligned} \tag{3.27}$$

where $z(s) \in \Gamma_j$. If $\chi = M$, then the subscript j is dropped on the LHS of the above but the integration is still over Γ_j.

Now, we investigate the integrals in Eq. (3.27). We begin with U as it is simpler. It is straightforward to see that $r_{,l'} \cdot r_{,k'}$ is in fact a smooth function even if $z, z' \in \Gamma_j$. Thus, parametrizing Γ_j by α, i.e., $s = s(\alpha, t)$, and applying Lemma 1, one obtains

$$U^{\chi*}_{lkj}[\sigma](\alpha,t) \sim C^{\chi}\pi\delta_{lk}\mathscr{F}[\tilde{\sigma}](\alpha,t), \tag{3.28}$$

where $\tilde{\sigma} = \sigma s_{,\alpha}$ and $C^{\chi} = (4\nu^{\chi} - 3)/8\pi\mu^{\chi}(1-\nu^{\chi})$. Therefore, by Lemma 2, we find that

$$U^{\chi}_{lkj}[\sigma](\alpha,t) \sim C^{\chi}\pi\delta_{lk}\mathscr{H}[\tilde{\xi}](\alpha,t), \tag{3.29}$$

where $\tilde{\xi}_{,\alpha} = \tilde{\sigma} - \overline{\tilde{\sigma}}$. This is the small scale decomposition of U. In practice, since we use the scaled arclength frame, $\tilde{\sigma}$ only differs from σ by the spatial constant $L_j/2\pi$.

We turn now to T. A straightforward calculation shows that $(1/r)\partial r/\partial n(s') = \partial/\partial n(s') \log|z(s') - z(s)|$ is a smooth function. Since $r_{,k'} \cdot r_{,l'}$ is also smooth, we find that by Lemma 1

$$T^{\chi}_{lkj}[\mu](\alpha,t) \sim D^{\chi}\int_0^{2\pi} \frac{\mu(\alpha')}{|z'-z|}(n'_l r_{,k'} - n'_k r_{,l'}) s_{,\alpha'}\, d\alpha', \tag{3.30}$$

where $D^{\chi} = (2\nu^{\chi} - 1)/4\pi(1-\nu^{\chi})$. A calculation shows that

$$\frac{n'_l r_{,k'} - n'_k r_{,l'}}{|z'-z|} = \frac{\varepsilon_{lk3}}{s_{,\alpha'}}\,\mathrm{Re}\left\{\frac{z_{,\alpha'}}{z'-z}\right\}, \tag{3.31}$$

where the permutation symbol ε_{lk3} is given by

$$\varepsilon_{lk3} = \begin{cases} 1 & \text{if } l = 1, k = 2, \\ -1 & \text{if } l = 2, k = 1, \\ 0 & \text{if } l = k. \end{cases}$$

Therefore,

$$T^{\chi}_{lkj}[\mu](\alpha,t) \sim -D^{\chi}\pi\varepsilon_{lk3}\mathrm{Re}\{\mathscr{G}[\mu](\alpha,t)\} \tag{3.32}$$

$$\sim -D^{\chi}\pi\varepsilon_{lk3}\mathscr{H}[\mu](\alpha,t) \tag{3.33}$$

by Lemma 2. This is the small scale decomposition of T^{χ}_{lkj}.

We are now ready to put everything together. Use the small scale decompositions of T and U to decompose the $\mathscr{A}$ in Eq. (2.37) as

$$\mathscr{A} = \mathscr{L} + R, \tag{3.34}$$

where $R = \mathscr{A} - \mathscr{L}$, and $\mathscr{L} = (\mathscr{L}_{1,1,1}, ..., \mathscr{L}_{1,1,p}, \mathscr{L}_{1,2,1}, ..., \mathscr{L}_{1,2,p}, \mathscr{L}_{2,1}, \mathscr{L}_{2,2})$ with the components $\mathscr{L}$ given by

$$\mathscr{L}_{1,l,j}[u,t] = \tfrac{1}{2}u_l - D^P \pi \varepsilon_{lk3} \mathscr{H}[u_k] - C^P \pi \delta_{lk} \mathscr{H}[\tilde{T}_k], \quad (3.35)$$

$$\mathscr{L}_{2,l}[u,t] = \tfrac{1}{2}u_l - D^M \pi \varepsilon_{lk3} \mathscr{H}[u_k] - C^M \pi \delta_{lk} \mathscr{H}[\tilde{T}_k], \quad (3.36)$$

where $\tilde{T}_{k,\alpha} = L_j t_k / 2\pi$ since $\bar{t}_k = 0$. Note that in Eqs. (3.35) and (3.36) we abuse notation slightly. The u and t that appear on the right-hand sides of Eqs. (3.35) and (3.36) are those displacements and tractions on Γ_j, whereas the brackets on the left-hand side contain the displacements and tractions on *all* the interfaces. Consequently, observe that on each Γ_j, $\mathscr{L}$ only involves those u and t on Γ_j. Note that this is not true of the original operator $\mathscr{A}$ because T^{M} and U^{M} involve integration over Γ and, hence, they involve all the u and t. In addition, although $\mathscr{L}$ is nonlocal, observe that in the scaled arclength frame, it is diagonalized by the Fourier transform. Using the above two observations, it is not difficult to see that solving $\mathscr{L}[u, t] = b$ on each interface only involves inverting a 4×4 matrix in Fourier space. The actual 4×4 matrix is given in Appendix C. This is much simpler than solving the original system (2.37). We first described this procedure in [26] but did not give details.

Inverting $\mathscr{L}$ in Fourier space we obtain the equivalent system to (2.37) given by

$$(I + \mathscr{L}^{-1}R)[u,t] = \mathscr{L}^{-1}b. \quad (3.37)$$

Notice that Eq. (3.37) is a second-kind Fredholm system and $\mathscr{L}^{-1}R$ is an infinite order smoothing operator since R itself is smoothing. And, unlike the original non-Fredholm system (2.37), the discretization of (3.37) will be well-conditioned. What remains of the original ill-conditioning is that $\widehat{\mathscr{L}^{-1}} \sim |k|$ for large k (see Appendix C). Thus, numerical errors in b and R are amplified by the application of $\mathscr{L}^{-1}$. To control these, we use the numerical filter described in Section 4.3.

As in the diffusion case, if precipitates merge or vanish, then the hypotheses of Lemmas 1 and 2 break down as a topological singularity occurs. In this case, the smoothing operator R becomes important at small spatial scales. In numerical computations, this difficulty is reflected by a rapid increase in iteration count(s) when particles become very close or very small. As in the diffusion case, to keep iteration count(s) low, the interface(s) must be well-resolved.

4. IMPLEMENTATION

In this section, we present our numerical scheme. Our method uses a second-order, nonstiff linear propagator time-stepping routine, developed by Hou, Lowengrub, and Shelley [17], to advance the positions of the interfaces in time. Spectrally accurate spatial discretizations are used to compute all derivatives and integrals. In addition, the iterative method GMRES [44] is used to solve the diffusion and elasticity systems using the small scale preconditioning developed in the previous section. A high order Fourier filter is also employed.

4.1. Temporal Discretization

We begin by discussing the time discretization of the equations of motion given in (2.73) and (2.74). The ODE for the length $L_i(t)$ of Γ_i is not difficult to solve numerically. Any explicit discretization method can be used. In the calculations presented here, the second-order Adams–Bashforth method is used,

$$L_i^{n+1} = L_i^n + \frac{\Delta t}{2}(3M_i^n - M_i^{n-1}), \quad (4.1)$$

where the superscript denotes the time level and M_i is given by

$$M_i = -\int_0^{2\pi} \theta_{i,\alpha'} V_i(\alpha', t)\, d\alpha'. \quad (4.2)$$

We also use the second-order Adams–Bashforth method to compute the motion of the endpoint or the center of mass.

It turns out, however, that straightforward time discretizations of Eq. (2.74) for the tangent angle θ_i suffer from severe time step restrictions (stiffness) imposed by the large number of spatial derivatives in the equations of motion. These arise from the derivatives present in the curvature term in the boundary condition (2.2) and the normal velocity V_i [17]. Note, in particular, that the curvature dominates the elasticity at the smallest scales (see the end of Appendix D). Using the small-scale analysis and following Hou, Lowengrub, and Shelley [17], it can be shown that if Eq. (2.74) is updated using an explicit time stepping method, the time step Δt must satisfy a stability restriction of the type $\Delta t \le C(L_i h_i / 2\pi)^3$, where h_i is the spatial grid size on Γ_i. We refer the reader to [17] for further details.

To remove the stiffness, we follow [17] and rewrite Eq. (2.74) with the dominant small-scale behavior explicitly separated as follows:

$$\theta_{i,t} = \left(\frac{2\pi}{L_i}\right)^3 \mathscr{H}[\theta_{i,\alpha\alpha\alpha}] + N_i(\alpha, t), \quad (4.3)$$

where

$$N_i(\alpha, t) = \frac{2\pi}{L_i}(V_{i,\alpha} + T_i\theta_{i,\alpha}) - \left(\frac{2\pi}{L_i}\right)^3 \mathscr{H}[\theta_{i,\alpha\alpha\alpha}]. \quad (4.4)$$

The remainder terms N_i are "lower order" at small spatial scales. Note that the dominant term is diagonalized by the Fourier transform. Implicit time discretizations, such as Crank–Nicholson differencing or linear propagator methods, can now be easily applied. In this paper, we use the following second-order linear propagator method derived in [17],

$$\hat{\theta}_i^{n+1}(k) = e_{ik}(t_n, t_{n+1})\hat{\theta}_i^n(k) + \frac{\Delta t}{2}(3e_{ik}(t_n, t_{n+1})\hat{N}_i^n(k) - e_{ik}(t_{n-1}, t_{n+1})\hat{N}_i^{n-1}(k)), \quad (4.5)$$

where $e_{ik}(t_n,\ t_{n+1})$ and $e_{ik}(t_{n-1},\ t_{n+1})$ are the exponential damping factors,

$$e_{ik}(t_n, t_{n+1}) = \exp\left(-\frac{\Delta t}{2}(2\pi|k|)^3\left[\frac{1}{(L_i^n)^3} + \frac{1}{(L_i^{n+1})^3}\right]\right) \quad (4.6)$$

$$e_{ik}(t_{n-1}, t_{n+1}) = \exp\left(-\Delta t(2\pi|k|)^3\left[\frac{1}{2(L_i^{n-1})^3} + \frac{1}{(L_i^n)^3} + \frac{1}{2(L_i^{n+1})^3}\right]\right). \quad (4.7)$$

This scheme at most suffers from a first-order time constraint (i.e., $\Delta t \le Ch$), arising from the transport term hidden in N. This scheme is straightforward to implement and to our knowledge is the most successful and efficient interface tracking method in the presence of surface tension [17, 16]. The time steps used in this paper are chosen in order to satisfy the first-order time constraint and also to resolve any fast time scales present in the evolution. We note that these are separate issues.

4.2. Spatial Discretization

In this section, we discuss the spatial discretizations used in our numerical scheme. It turns out that one must be quite careful when discretizing in space. For example, it has been observed by Baker and Nachbin [5] and Beale, Hou, and Lowengrub [6] that lower order spatial discretizations of certain related boundary integral equations can lead to violently unstable schemes. This instability is unrelated to the strict time step constraints normally introduced by the curvature (surface energy) and is due, instead, to the fact that lower order schemes tend to suppress the stabilizing effect of the surface energy at the smallest scales. In fact, even spectrally accurate schemes may be unstable as a result of aliasing errors [6].

Here, we use spectrally accurate spatial discretizations along with a numerical filter to remove aliasing errors. The filter will be described in the next section. Any differentiation, partial integration or Hilbert transform is found at the mesh points by using the discrete Fourier transform (DFT). It now remains to discuss the quadrature of the integrals appearing in the diffusion and elasticity integral equations.

The three types of integrals that appear in the diffusion and elasticity integral equations—integration against smooth kernels, logarithmic kernels, and Cauchy kernels—are given by the operators E, $\mathscr{T}$, and $\mathscr{G}$ in Eqs. (3.3)–(3.5).

Consider the discretization of E first. Since $e(\alpha, \alpha', t)$ is smooth and periodic in α and α', either the trapezoidal rule or the alternating point trapezoidal rule [45] yield spectral accuracy,

$$E[\mu]_j \approx \frac{h}{\pi}\sum_{l=0}^{N-1}\mu_l e_{jl} \qquad \text{trapezoidal rule} \quad (4.8)$$

$$\approx \frac{2h}{\pi}\sum_{\substack{l=0\\ l+jodd}}^{N-1}\mu_l e_{jl} \quad \text{alternating point rule,} \quad (4.9)$$

where $e_{jl} = e(jh, lh, t)$ and $h = 2\pi/N$.

In the diffusion integral equation, the only integral that appears is of type E. There, the appropriate kernel e on the interface Γ_q is given by

$$e(\alpha, \alpha_q', t) = \frac{2\pi}{L_q}\left(\frac{\partial}{\partial n(\alpha_q')}\log|z(\alpha_q', t) - z(\alpha, t)| + 1\right), \quad (4.10)$$

where q denotes the interface and the integral is taken over all the interfaces. In this case, we use the trapezoidal rule to obtain

$$K[\phi]_j^m = \frac{1}{2\pi}\int_\Gamma \phi(s')\left[\frac{\partial}{\partial n(s')}\log|z(s') - z_j^m| + 1\right]ds' \approx \frac{1}{2\pi}\sum_{q=1}^{p}\frac{h_q}{L_q}\sum_{l=0}^{N_q-1}\phi_l^q\left[\frac{\partial}{\partial n_l^q}\log|z_l^q - z_j^m| + 1\right], \quad (4.11)$$

where $h_q = 2\pi/N_q$ is the grid spacing on the qth interface. Further, $\phi_l^q = \phi(lh_q)$, $n_l^q = n(lh_q)$ and $z_l^q = z(lh_q)$. The self-induction point $q = m$, $l = j$ is computed by

$$\frac{\partial}{\partial n_j^m}\log|z_j^m - z_l^m| \equiv \frac{1}{2}\kappa_j^m = \frac{\pi}{L_m}\theta_{m,\alpha_j}. \quad (4.12)$$

We also implemented the alternating point rule for the diffusion integrals and found little difference in the performance of GMRES.

In the elasticity integral equations (2.37), all three types of integral operators appear. Here, we use a form of the alternating point rule to compute all of them, including those of type E. The smooth kernels that appear are given by

$$r_{,l'}r_{k'}, \frac{1}{r}\frac{\partial r}{\partial n'}, \tag{4.13}$$

where $r = |z(\alpha') - z(\alpha)|$ and $r_{,j'} = \partial r/\partial x_j(\alpha')$. We also tried the trapezoidal rule to compute the smooth integrals and found little difference in the performance.

We now describe the quadrature of the other two types of integral operators. First, consider the discretization of $\mathscr{T}$. Write

$$\begin{aligned}\mathscr{T}[\mu](\alpha,t) &= \frac{1}{\pi}\int_0^{2\pi}(\mu-\overline{\mu})\log|z(\alpha')-z(\alpha)|\,d\alpha' \\ &\quad + \frac{\overline{\mu}}{2\pi}\int_0^{2\pi}\log|z(\alpha')-z(\alpha)|\,d\alpha' \qquad (4.14)\\ &= -\frac{1}{\pi}\int_0^{2\pi}\xi\partial_{\alpha'}\log|z(\alpha')-z(\alpha)|\,d\alpha' \\ &\quad + \frac{\overline{\mu}}{2\pi}\int_0^{2\pi} g(\alpha,\alpha')\,d\alpha', \qquad (4.15)\end{aligned}$$

where $\xi_{,\alpha} = \mu - \overline{\mu}$ and integration by parts has been performed on the first integral. The function g, defined by

$$g(\alpha,\alpha',t) = \log\frac{|z(\alpha',t)-z(\alpha,t)|}{2|\sin((\alpha'-\alpha)/2)|}, \tag{4.16}$$

is a smooth periodic function of α, α'. And so, the second-integral in Eq. (4.15) is computed with spectral accuracy using the alternating point rule. The first integral can be written in the form

$$\begin{aligned}&-\frac{1}{\pi}\int_0^{2\pi}\xi\partial_{\alpha'}\log|z(\alpha)-z(\alpha')|\,d\alpha' \\ &\quad = \mathrm{Re}\left\{\frac{1}{\pi}\int_0^{2\pi}\xi\frac{z_{,\alpha'}}{z(\alpha)-z(\alpha')}\,d\alpha'\right\} \qquad (4.17)\\ &\quad = \mathrm{Re}\{\mathscr{G}[\xi](\alpha,t)\}. \qquad (4.18)\end{aligned}$$

Thus, the quadrature of the first integral in (4.15) can be reduced to the quadrature of $\mathscr{G}$. This is done using the alternating point rule, as it is now well known that this rule yields spectral accuracy when applied to Cauchy kernels [45]. Consequently, $\mathscr{G}$ is approximated by

$$\mathscr{G}[\mu]_j \approx \frac{2h}{\pi}\sum_{\substack{k=0\\ k+jodd}}^{N-1}\mu_k\frac{z_{,\alpha_k}}{z_j - z_k}. \tag{4.19}$$

We note that an alternative approach to computed $\mathscr{T}$ is given by using the small-scale decomposition Eq. (3.12), where the leading Hilbert transform is computed using the discrete Fourier transform and the smooth integral term E_1 is computed using the alternating point rule. In practice, we find the method (4.15), (4.18), and (4.19) to yield slightly faster convergence using GMRES. Moreover, since the logarithmic kernel is only applied to the components of the tractions $t_l(\alpha)$ and since $\bar{t}_l = 0$, the second integral in Eq. (4.15) need not be computed and the result is solely evaluated by using Eqs. (4.18) and (4.19). Therefore, we approximate

$$\begin{aligned}&\int_\Gamma t(s')\log|z(s')-z_j^m|\,ds' \approx \\ &\qquad \sum_{q=1}^{p}\frac{L_q h_q}{\pi}\sum_{\substack{k=0\\ k+jodd}}^{N-1}\xi_{l,k}^q\mathrm{Re}\left\{\frac{z_{,\alpha_k}^q}{z_j^m - z_k^q}\right\},\end{aligned} \tag{4.20}$$

where $\xi_{l,k}^q = \xi_l(kh_q)$ and on the continuous level, $\xi_{l,\alpha_q} = t_l(\alpha_q)$.

The most singular kernel in the elasticity integral equations is of Cauchy type when z, z' lie on the same interface. With $z = z_j^m$, it is given by

$$\frac{n_l' r_{,k'} - n_k' r_{,l'}}{|z' - z_j^m|} = \frac{2\pi\varepsilon_{lk3}}{L}\mathrm{Re}\left\{\frac{z_{,\alpha'}}{z' - z_j^m}\right\}, \tag{4.21}$$

where $l, k = 1, 2$, and ε_{lk3} is as in Section 3.2. Thus it is of type $\mathscr{G}$ and, so, the alternating point quadrature is used to compute this integral with spectral accuracy; i.e.,

$$\begin{aligned}&\int_\Gamma \mu(s')\frac{1}{r}(n_l' r_{,k'} - n_k' r_{,l'})\,ds' \approx \\ &\qquad -\varepsilon_{lk3}\sum_{q=1}^{p}2h_q\sum_{\substack{i=0\\ i+jodd}}^{N-1}\mu_i^q\mathrm{Re}\left\{\frac{z_{,\alpha_i}^q}{z_j^m - z_i^q}\right\},\end{aligned} \tag{4.22}$$

where $\mu_i^q = \mu(ih_q)$.

Note that if the integrals in Eqs. (4.20), (4.22) are only taken over a single interface Γ_m, as is the case for the precipitate equations, then on the right-hand sides, take $q = m$ and omit the sum over q. Finally, the integral term in the normal velocity V_i in Eq. (2.12) is also of type $\mathscr{G}$ and, so, alternating point quadrature is employed to compute it as well.

4.3. Filtering

In our scheme, we employ two types of filtering. We use a high (25th) order Fourier filter Π to damp the highest modes and suppress aliasing errors [6, 17]. We also use Krasny filtering [28] to prevent the accumulation of roundoff errors during the computation.

In principle, aliasing instabilities can be controlled by simply increasing the spatial resolution, but this is expensive. Instead we apply Π. In particular, we use

$$\hat{\Pi}[f](k) = e^{-10(|k|/N)^{25}}\hat{f}(k). \tag{4.23}$$

This filtering determines the overall accuracy of our method and so the formal accuracy is $O(h^{25})$. Certainly an infinite order filter could have been used, but we found Π to be sufficient.

In addition to the Fourier smoothing, we also use Krasny filtering. That is, we set to 0 all Fourier modes below an error tolerance ε. It is applied at the same time as Π and we choose ε to be slightly above the roundoff level, i.e., $\varepsilon = 10^{-11}$ in double precision. Krasny filtering prevents the accumulation of roundoff error during the computation. Hereafter, the combination of Fourier smoothing and Krasny filtering is denoted by Π.

We find that filtering is crucial to ensure the rapid convergence of GMRES applied to the elasticity integral equations. This is for two reasons. First, filtering is necessary to control aliasing errors that occur when the discrete elasticity integral equations are evaluated. For example, if filtering is used for a given mesh spacing and rather complex interface(s), the number of iterations required to solve the elasticity integral equations typically drops significantly when compared to the case where no filtering is performed. This is shown in Fig. 2 in Section 5. The number of iterations also drops when the mesh size is decreased, suggesting that the difficulty is due in large part to aliasing and resolution. We note that filtering is also necessary to remove aliasing errors that arise when the tangent angles are updated via Eq. (4.5) [17].

Second, even if the interface is well-resolved, it is important to filter the right-hand side b of the discrete integral equations for elasticity as well as the approximate right-hand sides (also denoted by b) that are computed during the iteration process. This is because our preconditioning involves the application of an operator $\mathscr{L}^{-1}$ to b. And, roughly speaking, $\hat{\mathscr{L}}^{-1} = O(|k|)$, as seen in Appendix C. Thus, errors in $\hat{b}$ are amplified by k upon multiplication by $\mathscr{L}^{-1}$, i.e., $\widehat{\mathscr{L}^{-1}b} = O(|k|\hat{b})$. This is a remnant of the original ill-conditioning. We find that by filtering b, the number of GMRES iterations is typically reduced.

4.4. GMRES Matrix Iteration

Discretizing the diffusion and elasticity boundary integral equations leads to two finite-dimensional linear systems $Ax = b$ that must be solved at each time step. In both cases, the resulting matrix systems are nondefinite and nonsparse. Therefore, we use the GMRES iterative method [44] to solve them up to a given error tolerance tol. The full matrices are never stored as GMRES requires, only matrix–vector products (Ax).

There are three important features involved with the application of GMRES: (1) the evaluation of matrix–vector products, (2) preconditioning, and (3) initial guess.

(1) *Matrix-Vector Products.* Currently, we use direct summation to compute Ax. That is, the quadratures developed in Section 4.2 are implemented as written. Consequently, the operation count of computing Ax is essentially $O(N^2)$, where N is the total number of grid points. This count could be reduced to $O(N)$ or $O(N \log N)$ using the fast multipole method (FMM) to evaluate the quadratures [13]. The FMM has already been applied to the diffusion quadratures [11] and can also be applied to the elasticity quadratures [12]. At our current resolutions we found it sufficient to use direct summation although it is expensive. In the future, we will implement the FMM for the diffusion and elasticity integral equations as we intend to perform computations involving large numbers of particles.

(2) *Preconditioning.* Rather than solving the system $Ax = b$, one solves a modified system,

$$M^{-1}Ax = M^{-1}b, \tag{4.24}$$

where the new iteration matrix $M^{-1}A$ has eigenvalues clustered near 1. This is known as left preconditioning, where M is the preconditioning matrix. In addition, given any r it must be easy to solve $Mz = r$ for z.

The modified systems for diffusion and elasticity are given by their SSDs given in Sections 3 and 3.2. In the diffusion case, this means that we should take M to be the discretization of $\mathscr{L}$ given in Eq. (3.19). Solving $Mz = r$ then requires only the solution of a $p \times p$ system, where p is the number of particles. This relatively small system is solved by Gaussian elimination with partial pivoting. The analysis presented in Section 3 shows that $M^{-1}A$ has the form $I + \mathscr{L}^{-1}R$, where the eigenvalues of $\mathscr{L}^{-1}R$ accumulated at 0 (as $N \to \infty$) and so asymptotically (in N), the eigenvalues of $M^{-1}A$ cluster near 1.

In the elasticity case, rather than solving the system $Ax = b$, one solves the modified system $\Pi A \Pi x = \Pi b$, where Π is the filtering described in Section 4.3. In addition, we define M through the Fourier coefficients of the $\mathscr{L}$ given in Eqs. (C.56) and (C.57) as shown in Appendix C. That is, the discrete Fourier coefficients of M are equal to the continuous Fourier coefficients of $\mathscr{L}$ up to the Nyquist mode $N/2$. Then, M^{-1} is computed by inverting the 4×4 matrix in Fourier space for each interface Γ_j. Note that in solving $Mz = r$ here, we really obtain z by $z = \Pi M^{-1} \Pi r$.

Finally, the analysis in Section 3 shows that the eigenvalues of $M^{-1}A = I + \mathscr{L}^{-1}R$ cluster near 1, asymptotically. This result is still true if the system is modified by filtering as above.

(3) *Initial Guess.* In order to obtain a good initial guess for GMRES, we extrapolate from solutions obtained by GMRES at previous time steps. We use up to fifth-order extrapolation in time and so we need to keep the previous five solutions for both the diffusion and elasticity equations. Thus, we can only use this extrapolation beyond the fifth time step. At earlier time steps, we use first-order extrapolation. At $t = 0$, we use 0 as a starting guess. After the fifth step in a typical calculation, the error in the first step of the iteration for either diffusion or elasticity is $O(10^{-6})$.

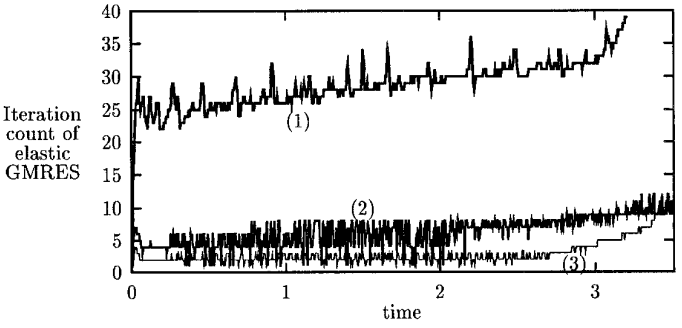

FIG. 2. The GMRES iteration count for the elastic solver with (1) no preconditioning, (2) small scale preconditioning, (3) small-scale preconditioning with filtering during iteration. Data used are: $\mu^{\mathrm{P}} = 0.5$, $\nu^{\mathrm{P}} = \nu^{\mathrm{M}} = 0.2$, $Z = 3000$, $J = 10$, $\varepsilon^0_{11} = -\varepsilon^0_{22} = 0.01$, $\varepsilon^0_{12} = 0$, $\Delta t = 0.005$, $N = 256$, tol $= 10^{-10}$, $\varepsilon = 10^{-11}$. The initial precipitate shape is a circle of radius 1.

5. CONVERGENCE TESTS

Our numerical scheme for tracking microstructural evolution consists of three parts: (1) an elastic solver to compute G^{el} on each precipitate–matrix interface, (2) a diffusion solver that computes the normal velocity on each interface, and (3) a time stepping routine to evolve the interfaces in time. The numerical implementation and analysis associated with steps (2) and (3) are already well documented [11, 17]. Here, we focus on the performance of the elastic solver. Unless otherwise stated, all numerical tests in this section are performed using a single precipitate under an applied shear ($\varepsilon^0_{11} = -\varepsilon^0_{22} = 0.01$, $\varepsilon^0_{12} = 0$) with elastic properties $\mu^{\mathrm{P}} = 0.5$, $\nu^{\mathrm{P}} = \nu^{\mathrm{M}} = 0.2$, and $Z = 3000$. There is no misfit strain. Except for the amount of inhomogeneity μ^{P}, these parameters are appropriate for nickel-based alloys. The precipitate is initially circular with radius $r = 1$. The far-field flux is $J = 10$. The GMRES error tolerance is tol $= 10^{-10}$ and the filter level is $\varepsilon = 10^{-11}$. Finally, to recover the (x_1, x_2) position of the interface from the $\theta - L$ formulation, the endpoint is evolved as discussed in Section 2.4.

5.1. The Effect of Preconditioning and Filtering

In Fig. 2, we present the iteration count of GMRES versus time for the discretized elasticity integral equations using different preconditioning strategies. The number of grid points is $N = 256$ and the time step is $\Delta t = 0.005$. The curve marked (1) shows the result without preconditioning. The iteration count is at least 25 and steadily increases as the precipitate shape evolves. Curve (2) shows the result with the SSD preconditioner discussed in Section 3.2. We find a much lower iteration count. The count is consistently between 5–10 and increases slowly as the shape evolves. Curve (3) shows the result with the SSD preconditioning *and* the filtering Π as described in Sections 4.3 and 4.4. The iteration count is further reduced as the filter prevents the accumulation and amplification of roundoff errors in addition to suppressing aliasing errors. Up to time $t = 3$, the count is consistently around 3 which is better than a factor of 8 improvement over curve (1) and is at least a factor of 2 improvement over curve (2). The improvement is even more dramatic at later times where it is simply not feasible to perform computations without preconditioning. After time 3, the iteration count of curve (3) rises rapidly to that of curve (2). This is due to a lack of numerical resolution. Doubling the number of grid points reduces the iteration count back to approximately 3 at these times. On the other hand, a similar doubling of the number of grid points using just the SSD preconditioning curve (2) does not yield as dramatic a reduction in the iteration count at these same times.

5.2. Error Analysis

In this section, we analyze the spatial, temporal, filtering, and GMRES tolerance errors in the computed solutions to the elastic fields. We begin with the errors in space.

Spectral Accuracy in Space

We use a computation with $N = 2048$ to approximate the exact solution in order to measure the errors at other spatial resolutions. The precipitate is initially circular with radius $r = 2.5$. Further, $\Delta t = 0.005$. All other parameters are fixed as before. We compare the $N = 2048$ solution to those with $N = 256$, 512, and 1024. The error is defined as the largest error among all common points at each time step; i.e.,

$$e_N(t) = \max_j |f_j(t; N) - f_j(t; 2048)|,$$

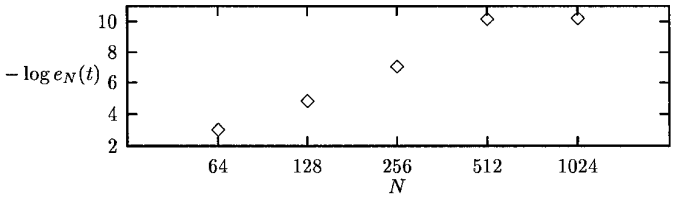

FIG. 3. Convergence test in space. Errors are measured relative to the $N = 2048$ result at time $t = 4$. Data used are: $\mu^P = 0.5$, $\nu^P = \nu^M = 0.2$, $Z = 3000$, $J = 10$, $\varepsilon^0_{11} = -\varepsilon^0_{22} = 0.01$, $\varepsilon^0_{12} = 0$, $\Delta t = 0.005$, tol $= 10^{-10}$, $\varepsilon = 10^{-11}$. The initial precipitate shape is a circle of radius 2.5.

for N nodes, where f can be either one of the components of displacement (u_1, u_2) or traction (t_1, t_2). Figure 3 shows the error in t_1 as a function of N at the time $t = 4.0$. This curve is representative of the other three choices. The error is plotted on a negative logarithm (base 10) scale so the vertical axis shows the number of accurate digits. For $N = 512$, there are 10 digits of accuracy. Increasing N beyond 512 does not improve the accuracy as the GMRES error tolerance tol $= 10^{-10}$ governs the overall accuracy. These results confirm that the method is spectrally accurate in space.

Second-Order Accuracy in Time

Although the equations of elastostatics are used to compute the elastic fields, the elastic fields vary smoothly in time through the evolution of the precipitates. Since second-order methods are used to update the precipitate shapes, we expect to see second-order convergence in the elastic fields. This is verified as follows. We use a computation with $\Delta t = 0.00125$ to approximate the exact solution in order to measure the temporal errors. The precipitate is initially circular with radius $r = 5$. Further, $N = 256$. All other parameters are fixed as before. We compare the $\Delta t = 0.00125$ solution to those with $\Delta t = 0.01$, 0.005, and 0.0025. As in the spatial case, the error is taken to be the maximum error on the grid at a common time, i.e.,

$$e_{\Delta t}(t) = \max_j |f_j(t; \Delta t) - f_j(t; 0.00125)|.$$

Figure 4 shows a representative plot of the time stepping error for t_1 as a function of time. The graph of $-\log e_{\Delta t}(t)$ uniformly increases by about 0.6 with each halving of Δt. This confirms the second-order accuracy in time.

Effect of Tolerance and Filter Levels

We have also investigated the effect of changing the tolerance and filter levels for the GMRES solver. We find that decreasing the tolerance level by an order of magnitude (with all other parameters fixed) leads to an order of magnitude decrease in the error. We find that the same holds true if the filter level ε is varied similarly.

6. NUMERICAL RESULTS

In this section, we use fully nonlinear simulations to study the role an inhomogeneous elastic medium plays in the diffusional growth/equilibration process. We refer to a system as growing if the far-field flux $J > 0$ and as equilibrating if there is no far-field flux, i.e., $J = 0$. In addition, we focus primarily on the case of one or two precipitates, although we present a computation involving 16 precipitates at the end of this section. As we will see, precisely analyzing the role of elasticity is quite complicated even for such a small number of precipitates. Additional results will be given in a forthcoming paper [25].

We begin by comparing the results of our nonlinear simulation with that from the linearized theory of a single growing precipitate.

6.1. Comparison with Linear Theory

Consider a single precipitate with an initial shape given by a perturbed circle, $r(\alpha, 0)e^{i\alpha}$, with radius

$$r(\alpha, 0) = R(0) + \mathrm{Re}\left[\sum_{k=1}^{\infty} b_k(0)e^{ik\alpha}\right], \tag{6.1}$$

where $|b_k(0)/R(0)| \ll 1$ for all k. We then expect that the growth of this precipitate in an elastically stressed matrix preserves $|b_k(t)/R(t)| \ll 1$ for at least short times. Following Leo and Jou [33], one can show that to first order in the perturbation, i.e., $O(b_k(t)/R(t))$, the velocity $v(\alpha, t) = \dot{r}(\alpha, t) = \dot{R}(t) + \mathrm{Re}\,[\sum_{k=1}^{\infty} \dot{b}_k(t)e^{ik\alpha}]$ can be found by solving the dynamical system for R and the b_k given by

$$\dot{x} = Ax, \tag{6.2}$$

where the vector $x = \{R, b_1, b_2, ...\}$ and A is an infinite-dimensional banded matrix that varies in time through

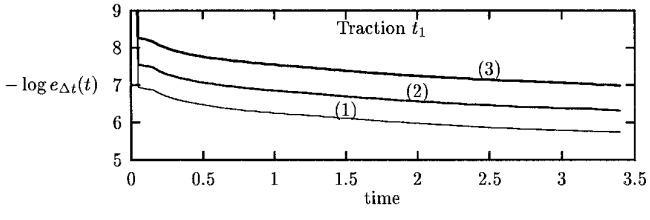

FIG. 4. Convergence test in time for (1) $\Delta t = 0.01$, (2) $\Delta t = 0.005$, (3) $\Delta t = 0.0025$. Errors are measured relative to the $\Delta t = 0.00125$ result. Data used are: $\mu^P = 0.5$, $\nu^P = \nu^M = 0.2$, $Z = 3000$, $J = 10$, $\varepsilon^0_{11} = -\varepsilon^0_{22} = 0.01$, $\varepsilon^0_{12} = 0$, $N = 256$, tol $= 10^{-10}$, $\varepsilon = 10^{-11}$. The initial precipitate shape is a circle of radius 5.

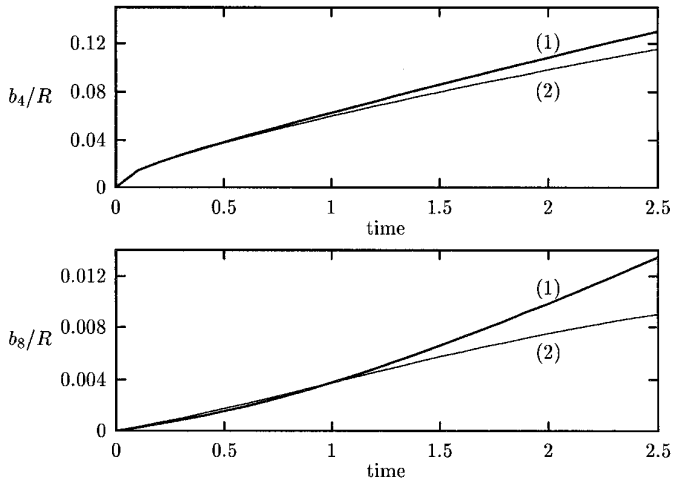

FIG. 5. Comparison of perturbation amplitudes for growth shapes calculated from (1) linear theory and (2) nonlinear numerical method. Data used are: $\mu^{\mathrm{P}} = 0.5$, $\nu^{\mathrm{P}} = \nu^{\mathrm{M}} = 0.2$, $Z = 3000$, $J = 10$, $\varepsilon^0_{11} = -\varepsilon^0_{22} = 0.01$, $\varepsilon^0_{12} = 0$, $\Delta t = 0.005$, $N = 256$, tol $= 10^{-10}$, $\varepsilon = 10^{-11}$. The initial precipitate shape is a circle of radius 1.

$R(t)$. We refer the reader to Appendix D for the full and rather complicated form of A. We point out two important features of A that differ from the pure diffusion case, i.e., the classical Mullins–Sekerka analysis [40] with isotropic surface energy and without elastic effects. First,

$$\dot{R} = a_{00}R + a_{02}b_2 + a_{04}b_4, \tag{6.3}$$

where $a_{00} = J/R^2$ is the usual Mullins–Sekerka term and a_{02} and a_{04} are elastically induced coefficients. Thus, unlike the classical case, R cannot be solved independently of the b_k. Second, due to the elastic effects, each perturbation amplitude generates up to four modes since

$$\dot{b}_k = a_{k,k-4}b_{k-4} + a_{k,k-2}b_{k-2} + a_{k,k}b_k + a_{k,k+2}b_{k+2} + a_{k,k+4}b_{k+4}. \tag{6.4}$$

In the classical case, only $a_{k,k}$ is nonzero. From Eq. (6.4), we see that the even and odd modes decouple. Moreover, since $R \equiv b_0$ explicitly appears in the $\dot{b}_2$ and $\dot{b}_4$ equations, this implies that typically $\dot{b}_2 \neq 0$ and $\dot{b}_4 \neq 0$ at time $t = 0$. Thus, even if b_2 and b_4 are zero at $t = 0$, they can become nonzero for $t > 0$. Elastically induced mode coupling typically causes all the even modes to eventually become nonzero. Odd modes, however, must be initially perturbed in order to deviate from zero. Further, as shown in [33], the off-diagonal terms $a_{j,k}$, with $j \neq k$, depend on the deviatoric part of the applied or misfit strain.[2] Thus, it is the deviatoric part of the misfit and/or the applied strain that breaks the circular symmetry of the diffusion.

An example of this type of behavior is given in Fig. 5 which shows the amplitudes b_4/R and b_8/R as a function of time for a growing particle under a far-field flux $J = 10$ and an applied shear $\varepsilon^0_{11} = -\varepsilon^0_{22} = 0.01$, $\varepsilon^0_{12} = 0$. Note that shear strains are purely deviatoric. There is no shape perturbation at $t = 0$ as the precipitate is initially a unit circle. There is no misfit strain. We do not show the b_2 mode as it happens to be identically zero for an applied shear strain [33]. The parameters are $\mu^{\mathrm{P}} = 0.5$, $\nu^{\mathrm{P}} = \nu^{\mathrm{M}} = 0.2$, and $Z = 3000$. The solution to the dynamical system (6.2) is computed using fourth-order Runge–Kutta with $\Delta t = 0.005$ and is shown in the curves marked (1). The curves marked (2) show the result from our fully nonlinear numerical scheme with $N = 256$, tol $= 10^{-10}$, $\varepsilon = 10^{-11}$, and $\Delta t = 0.005$. The endpoints of the interface are evolved to recover the (x_1, x_2) positions from the (θ, L) formulation. We see that b_4 and b_8 are initially zero since there is no initial perturbation in the shape. However, they steadily grow in time as the shape evolves. The linearized solution (1) compares well to the nonlinear numerical solution (2) for short times. At later times, as the solution grows into the nonlinear regime, the linearized solution overpredicts the growth of the 4 and 8 modes.

A natural question concerns the stability of these growing shapes. In the case without elasticity, classical analysis [40] shows that circles are stable growing shapes. In particular, if $R(t) \leq R_c(k)$, where $R_c(k) = k(k^2 - 1)/(J(k - 2))$ is the Mullins–Sekerka critical radius, then the kth perturbation mode decays in time relative to the growing radius $R(t)$ [40]. Note that the $k = 2$ mode never becomes unstable. In the case with elasticity, such a simple criterion is not possible due to the complicated mode coupling. Nevertheless, in the elastic case, we observe stable growing noncircular precipitates. This was predicted from linear theory by Johnson [19] and Leo and Jou [33]. In Fig. 6, we present evidence confirming the existence of such stably growing shapes using our fully nonlinear code. The parameters are the same as in Fig. 5, except that the far-field shear and flux are both reduced by a factor of 10 and $N = 128$. The amplitude b_4/R is shown as a function of base radius R for four different computations with varying initial conditions. The curve marked (1) corresponds to the growth path of an initially unperturbed circle of radius 2. Note that the slope of this curve is positive, indicating that the growth shape increasingly deviates from a circle as R increases. Curves (2) and (3) show the growth paths for initial 1% perturbations in the fourth mode of the circle of radius 2. Note how rapidly these curves collapse onto the path of (1). Curves (4) and (5) correspond to the growth paths of 1% perturbations in the fourth mode of a circle with radius 6. These curves also eventually collapse onto the growth path of (1). This indicates that (1) corresponds to a stable growing noncircular shape.

We make two comments here. First, for this situation, the dynamical system (6.2) and the nonlinear simulation

[2] Like any tensor field in 2D, a strain field ε_{ij} can be decomposed into a dilatational part $\frac{1}{2}\varepsilon_{kk}\delta_{ij}$ and a deviatoric part $\varepsilon_{ij} - \frac{1}{2}\varepsilon_{kk}\delta_{ij}$.

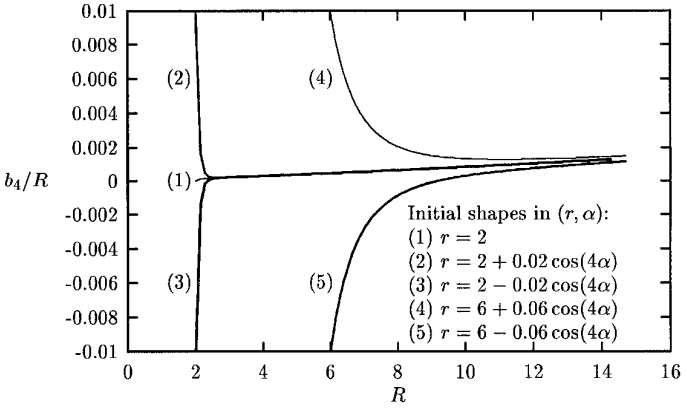

FIG. 6. Evidence for a stable noncircular growth shape using the nonlinear numerical method. Curve (1) corresponds to the growth path of an initial circle of radius 2. Curves (2) and (3) correspond to the paths from an initial 1% perturbation of the circle of radius 2. Curves (4) and (5) correspond to the paths from an initial 1% perturbation of the circle of radius 6. Data used are: $\mu^{\mathrm{P}} = 0.5$, $\nu^{\mathrm{P}} = \nu^{\mathrm{M}} = 0.2$, $Z = 3000$, $J = 1$, $\varepsilon^0_{11} = -\varepsilon^0_{22} = 0.001$, $\varepsilon^0_{12} = 0$, $\Delta t = 0.005$, $N = 128$, tol $= 10^{-10}$, $\varepsilon = 10^{-11}$.

yield the same results, up to graphical resolution. Second, for these parameters, the Mullins–Sekerka critical radius for the fourth mode is $R_c(4) = 30$. Thus, at the end of the computation shown in Fig. 6, the precipitate has a radius less than half that of $R_c(4)$ and so in the *absence* of elasticity, any perturbation in the fourth mode would decay relative to R; i.e., b_4/R would decrease. This is in contrast to what we observe in Fig. 6 with elasticity, where b_4/R actually increases even though the growing noncircular shape is stable. We do not show the actual shape of the precipitate here, because at these early times it is indistinguishable from a circle to graphical resolution.

The situation becomes much more delicate as the precipitate radius nears R_c. This is shown in Fig. 7, where b_4/R is shown again as a function of R. The parameters are the same as in Fig. 6, except that the flux is increased by a factor of 5, i.e., $J = 5$. This makes $R_c(4) = 6$. Three curves are shown, each corresponding to different initial conditions. The curve marked (1) shows the growth path from an initially unperturbed circle of radius 2. The curves (2) and (3) show the growth paths resulting from 1% perturbations in the fourth mode of the circle of radius 2. We see that roughly for $R < R_c$, the paths of (2) and (3) tend to converge to that of (1). However, when $R > R_c$, the growth paths steadily diverge, indicating that the perturbation has become unstable. Because of the complicated mode coupling, it is difficult to identify the precise value of R for which the fourth mode becomes unstable in the presence of elasticity. We refer the reader to [33] for further details.

6.2. Simulations in the Fully Nonlinear Regime

In this section, we present numerical simulations of precipitate growth well into the nonlinear regime. We divide our results into four cases: (1) one precipitate, (2) two precipitates of equal sizes, (3) two precipitates of different sizes, and (4) multiple precipitates.

Case 1: *One Precipitate*

Consider the case of a single precipitate growing by diffusion in an elastic matrix. This situation provides one of the simplest contexts in which to analyze the effect of elastic stresses on morphological development. In Fig. 8, we present several examples of such growing shapes in an applied strain field. In case (1), we do not consider misfit, although we note there is an equivalence between misfit and applied strain [41]. Misfit is considered in cases (2), (3), and (4). Unless otherwise indicated, the precipitates are initially circular with radius 1. The elastic parameters are $\nu^{\mathrm{M}} = \nu^{\mathrm{P}} = 0.2$ and $Z = 3000$. The far-field flux is $J = 10$. The GMRES error tolerance is tol $= 10^{-10}$ and the filter level is $\varepsilon = 10^{-11}$. Typically, the computations are started with $N = 256$ and N is increased during the computation to maintain resolution. Finally, the endpoint of the interface is evolved to reconstruct the (x_1, x_2) position from the $\theta - L$ formulation.

In the *absence* of elastic effects, the initial circle of radius 1 will grow while keeping its circular shape. As we have seen, the deviatoric parts of the elastic fields break this circular symmetry. We now examine the long time evolution. In Figs. 8a and b we show precipitates grown with an applied shear strain $\varepsilon^0_{11} = -\varepsilon^0_{22} = 0.01$, $\varepsilon^0_{12} = 0$. The difference between a and b is that in a we have $\mu^{\mathrm{P}} = 0.5$, while in b we have $\mu^{\mathrm{P}} = 2$. The precipitate is referred to as *hard,* with respect to the matrix, if $\mu^{\mathrm{P}} > 1$ and analogously as *soft* if $\mu^{\mathrm{P}} < 1$. Further, time ranges from $t = 0$ to $t = 160$ and the interface is plotted very 20 time units. The time

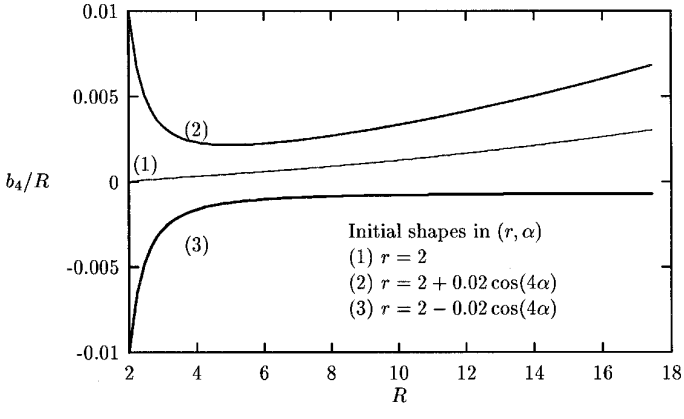

FIG. 7. Evidence for unstable growth paths using the nonlinear numerical method. Curve (1) corresponds to the growth path of an initial circle of radius 2. Curves (2) and (3) correspond to the paths from an initial 1% perturbation of the circle of radius 2. Data used are: $\mu^{\mathrm{P}} = 0.5$, $\nu^{\mathrm{P}} = \nu^{\mathrm{M}} = 0.2$, $Z = 3000$, $J = 5$, $\varepsilon^0_{11} = -\varepsilon^0_{22} = 0.001$, $\varepsilon^0_{12} = 0$, $\Delta t = 0.005$, $N = 128$, tol $= 10^{-10}$, $\varepsilon = 10^{-11}$.

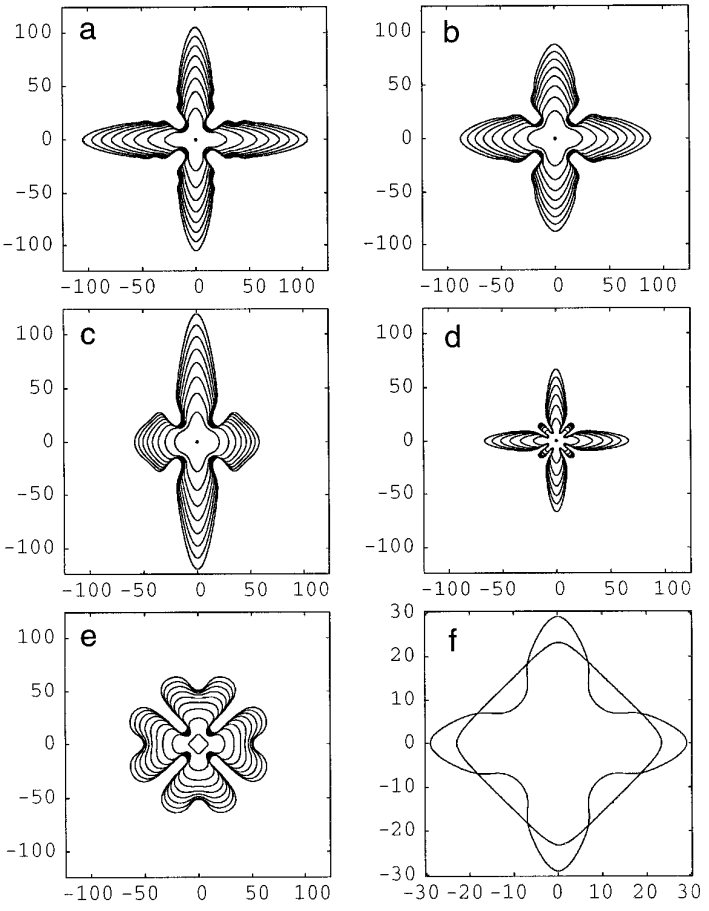

FIG. 8. A series of precipitate shapes under different growth conditions. In (a)–(c) the flux $J = 10$. (a) shows a soft precipitate ($\mu^P = 0.5$) growing in an applied shear $\varepsilon^0_{11} = -\varepsilon^0_{22} = 0.01$, $\varepsilon^0_{12} = 0$. N ranges from 256 to 4096. (b) shows a hard precipitate ($\mu^P = 2$) growing under the same conditions. (c) shows a soft precipitate ($\mu^P = 0.5$) growing in an applied uniaxial tension $\varepsilon^0_{11} = 0.015$, $\varepsilon^0_{22} = \varepsilon^0_{12} = 0$. All other parameters are as in (a). (d) shows the same case as (a), but with the far-field flux $J = 100$. (e) shows shape evolution in the absence of elastic fields. The initial shape is the time $t = 3$ shape of (a). (f) shows the equilibrating shape that results from coarsening ($J = 0$) of the $t = 20$ shape in (a). See text for other parameters.

step is $\Delta t = 0.01$ and N varies from 256 at $t = 0$ to $N = 4096$ for $t \geq 80$, for a; $N = 2048$ for $t \geq 80$ for b. By checking the precipitate area, we found it was sufficient to keep $\Delta t = 0.01$ fixed throughout these computations to ensure three digits of accuracy in the area at time $t = 160$.

In both Figs. 8a and b we observe the development of four symmetric dendrite arms which align along the principal directions of the applied strain. By principal directions, we refer to the eigenvector directions of the applied strain matrix. For the above shear, these directions are the coordinate directions e_1 and e_2. Analogously, the term principal strains refers to the eigenvalues of the strain matrix. The energy density G^{el} depends only on the magnitude of the principal applied strains and not on their signs. Thus, the morphological development does not distinguish between tension (positive principal strain) and compression (negative principal strain). This is why the dendrite arms grow in *both* strain directions and are symmetric (since $|\varepsilon^0_{11}| = |\varepsilon^0_{22}|$). Symmetry is not enforced by the code and is used as an additional check on the accuracy of the computational solution. Note that the structure of the dendrite arms is rather different for the precipitates in a and b. The dendrite arms are more slender for the soft precipitate, a, than for the hard precipitate, b. Moreover, a regular pattern of "wiggles" appears to be forming on the dendrite arms of the soft precipitate. These wiggles may be the beginnings of side-branching. Although such wiggles are not yet present in the hard precipitate, there is a bump on each side of the dendrites. It seems possible that wiggles will develop later in time in the hard precipitate as well.

We now consider a different applied field. In Fig. 8c, we consider the same soft precipitate as in a, except now there is an applied uniaxial tension $\varepsilon^0_{11} = 0.015$ and $\varepsilon^0_{22} = \varepsilon^0_{12} = 0$. The interface is plotted from time $t = 0$ to $t = 160$ at intervals of 20 time units. The time step is still $\Delta t = 0.01$ and N varies from 256 at $t = 0$ to $N = 4096$ for $t \geq 150$. The principal applied strain directions are still e_1 and e_2 and so we again see dendrite arms aligned along these directions. However, since the magnitudes of the principal applied strains are different, we see that the arms are elongated in the e_2 direction which is perpendicular to the direction of largest principal strain.

Next, consider the effect of increasing the far-field flux. In Fig. 8d, we show a precipitate growing under exactly the same conditions as in a, except that the far-field flux J is increased by a factor of 10, i.e., $J = 100$. The interface is plotted from $t = 0$ to $t = 6.0$ every 1 time unit. The time step is reduced to $\Delta t = 0.001$ and N ranges from 256 at $t = 0$ to $N = 4096$ for $t \geq 2.2$. We again see the development of a dendritic-type structure where the primary arms are aligned along the principal strain directions. However, additional arms form *between* the primary arms and wiggles form along the primary arms themselves (near the base). The additional arms occur because by increasing J, the Mullins–Sekerka critical radii are reduced so that the elastically induced eighth mode perturbation becomes unstable and influences the shape before the induced fourth mode perturbation completely dominates the nonlinear evolution. As one can see from Fig. 8d, however, the growth of these small, additional arms slows down in time relative to the growth of the primary arms of the precipitate. This is due to a nonlinear elastic stabilization. At late times, the fourth mode dominates the evolution. This will be discussed further in [25].

Now, consider the effect of removing the elasticity. As noted above, in presence of an isotropic surface energy and

in the absence of elasticity, a circle will grow maintaining its circular shape. So, rather than starting from a circle, we take the $t = 3$ shape from Fig. 8a as the initial condition. This contains elastically induced perturbations in the $2k$ modes for $k \geq 2$, with the fourth mode dominating. The resulting evolution, in the absence of elasticity ($Z = 0$), is shown in Fig. 8e. Time ranges from the initial $t = 3$ to $t = 160$ and the interface is plotted at $t = 3$, $t = 20$, and every 20 time units thereafter so the shapes can be directly compared with those in Fig. 8a. The time step $\Delta t = 0.01$ and N ranges from 256 to $N = 512$ for $t \geq 30$. We note that fewer grid points are required to resolve the diffusion field as compared to the elastic fields. There is an overall fourfold symmetry because of the perturbation in the data at $t = 3$. However, in contrast to the precipitate grown in Fig. 8a, there are no well-defined dendrite arms and there is significant tip splitting. Also, the wiggles observed on the dendrite arms in a are not present in any form here. Thus, this shape is very different from the shapes of precipitates grown in the presence of an elastic field.

One could also compare the shapes grown under the influence of an *anisotropic* surface tension in the absence of elasticity to those in Figs. 8a–d. Like elasticity, surface tension anisotropy breaks the circular symmetry of the diffusion and introduces preferred directions of growth. It is therefore not surprising to notice that surface tension anisotropy produces dendritic shapes somewhat similar to those we observe in Figs. 8a–d [3].

Finally, we consider the difference between the growth shapes of Figs. 8a–d and the equilibrium shapes. An equilibrium shape is the shape that minimizes the total energy W_{tot} given in Eq. (2.52) among all shapes with a given area. It is characterized by a constant composition along the interface. Because W_{tot} is nonincreasing in time (see Eq. (2.69)), an equilibrium shape can be computed dynamically by taking any intial precipitate shape, with appropriate area, setting the flux $J = 0$ and evolving in time until the composition is constant along the interface. The resulting equilibrium shape is independent of the original shape and depends only on the elastic parameters and the area of the initial precipitate. In Fig. 8f, we show how the precipitate given by the $t = 80$ shape from a evolves during the equilibration process. The time step is $\Delta t = 0.01$ and $N = 1024$ throughout the computation. All other parameters are the same as in Fig. 8a.

Two plots are overlayed in Fig. 8f. The dendritic shape is the $t = 20$ solution from Fig. 8a. As the dendrite equilibrates, the arms decay and the valleys grow to form the squarish shape that is pictured (after 400 time units). This resulting squarish shape is typical of many other calculations of equilibrium shapes [37, 49]. Moreover, since the composition on the interface shown at $t = 400$ in Fig. 8f is essentially constant, it is truly an equilibrium shape. We also note that since the equilibrium shape depends only on the elastic parameters and the area, the growth shapes shown in Fig. 8a at a time T and in 8d at time $T/10$ will equilibrate to exactly the same shape—an appropriately sized ''square-oid'' of the type shown in f.

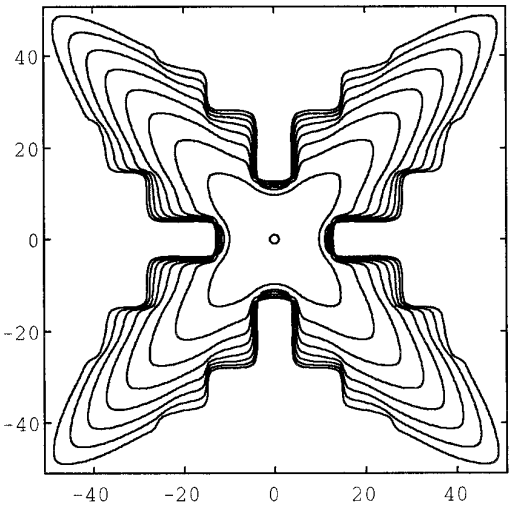

FIG. 9. A precipitate growing in an anisotropic, homogeneous elastic media. Interfacial positions are plotted every 10 time units from $t = 0$ to $t = 80$. $J = 10$, N ranges from 512 to 8192 and $\Delta t = 0.01$. The elastic fields are calculated using the elastic solver developed by Voorhees *et al.* [52, 46, 47] with parameters $L = 1$, $C_{11} = 1.98$, $C_{12} = 1.18$, $C_{44} = 1$.

Differences between growth shapes and coarsening shapes have been observed experimentally by Yoo, Yoon, and Henry [57]. They studied the microstructure formed in a nickel-aluminum-titanium alloy as a function of nucleation density. At sufficiently small nucleation densities where there is a large mass flux into each precipitate, dendritic shapes are observed. However, at medium to high nucleation densities where there is a small mass flux into each precipitate, Yoo *et al.* observe cuboidal shapes (square-oids in 2D).

In the experiments of Yoo *et al.*, there was no applied strain and there is significant elastic anisotropy. Thus, comparisons with our results are strictly qualitative. However, it is interesting to note that our computations often yield shapes similar to those observed in simulations of *anisotropic*, *homogeneous* elastic systems. In isotropic media, misfits and applied strains with nonzero deviatoric parts appear to have a symmetry breaking effect similar to that of elastic anisotropy. For example, using our nonstiff time integration scheme, we simulated the evolution of a single growing precipitate using the homogeneous, cubic anisotropic elasticity solver developed by Voorhees *et al.* [53, 47, 48]. The result is given in Fig. 9. The initial condition is a unit circle and the interface is plotted from $t = 0$ to $t = 80$ every 10 time units. The parameters are $L = 1$, $C_{11} = 1.98$, $C_{12} = 1.18$, $C_{44} = 1$, where we refer the reader to [53] for their meaning. Initially, $N = 512$ and N is gradually

increased to $N = 8192$ for $t \geq 60$. The time step is $\Delta t = 0.01$. We again find dendritic shapes with an evidence of side-branching. The dendrite arms now form in the elastically hard directions [53]. Moreover, the growth shapes recently reported by Wang and Khachaturyan [55] for a similar system appear to be early time versions of those we show in Fig. 9.

Finally, we note that the computations presented in Figs. 6, 7, 8, and 9 were performed on a CRAY C90 in vector mode. The computations shown in Figs. 6 and 7 are rather inexpensive with each taking less than 1 CPU hour to compute. On the other hand, a typical computation in Fig. 8 is rather expensive (because direct summation is used to evaluate the discretized elasticity, diffusion and normal velocity integrals). For example, the simulation shown in Fig. 8a takes approximately 90 CPU hours to compute. Most of this time is spent in solving the elasticity system, when $N \geq 2048$. Interestingly, the number of iterations required to solve the elasticity system is consistently *less* than that required to solve the diffusion system for the same error tolerance. This is somewhat surprising given the relative complexity of the elasticity system as compared to the diffusion system. This is an indication of the effectiveness of our preconditioning strategy for elasticity. In Fig. 8a from $t = 140 - 160$, for instance, the iteration count for elasticity is approximately 6–7 while for diffusion it is 9–10. The difference is more dramatic for 8d, where the elasticity count is typically 5–6 while for diffusion it is 11–12 (for $t = 1.0 - 2.0$). The reason the elasticity computation is so expensive is because four integral equations must be solved at each time step. Further, we consistently find that larger values of N are required to resolve the case with $Z \neq 0$ (presence of elastic fields) as compared to the case with $Z = 0$ (absence of elastic fields). We expect that employing a fast multipole method will reduce the time required to perform these computations by a factor of 30 when $N \geq 4096$ [12].

The homogeneous, anisotropic computation of Fig. 9 is much more efficient to compute as no integral equation needs to be solved to recover the elastic fields. The fields are evaluated directly from the quadrature of an integral [53]. This computation takes approximately 6 CPU hours to complete.

Case 2: *Two Precipitates of the Same Size*

The study of two growing or equilibrating precipitates is much more complicated than that of a single precipitate. The elastic fields generated by each particle interact with each other as well as with the composition field. This may result in alignment, translation, merging, and coarsening of precipitates. Coarsening is said to occur when one particle grows at the expense of the other. The primary feature of coarsening is that the total number of precipitates decreases rather uniformly in time as particles shrink in size and eventually vanish. This presents difficulties for boundary integral methods. We discuss this later, in Cases 3 and 4, where we consider particles of different sizes.

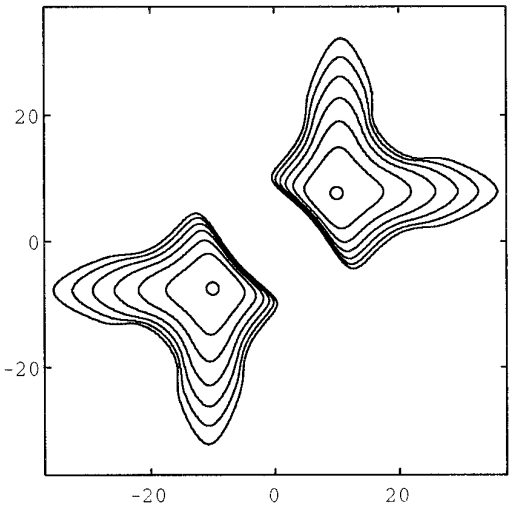

FIG. 10. Two soft ($\mu^P = 0.5$) precipitates growing from $t = 0$ to 36. The precipitates are initially unit circles with centers a distance $D = 25$ apart and the interfaces are plotted every 3 time units. Data used are: $\nu^P = \nu^M = 0.2$, $Z = 6000$, $J = 10$, $\varepsilon^0_{11} = -\varepsilon^0_{22} = 0.01$, $\varepsilon^0_{12} = 0$, $\Delta t = 0.001$, N ranges from 256 to 1024, tol $= 10^{-10}$, $\varepsilon = 10^{-11}$.

As a first step towards understanding the role elasticity plays in these complicated phenomena, we consider the simplest two-particle case. That is, we consider initially two precipitates with the same size, shape, and misfit. Symmetry considerations then require the particles to have the same size at all times. By studying this case first, we eliminate the potential for coarsening and we focus just on precipitate alignment, translation, and merging. One could correctly argue that considering equally sized particles is unphysical since in real alloys precipitates always have different sizes and coarsening is a very real phenomenon. However, the case of equally sized particles may be a good model for the late stages of coarsening where there are relatively few particles of approximately the same size and where particle alignment, translation, and merging are commonly observed.

(a) *Growth*. We begin this section by considering two growing precipitates. A typical example is shown in Fig. 10. There, two soft precipitates are grown under an applied shear and far-field flux. The precipitates are initially unit circles and the distance between their centers is $D = 25$. The growing precipitates are shown from $t = 0$ to $t = 18$ and are plotted every 3 time units. The parameters are $\mu^P = 0.5$, $\nu^M = \nu^P = 0.2$, $\varepsilon^0_{11} = -\varepsilon^0_{22} = 0.01$, $\varepsilon^0_{12} = 0$, $Z = 6000$, $J = 10$, tol $= 10^{-10}$, $\varepsilon = 10^{-11}$, and $\Delta t = 0.001$. Initially, $N = 256$ on each precipitate and N is gradually

increased to $N = 1024$ on each precipitate for $t \geq 7$. There is no misfit strain. We observe the same dendritic structure characteristic of single precipitate growth. The arms align in the directions of principal applied strain, except that the region between the particles is effectively shielded from the far-field flux and stays relatively flat. The shielding occurs because the far-field (global) mass flux is absorbed by the outermost boundaries before it is able to penetrate the inner region. In real alloys, growth is also driven by local mass fluxes so that even in the presence of a far-field flux, the regions between particles can still grow and form dendritic arms. From the theoretical and numerical point of view, it is difficult to simulate a local mass flux within a boundary integral model.

We further note that even though there are two growing precipitates, the number of iterations required to solve the elasticity integral equations (typically between 3–5) is still slightly less than that required to solve the diffusion system (typically between 5–7). This is in fact the generic behavior we observe for the elasticity/diffusion iteration counts in all our multiple precipitate computations. Finally, this computation takes approximately 10 CPU hours to complete on the Cray C90.

(b) *Equilibration.* In the absence of a far-field flux, our numerical simulations of two equally sized precipitates reveal a variety of different behaviors. Depending on the elastic parameters and the misfit strain, we observe particle translation, merging, repulsion, and significant shape variation. In the computations we present in this section, the initial precipitates are circular with the same radius. Note that such a configuration is an unstable equilibrium state in the absence of elastic effects ($Z = 0$).

We focus first on the effects of particle misfit strains rather than on the effects of applied strains as in the previous computations. Later, when we consider precipitates of different sizes, we will consider both misfit and applied strains. We remark that the computations in this section are performed slightly differently from those in the previous sections. First, the centroid positions, rather than the endpoints, are evolved to recover the (x_1, x_2) position from the $\theta - L$ form of the interface. Second, to prevent numerically induced coarsening, the area of each particle is conserved exactly by *choosing* the length L_i so that the area $A_i(t)$ at time t is equal to $A_i(0)$ for any given tangent angle $\theta_i(\alpha, t)$. Thus, we do not solve the ODE (2.73) for L_i. Instead, we use the following boundary integral formula for the area of the ith precipitate:

$$A_i(t) = \frac{L_i(t)}{4\pi} \int_0^{2\pi} (x_1(\alpha, t), x_2(\alpha, t)) \cdot n(\alpha, t)\, d\alpha. \tag{6.5}$$

Setting $A_i(t) = A_i(0)$ and using the $\theta - L$ form of the interface yields

$$L_i(t) = \frac{A_i(0)}{4\pi} \left\{ \int_0^{2\pi} \left[\sin(\theta_i(\alpha, t)) \int^{\alpha} \cos(\theta_i(\alpha', t)\, d\alpha' - \cos(\theta_i(\alpha, t)) \int^{\alpha} \sin(\theta_i(\alpha', t))\, d\alpha' \right] d\alpha \right\}^{-1}. \tag{6.6}$$

It is important to explicitly conserve area since numerically generated errors in the precipitate area can cause coarsening to occur at long times due to the underlying physical tendency of the system to coarsen. Of course, reducing the numerical parameters (particularly the time step Δt) reduces this difficulty but, on the other hand, increases the computational cost.

We begin by presenting the equilibration of soft precipitates each with the same dilatational (hydrostatic) misfit. The particles are initially unit circles aligned along the e_1-direction and the distance D between their centers is $D = 3$. The evolution from $t = 0$ to $t = 4.9$ is shown in Figs. 11a–f. The parameters are $\mu^{\mathrm{P}} = 0.5$, $\nu^{\mathrm{M}} = \nu^{\mathrm{P}} = 0.2$, $\varepsilon_{11}^{\mathrm{T}} = \varepsilon_{22}^{\mathrm{T}} = 0.01$, $\varepsilon_{12}^{\mathrm{T}} = 0$. Thus, the principal misfit strains have the same value. Further, $Z = 15000$, $J = 0$, tol $= 10^{-10}$, $\varepsilon = 10^{-11}$, and $\Delta t = 0.0002$. Initially, $N = 64$ on each interface and N is gradually increased to $N = 512$ for $t \geq 4.8$. We observe that the precipitates translate toward one another and we expect that they eventually merge. Interestingly, during the early stages of the evolution process, the distance D between the *centroids* of the precipitates actually *increases*, despite the fact that the *gap* between the precipitates always *decreases* in time. At later times, D decreases steadily. This nonuniform behavior of D can be explained by observing that the evolution is dominated by three main stages. At early times, the shapes of the precipitates change rapidly and the effect is to move the center of mass as described above. Once these initial shape changes occur, the equilibration then enters a translational stage where the particle centroids move toward each other. Finally, the precipitates enter a merger stage where they eventually coalesce to become one. These three different evolution stages can be seen very clearly by looking at plots of the energy. In Figs. 12a, c, and e, we give the total energy W_{tot}, the surface energy W_Γ, and the elastic energy ZW_{el} (see Section 2.3) as a function of time for the computation shown in Fig. 11. The plots 12b, d, and f correspond to the hard precipitate case which we discuss presently. Consider first the total energy in Fig. 12a. For $t < 0.2$, there is a rapid decrease in energy. This is associated with the rapid shape change at early times. For $0.2 < t < 4$, there is a much slower energy decrease. This is associated with the translational stage of the evolution. For $4 < t < 4.9$, there is again a rapid decrease in energy. This is associated with merger. Note that the surface energy in Fig. 12c *increases* during the entire evolution. Consequently, it is the decrease in elastic energy (Fig. 12e) that drives the

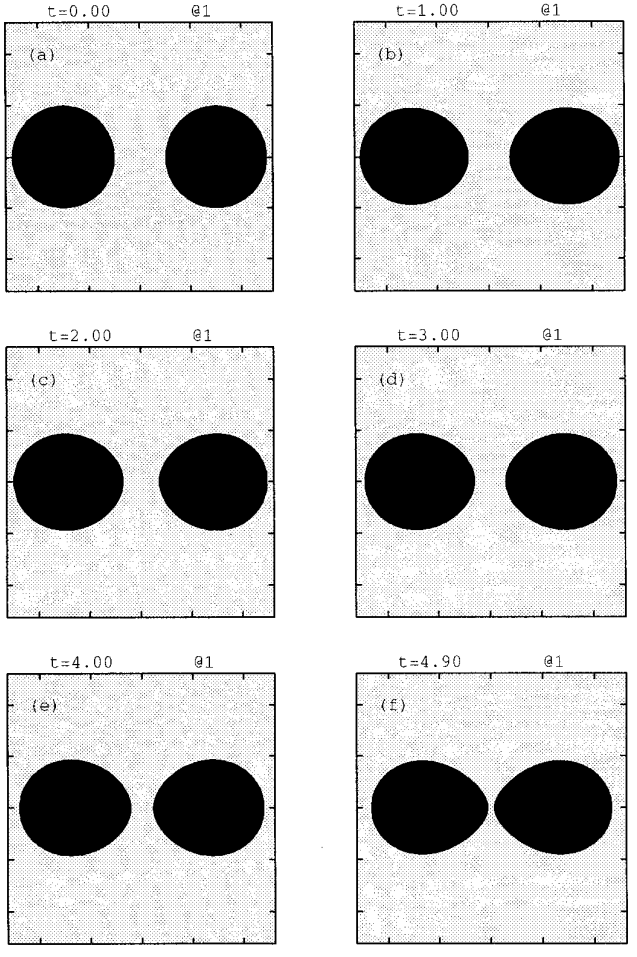

FIG. 11. The equilibration ($J = 0$) of two soft ($\mu^P = 0.5$) precipitates with dilatational misfits. Initially, both particles are unit circles and their centers are distance $D = 3$ apart. Data used are: $\nu^P = \nu^M = 0.2$, $Z = 15000$, $\varepsilon_{11}^T = \varepsilon_{22}^T = 0.01$, $\varepsilon_{12}^T = 0$, for both precipitates. The tick marks are 1 unit apart. $\Delta t = 0.0002$, N ranges from 64 to 512, tol $= 10^{-10}$, and $\varepsilon = 10^{-11}$.

process. Clearly, this computation indicates that morphological changes are an important part of equilibration. As such, it casts doubt on studies where particle shapes are constrained. We note that the above computation takes approximately 4 CPU hours to complete on the Cray C90.

Now, consider the effect of the elastic inhomogeneity. We repeat the preceding simulation using two *hard* precipitates instead of two soft ones. We take $\mu^P = 2$ and $\Delta t = 0.002$. It is sufficient to use $N = 64$ on each interface and all other parameters are fixed as before. The resulting evolution from $t = 0$ to $t = 40$ is shown in Figs. 13a–f. In contrast to the soft case, the hard precipitates tend to repel each other. However, we observe that at very early times D *decreases*, even though the gap width between the precipitates steadily *increases*. At later times D increases steadily. Here, the nonuniformity of D in time is due to the fact that the evolution occurs in two distinct stages. At early times, there are rapid shape changes and at moderate to late times the precipitates repel each other. As before, this is best seen by analyzing the energy. In Figs. 12b, d, f (for a blowup of early times) and 14a–c (for times up to $t = 40$), the total energy, surface energy, and elastic energy are plotted. At early times, there is a sharp drop in the total energy associated with the rapid shape change. Note that at these early times, the surface energy increases although by quite a small amount (note the reduced scale on the graph). Nevertheless, this stage is driven by elastic effects. At later times, there is a much more gradual decrease in the energy associated with the translational stage. At these times, the surface energy decreases and the precipitates become circular as they move apart. In Fig. 12, the energies for the soft and hard cases can be directly compared, up to time $t = 4.9$. Note that by making the precipitate hard, the elastic energy increases by about a factor of two. This is reflected in the total energy. Further, except for the initial shape change stage ($0 \le t < 0.2$) the energies in the hard precipitate case vary much more slowly than those in the soft case.

Finally, since $N = 64$ this computation takes only one-fourth of a CPU hour to complete on the Cray C90.

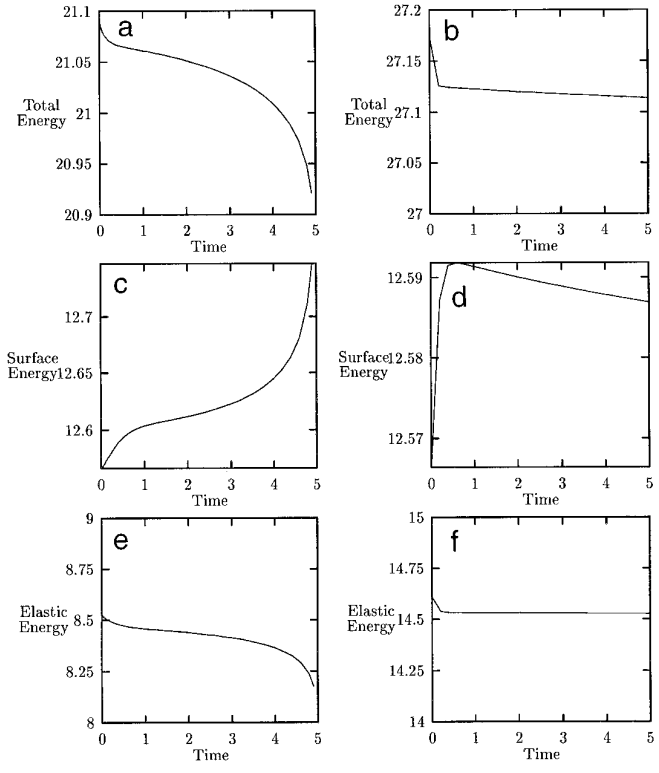

FIG. 12. In (a), (c), (e) the total, surface, and elastic energies are shown for the calculation in Fig. 11. In (b), (d), (f) the energies are shown for the calculation in Fig. 13 up to time $t = 4.9$.

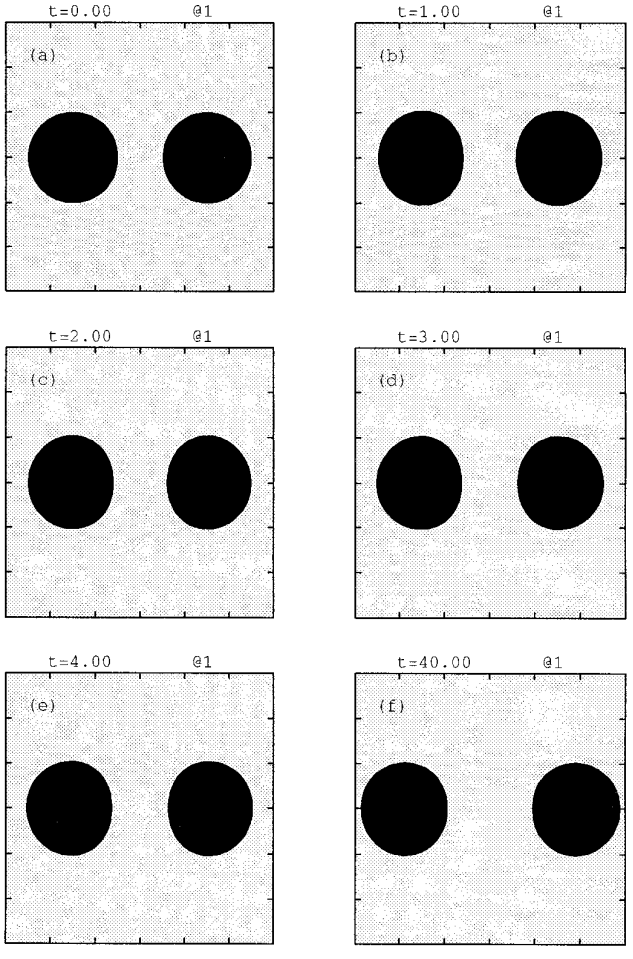

FIG. 13. The equilibration ($J = 0$) of two hard ($\mu^P = 2$) precipitates with dilatational misfits. Initially, both particles are unit circles and their centers are distance $D = 3$ apart. The tick marks are 1 unit apart. Data used are: $\nu^P = \nu^M = 0.2$, $Z = 15000$, $\varepsilon^T_{11} = \varepsilon^T_{22} = 0.01$, $\varepsilon^T_{12} = 0$, for both precipitates. $\Delta t = 0.002$, $N = 64$, tol $= 10^{-10}$, and $\varepsilon = 10^{-11}$.

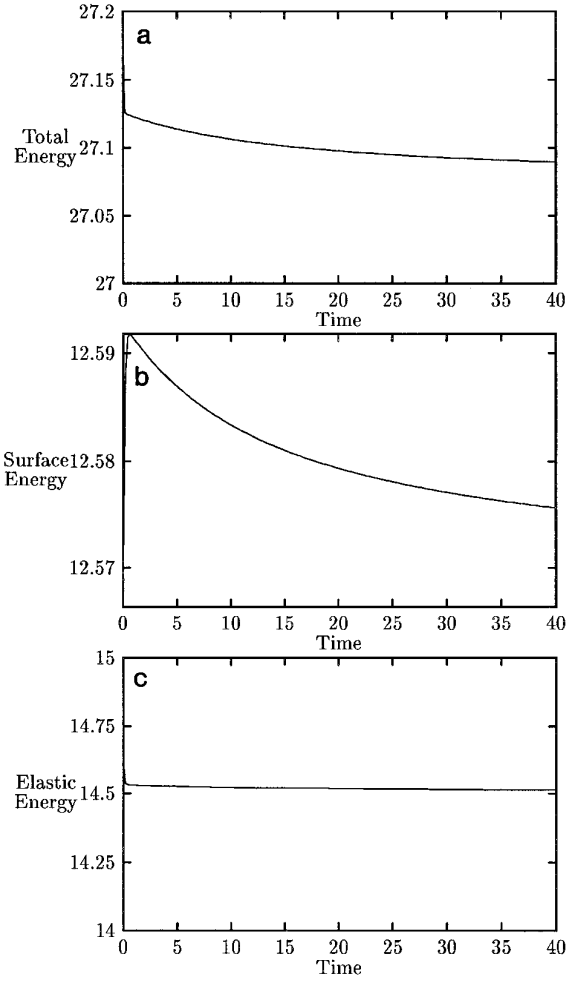

FIG. 14. The total, surface, and elastic energies for the calculation in Fig. 13.

We next consider misfit strains where the principal strains have different values, thereby introducing directional dependence. We begin by considering the simplest scenario. We take $\varepsilon^T_{12} = 0$ and only one of ε^T_{11} or ε^T_{22} to be nonzero, i.e., a uniaxial misfit. Four such computations are shown in Figs. 15a, b and 16a, b. In Fig. 15, the evolution of two soft precipitates, with $\mu^P = 0.5$, is shown. In Fig. 16, the evolution of two hard precipitates, with $\mu^P = 2$, is shown. In both figures, the particles are initially unit circles and are aligned along the e_1-direction with $D = 3$. In the graphs marked (a), both precipitates have misfit strain $\varepsilon^T_{22} = 0.01$, while in those marked (b), both precipitates have misfit strain $\varepsilon^T_{11} = 0.01$. In both figures, $\Delta t = 0.0025$. In Figs. 15a and 16a, $N = 128$ initially and is gradually increased to $N = 512$ for $t \geq 2.0$ (in Fig. 15a) and for $t \geq 0.7$ (in Fig. 16a). In Figs. 15b and 16b, $N = 128$ throughout the computations. The other parameters are $Z = 12000$, tol $= 10^{-10}$, $\varepsilon = 10^{-11}$, and $J = 0$.

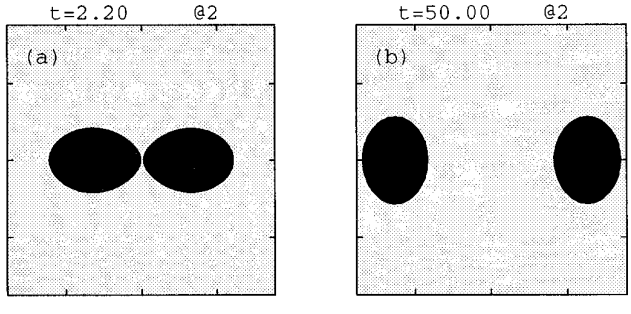

FIG. 15. Equilibrated ($J = 0$) configurations for two soft ($\mu^P = 0.5$) precipitates with uniaxial misfits. The precipitates are initially unit circles with $D = 3$. The tick marks are 2 units apart. In (a) both precipitates have misfit strain $\varepsilon^T_{11} = 0 = \varepsilon^T_{12}$ and $\varepsilon^T_{22} = 0.01$. In (b), $\varepsilon^T_{11} = 0.01$ and $\varepsilon^T_{12} = \varepsilon^T_{22} = 0$. Data used are: $\nu^P = \nu^M = 0.2$, $Z = 12000$, $\Delta t = 0.0025$, N ranges from 128 to 512, tol $= 10^{-10}$, and $\varepsilon = 10^{-11}$.

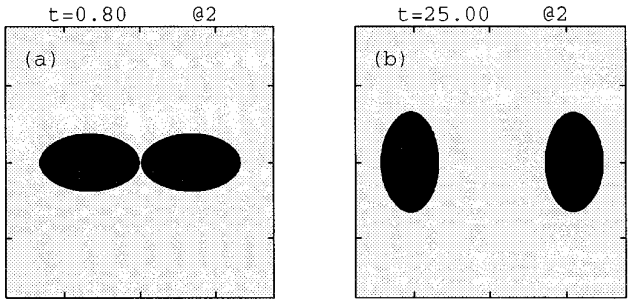

FIG. 16. Equilibrated ($J = 0$) configurations for two hard ($\mu^P = 2$) precipitates with uniaxial misfits. The precipitates are initially unit circles with $D = 3$. The tick marks are 2 units apart. In (a) both precipitates have misfit strain $\varepsilon_{11}^T = 0 = \varepsilon_{12}^T$ and $\varepsilon_{22}^T = 0.01$. In (b), $\varepsilon_{11}^T = 0.01$ and $\varepsilon_{12}^T = \varepsilon_{22}^T = 0$. Data used are: $\nu^P = \nu^M = 0.2$, $Z = 12000$, $\Delta t = 0.0025$, N ranges from 128 to 512, tol $= 10^{-10}$, and $\varepsilon = 10^{-11}$.

We observe that independent of whether the precipitates are hard or soft, the precipitates always become elliptical with the long axis perpendicular to the direction of nonzero principal misfit strain. Furthermore, the precipitates attract and appear to merge when the direction of principal misfit strain is perpendicular to the direction of particle alignment (Figs. 15a and 16a). Analogously, the precipitates repel when the direction of nonzero principal misfit strain is parallel to that of the alignment (Figs. 15b and 16b). Recall that, in contrast, dilatational misfits result in attraction for soft particles and repulsion for hard particles. Thus, we expect complicated interactions between inhomogeneity and misfit when we consider more general misfits. We present one computation with a more general misfit strain to show such behavior. Additional simulations will be given in a future work [25].

We consider two hard precipitates ($\mu^P = 2$). Initially, the precipitates are unit circles oriented at 45° to the e_1-direction with $D = 3.39$. Both particles have misfit strain $\varepsilon_{11}^T = 0.01$, $\varepsilon_{22}^T = 0.02$, and $\varepsilon_{22}^T = 0$. Thus, the direction of maximum principal misfit strain is the e_2-direction. Also, $\Delta t = 0.0005$ and $Z = 6000$. Initially, $N = 128$ and is increased to $N = 256$ for $t \geq 17.5$.

The initial ($t = 0$) and final ($t = 18$) times of our simulation are shown in Fig. 17. The centroid positions are also displayed on the figure. The initial positions of the centroids are indicated by the hollow circles and the solid circles mark their final positions. The curves connecting the circles trace their evolution paths. We observe that the precipitates translate so that they eventually align along the e_1-direction which is perpendicular to the direction of maximum principal misfit strain. Similar alignment has been seen in the calculations of Su and Voorhees for elastically anisotropic, homogeneous systems [47, 48]. In our simulation, the precipitates become somewhat elliptical and the gap between them, as well as the distance between their centroids, decreases. However, the sides of closest approach become flat as if the precipitates want to avoid merging. This is unlike the situation in Fig. 16a, where the sides of closest approach curve toward each other, enhancing merger. This results from the competing elastic effects in this simulation. We can decompose the misfit strain into the sum of a dilatational strain and a uniaxial strain. Since the uniaxial direction (e_2-direction) is perpendicular to the direction of eventual particle alignment, this favors elliptical shapes and merger (recall Fig. 16a). However, because the precipitates are hard, the dilatational strain favors repulsion. It is the repulsive effect that causes the sides of closest approach to be flat. The final morphology reflects this competition.

The computations in Figs. 15 and 16 each take less than 1 CPU hour to compute on the Cray C90, while the computation in Fig. 17 takes approximately 6 CPU hours to complete.

Case 3: *Two Precipitates of Different Sizes*

We now consider equilibrating precipitates of different sizes. In the *absence* of elastic effects, the diffusional evolution is such that large particles grow monotonically in time. Since total area is conserved, small precipitates are thus forced to shrink and then vanish at finite times. This leads to a ''survival of the fattest'' [43] as eventually only one large precipitate remains. This is the configuration that minimizes the surface energy corresponding to a given area and is referred to as ''classical'' coarsening or Ostwald ripening [52]. From an engineering point of view, classical coarsening is undesirable because the resultant decrease in number density of precipitates in a coarsening alloy

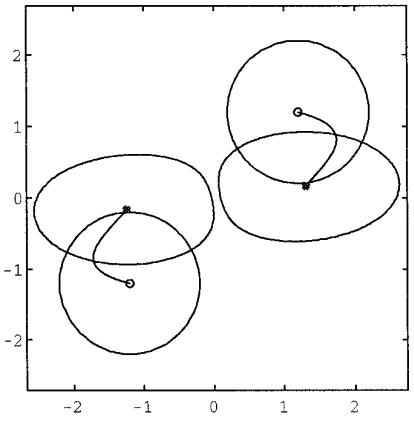

FIG. 17. Two hard ($\mu^P = 2$) precipitates aligning during equilibration ($J = 0$). The initial precipitates are unit circles with $D = 3.39$ oriented at 45° to the e_1 direction. The initial and final shapes ($t = 18$) are shown, along with the positions of the centroids. Data used are: $\nu^P = \nu^M = 0.2$, $Z = 6000$, $\varepsilon_{11}^T = 0.01$, $\varepsilon_{22}^T = 0.02$, $\varepsilon_{12}^T = 0$ for both precipitates, $\Delta t = 0.0005$, N ranges from 128 to 256, tol $= 10^{-10}$, and $\varepsilon = 10^{-11}$.

can lead to a failure of the alloy. One of the outstanding problems in material science is to understand how to stabilize such equilibrating systems against a severe decrease in number density of precipitates. Elastic effects could provide such a stabilizing mechanism. Theoretically, this is possible because elastically influenced coarsening may not favor the largest precipitate. Ideally, one would like to find situations where a microstructure consisting of many nearly equally sized particles is energetically favorable over a microstructure consisting of one or a few large particles.

As a first step to analyze elastically influenced coarsening, we consider the case of two equilibrating precipitates of different sizes. In the presence of constant (in time) misfit or applied fields, our results indicate that only one particle survives the coarsening process. However, because of elastic effects, small particles can be induced to grow and large particles can be forced to shrink. We can find cases where the areas of individual precipitates evolve nonmonotonically in time. In fact at short times, stabilization may be achieved so that equally sized particles are favored. At long times, there is typically no elastic stabilization because the area evolution eventually becomes monotonic and one particle dominates. On the other hand, by using the applied strains as a control variable in time, it may be possible to achieve a dynamic stabilization of the coarsening process. The elastic inhomogeneity plays an important role in the details of the above processes. Some of these phenomena are illustrated below. Additional results will be given in a future work [25].

The computations in this section are performed with the area $A_i(t)$ as a dynamic variable rather than the length $L_i(t)$ of each interface. Using the formula for the time derivative of the area,

$$\dot{A}_i = \frac{L_i(t)}{2\pi} \int_0^{2\pi} V_i(\alpha, t)\, d\alpha, \tag{6.7}$$

we evolve the area in time using the second-order Adams–Bashforth discretization

$$A_i^{n+1} = A_i^n + \frac{\Delta t}{2}(3\dot{A}_i^n - \dot{A}_i^{n-1}), \tag{6.8}$$

where

$$\dot{A}_i^n = \frac{L_i^n}{2\pi} \int_0^{2\pi} V_i^n(\alpha)\, d\alpha. \tag{6.9}$$

The updated length L_i^{n+1} is obtained from A_i^{n+1} by using Eq. (6.6) with $A_i(0)$ replaced by A_i^{n+1}. The centroid is also used as a dynamic variable.

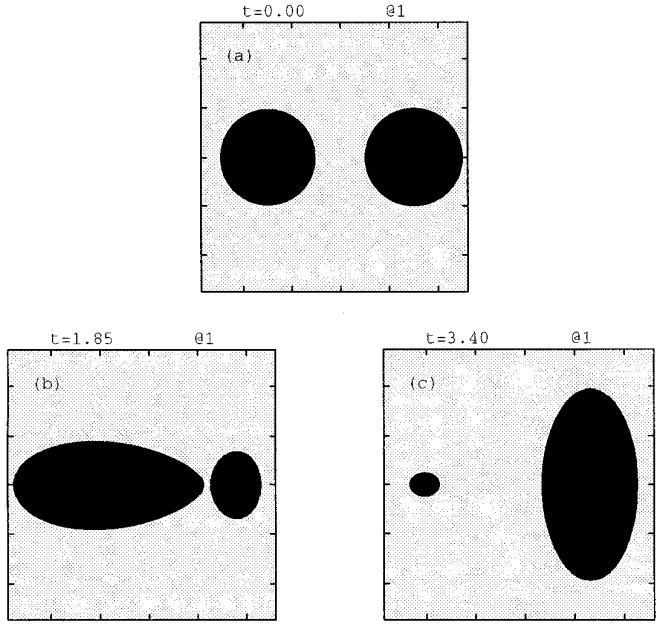

FIG. 18. Two precipitates undergoing coarsening. The left particle is initially circular with radius $R_l = 0.98$ and has misfit strain $\varepsilon_{11}^{\mathrm{T}} = 0.01$, $\varepsilon_{22}^{\mathrm{T}} = 0.02$, and $\varepsilon_{12}^{\mathrm{T}} = 0$. The right particle is initially circular with radius $R_r = 1.0$ and has misfit strain $\varepsilon_{11}^{\mathrm{T}} = 0.02$, $\varepsilon_{22}^{\mathrm{T}} = 0.01$, and $\varepsilon_{12}^{\mathrm{T}} = 0$. The initial interparticle distance is $D = 3$. The tick marks are 1 unit apart. The initial configuration is shown in (a). In (b), both precipitates are soft ($\mu^{\mathrm{P}} = 0.5$). In (c), both precipitates are hard ($\mu^{\mathrm{P}} = 2$). Data used are: $\nu^{\mathrm{P}} = \nu^{\mathrm{M}} = 0.2$, $Z = 6000$, $J = 0$, $\Delta t = 0.00125$, $N = 512$, tol $= 10^{-10}$, and $\varepsilon = 10^{-11}$.

As a first example, in Fig. 18 we present two equilibrating initially circular precipitates with radii $R_l = 0.98$ for the left precipitate and $R_r = 1$ for the right. Both particles have misfit strains. The left precipitate has misfit strain $\varepsilon_{11}^{\mathrm{T}} = 0.01$ $\varepsilon_{22}^{\mathrm{T}} = 0.02$, $\varepsilon_{12}^{\mathrm{T}} = 0$ so that e_2 is the direction of the largest principal strain while the right has $\varepsilon_{11}^{\mathrm{T}} = 0.02$, $\varepsilon_{22}^{\mathrm{T}} = 0.01$, $\varepsilon_{12}^{\mathrm{T}} = 0$ and so has e_1 as the direction of largest principal strain. The precipitates are initially aligned along the e_1-direction and the distance between their centers is $D = 3$. Also $\nu^{\mathrm{M}} = \nu^{\mathrm{P}} = 0.2$, $Z = 6000$, $J = 0$, $N = 512$, $\Delta t = 0.00125$, tol $= 10^{-10}$, and $\varepsilon = 10^{-11}$. The initial precipitate configuration is shown in Fig. 18a. In 18b, the result of two coarsening *soft* precipitates with $\mu^{\mathrm{P}} = 0.5$ is shown at $t = 1.85$. In 18c, the result of two coarsening *hard* precipitates with $\mu^{\mathrm{P}} = 2$ is shown at $t = 3.40$.

If the precipitates are soft the left precipitate dominates the coarsening process. If the precipitates are hard the right precipitate dominates. This shows that elastic inhomogeneity can play a significant role in the coarsening process.

In the soft precipitate case, the area evolution of each precipitate is monotonic in time. The area evolution is shown in Figs. 19a and b. At approximately $t = 0.15$, the precipitates momentarily have the same area. As this does

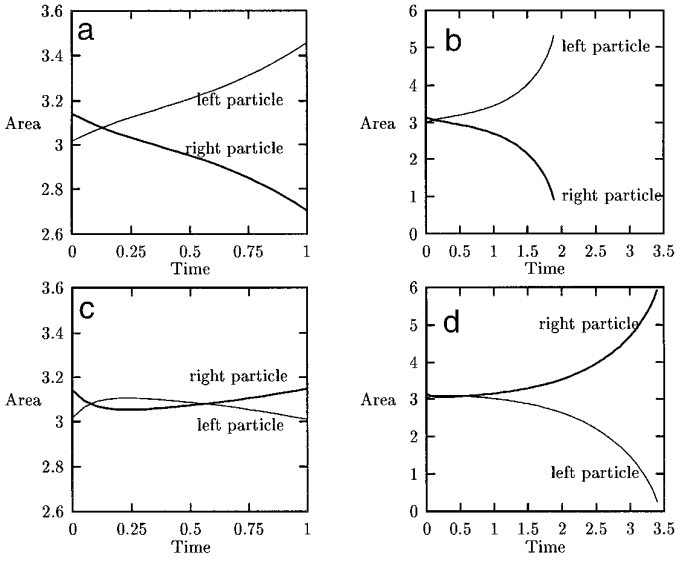

FIG. 19. The area evolution of each precipitate corresponding to the calculation in Fig. 18. The soft precipitate case is shown in (a) and (b) and the hard case is shown in (c) and (d).

not correspond to an equilibrium configuration, the areas continue to evolve. However, as seen in Fig. 18b, the left precipitate takes an ''egg-shaped'' form with the side closest to the right precipitate being more curved. It appears that the precipitates will merge before the right precipitate entirely vanishes. Since the precipitate that was initially the smaller of the two is the one that dominates the late stages of the coarsening process, we refer to this as ''inverse'' coarsening. This is in contrast to classical coarsening where large precipitates *always* grow.

For the hard precipitate case shown in Fig. 18c it is the initially larger right precipitate that dominates the late stages and it appears that the left particle will vanish entirely. One is tempted to call this case classical but an inspection of the evolution of the precipitate areas reveals clear nonclassical behavior. This is shown in Figs. 19c and d. The area evolution is nonmonotone and there are two times, approximately $t = 0.1$ and $t = 0.5$, where the areas of both precipitates are equal. Since these do not correspond to equilibrium configurations, the areas continue to evolve until the initially larger (right) particle devours the other. Surprisingly, for the times $t \leq 0.5$, elastic stabilization is achieved. At later times $t > 0.5$, however, the area evolution becomes monotonic and the right precipitate dominates. This ''oscillatory'' behavior is sensitive to the initial sizes of the particles, the relative shear moduli, and the magnitude of the surface energy compared to the elastic energy. Moreover, this oscillatory behavior is not always observed in the hard particle case. So far, we have found no way to predict *a priori* whether this oscillatory behavior will occur. Finally, note that as the left precipitate decreases in size it also becomes more circular. This is because for small precipitates surface energy dominates the elastic energy, since the surface energy scales like the length of a precipitate interface, while elastic energy scales like the area of a precipitate region.

We now show how the application of applied strains may alter the coarsening process. Consider the same hard precipitate system as in Fig. 18c. We add a small, relative to the misfit, applied uniaxial strain in the e_2-direction, i.e., $\varepsilon^0_{22} = 0.001$ and $\varepsilon^0_{11} = \varepsilon^0_{12} = 0$. All other parameters are held fixed. The applied strain favors the left precipitate since the largest misfit strain of that precipitate also has e_2 as its direction. The results at $t = 0$ and $t = 2.05$ are shown in Figs. 20a and b, respectively. We see that now the left particle dominates the coarsening process. Further, in Figs. 20c and d, we see that the precipitate areas evolve monotonically. Recall that without the applied field, the right particle dominated, the area evolution was nonmonotone, and there was an elastic stabilization at early times. Thus, although the applied field stabilizes the left precipitate, there is no overall elastic stabilization as the precipitate areas evolve monotonically. We note that an analogous effect can be achieved in the *soft* precipitate case of Fig. 18b. There, the right particle can be stabilized by applying a uniaxial strain in the e_1 direction.

The above results suggest that, by varying the applied fields in time, it may be possible to stabilize the coarsening process against a decrease in number density of precipi-

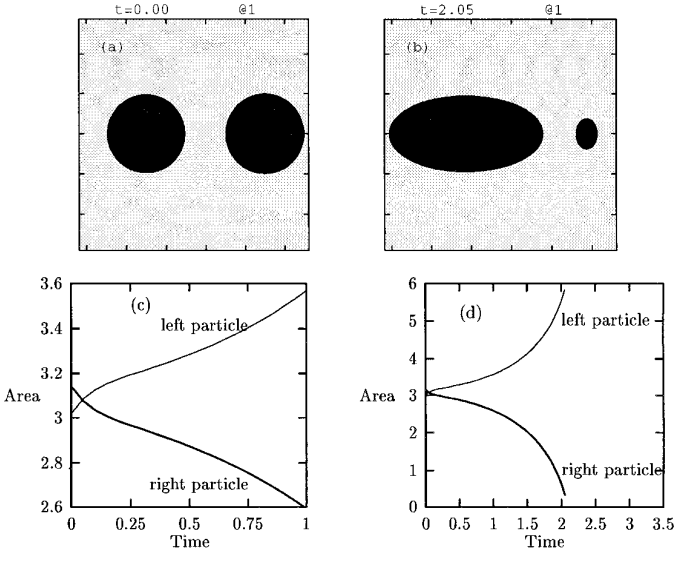

FIG. 20. Coarsening of two precipitates with both misfit and applied strains. The parameters are as in Fig. 18c, except that there is an additional applied strain $\varepsilon^0_{11} = \varepsilon^0_{12} = 0$ and $\varepsilon^0_{22} = 0.001$. In (a), the initial configuration is shown. In (b), the final configuration at $t = 2.05$ is shown. In both (a) and (b), the tick marks are 1 unit apart. In (c), the early time evolution of the precipitate areas is shown. In (d), the entire time evolution of the areas is shown.

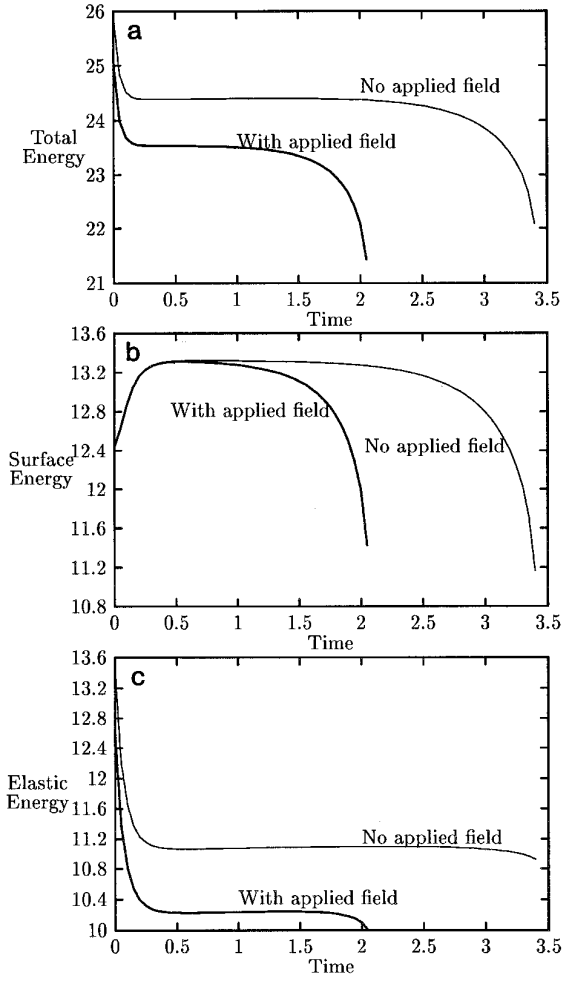

FIG. 21. The total, surface, and elastic energies are shown for the coarsening of two hard precipitates with (Fig. 20) and without (Fig. 18c) applied fields.

tates. It certainly seems possible to do so in this simple two-particle system. However, when the system consists of many coarsening precipitates, the answer is not so clear. We do not address the question of using time-varying applied fields to achieve elastic stabilization in this paper. The potential for such stabilization will be discussed in a future work [25].

A natural question about the computations in Figs. 18 and 19 is whether the differences in the coarsening behavior are reflected in the system energies. In Figs. 21a–c, we give the total, surface, and elastic energies for the hard precipitate case, both with and without the applied field. The shapes of the energy curves with and without the applied fields are very similar, suggesting that the energies are insensitive to the details of the coarsening process. We have also examined the energies and their time rates of change for the individual particles; they also seem to be insensitive to the details of the process.

Finally, these coarsening computations of two differently sized particles all take approximately 5 CPU hours on the Cray C90.

Case 4: *Multiple Precipitates*

As a final example, we present the equilibration of a system of many differently sized, arbitrarily placed precipitates. The precipitates are soft and the parameters are $\mu^{\mathrm{P}} = 0.5$, $\nu^{\mathrm{M}} = \nu^{\mathrm{P}} = 0.2$, $Z = 6000$, $N = 512$ on each precipitate interface, $\Delta t = 0.0025$, tol $= 10^{-10}$, and $\varepsilon = 10^{-11}$. The precipitate misfits are either $\varepsilon^{\mathrm{T}}_{11} = 0.01$, $\varepsilon^{\mathrm{T}}_{22} = 0.015$, or $\varepsilon^{\mathrm{T}}_{11} = 0.015$, $\varepsilon^{\mathrm{T}}_{22} = 0.01$. In all cases, $\varepsilon^{\mathrm{T}}_{12} = 0$. There is no applied strain. The evolution of the system until t = 9.8 is shown in Fig. 22. We simulate precipitate van-

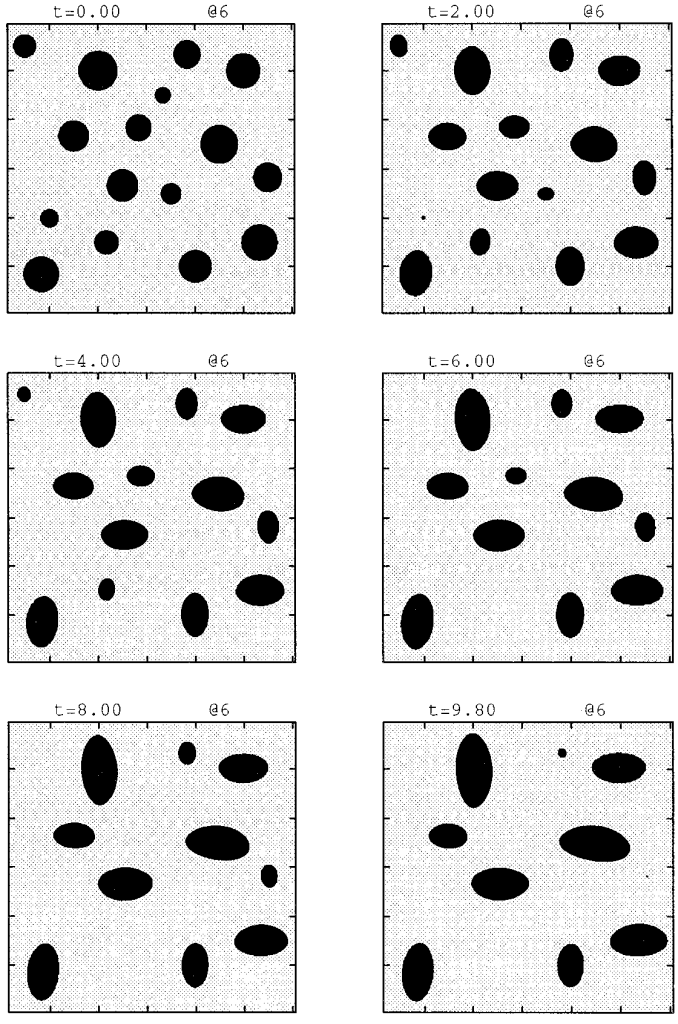

FIG. 22. Coarsening of 16 particles with random positions and sizes and different misfits. Precipitates are removed when their area drops below 0.1. The tick marks are 6 units apart. For all particles, $\mu^{\mathrm{P}} = 0.5$, $\nu^{\mathrm{M}} = \nu^{\mathrm{P}} = 0.2$, $Z = 6000$, $N = 512$, $\Delta t = 0.0025$, tol $= 10^{-10}$, $\varepsilon = 10^{-11}$. The misfits are either $\varepsilon^{\mathrm{T}}_{11} = 0.015$, $\varepsilon^{\mathrm{T}}_{22} = 0.01$, $\varepsilon^{\mathrm{T}}_{12} = 0$, or $\varepsilon^{\mathrm{T}}_{11} = 0.01$, $\varepsilon^{\mathrm{T}}_{22} = 0.015$, $\varepsilon^{\mathrm{T}}_{12} = 0$.

ishing by removing precipitates when their area drops below 0.1. The effect of this procedure is discussed below.

As we saw in the previous computations, the precipitates develop roughly elliptical shapes, depending on the direction of their largest principal misfit strain. Further, we observe an overall classical coarsening behavior as large precipitates grow at the expense of smaller ones. Further, no significant precipitate translation or alignment occurs. In addition, no merging is observed.

Although boundary integral methods do not easily handle changes in topology, one can easily remove precipitates "by hand" when they become very small. Precipitate merging, on the contrary, is much more difficult to handle. Since our precipitates vanish before merging is seen, we focus here on their removal. It is well known that through the usual Gibbs–Thomson boundary condition, small precipitates have an unphysically large effect on the evolution of a multiparticle system [51]. As we show here, elastic effects could make their contribution even larger. This is seen by considering the energy of the system. From Section 2.3, the total finite part of the energy is given by

$$W_{\text{tot}}(t) = W_\Gamma + ZW_{\text{el}}. \tag{6.10}$$

W_Γ scales like $\sum_j L_j$ and W_{el} scales like $\sum_j L_j^2$. Suppose now that the ith precipitate becomes very small and vanishes at time $t = t_c$. Clearly, the energy varies continuously through $t = t_c$. The time derivative of the energy, $\dot{W}_{\text{tot}}$, on the other hand, does not vary smoothly through $t = t_c$. This is seen as follows. From Section 2.3, the time derivative of the energy is given by

$$\dot{W}_{\text{tot}}(t) = \sum_j \int_{\Gamma_j} (\kappa_j(s,t) + ZG_j^{\text{el}}(s,t))V_j(s,t)\, ds. \tag{6.11}$$

As the ith particle becomes very small, it typically becomes circular. This implies that

$$\kappa_i(s,t) \sim \frac{2\pi}{L_i(t)}, \quad V_i(s,t) \sim \dot{L}_i(t) \tag{6.12}$$

for t near t_c. Also G_i^{el} is independent of L_i. Using (6.12) in Eq. (6.11) gives

$$\begin{aligned}\dot{W}_{\text{tot}}(t) \sim \dot{L}_i(t) &\left[2\pi + Z\frac{L_i(t)}{2\pi}\int_0^{2\pi} G_i^{\text{el}}(\alpha,t)\, d\alpha\right] \\ &+ \sum_{j\neq i}\int_{\Gamma_j} (\kappa_j(s,t) + ZG_j^{\text{el}}(s,t))V_j(s,t)\, ds.\end{aligned} \tag{6.13}$$

Thus, the contribution to $\dot{W}_{\text{tot}}$ from the ith precipitate is not necessarily small as the length L_i scales out of the surface energy contribution. Note that the elastic energy contribution scales like L_i. The fact that L_i scales out of the surface energy means that removing the ith precipitate necessarily causes a jump in $\dot{W}_{\text{tot}}(t)$. Moreover, this jump could be quite large and depends on the behavior of $\dot{L}_i(t)$ as $t \to t_c$. The scaling of L_i with $t_c - t$ in classical coarsening without elastic effects gives $L_i(t) \sim (t_c - t)^{1/3}$ and so $\dot{L}_i(t) \sim -(t_c - t)^{-2/3}$. We expect that this scaling still holds in the presence of elastic effects since the surface energy is dominant for small enough precipitates. We will investigate this hypothesis in a future work [25]. Using these scalings in Eq. (6.13) gives

$$\begin{aligned}\dot{W}_{\text{tot}}(t) \sim -(t_c - t)^{-2/3} &\left[2\pi + Z(t_c - t)^{1/3}\int_0^{2\pi} G_i^{\text{el}}(\alpha,t)\, d\alpha\right] \\ &+ \sum_{j\neq i}\int_{\Gamma_j} (\kappa_j(s,t) + ZG_j^{\text{el}}(s,t))V_j(s,t)\, ds.\end{aligned} \tag{6.14}$$

Thus, the contribution from the surface energy of the ith precipitate blows up like $-(t_c - t)^{-2/3}$ as $t \to t_c$. The contribution from the elastic energy blows up as well, albeit at the less singular rate $-(t_c - t)^{-1/3}$, assuming that $\int_0^{2\pi} G_i^{\text{el}}(\alpha, t)\, d\alpha$ is bounded as $t \to t_c$. This shows that with the above assumptions and with Z fixed in time, the *evolution* of the system, as defined through $\dot{W}_{\text{tot}}$, cannot be smoothly continued through $t = t_c$.[3] We note that the nonsmoothness of $\dot{W}_{\text{tot}}$ as $t \to t_c$ is not restricted to two dimensions. In three dimensions, similar arguments show the surface energy contribution is $O(-(t_c - t)^{-1/3})$ and the elastic energy contribution is $O(1)$.

An investigation of the energy evolution for our 16 precipitate computation clearly shows the behavior described above. In Figs. 23a and b, the elastic and surface energies, respectively, are shown. The filled circles correspond to the times immediately *after* a precipitate is removed. As expected, the elastic energy appears to be smooth and the surface energy is kinked. The small discontinuities observed in the surface energy (and hidden in the plot of the elastic energy) are due to the fact that small but finite sized precipitates are removed. The total energy is shown in Fig. 24a and shows a similar behavior. The time derivative $\dot{W}_{\text{tot}}$ is shown in Fig. 24b. We do not use filled circles in this plot so that the discontinuities associated with precipitate vanishing can be clearly observed. Note that as expected, $\dot{W}_{\text{tot}}$ drops sharply just before a precipitate vanishes (is removed). Because precipitates are removed after their area drops below 0.1, their size when they are actually removed varies. Thus, the drops in $\dot{W}_{\text{tot}}$ vary. Interestingly,

[3] On the other hand, if one were able to introduce a surface tension τ (through a different nondimensionalization) and τ and Z were allowed to vanish as $t \to t_c$, then it may be possible to obtain a smooth evolution. We are currently experimenting with this approach.

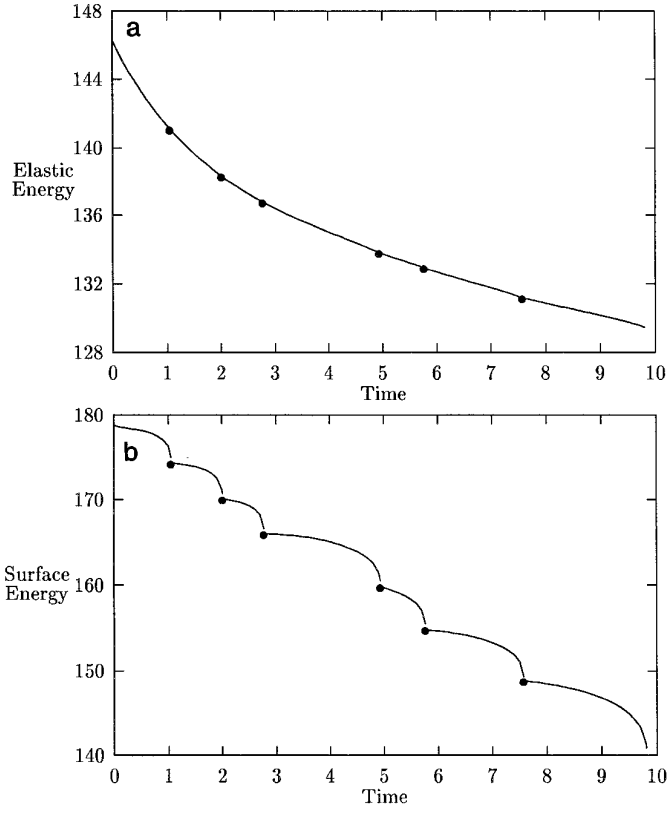

FIG. 23. The elastic and surface energies for the 16-particle computation shown in Fig. 22. The filled circles correspond to times immediately after a precipitate is removed.

after a precipitate is removed, $\dot{W}_{\text{tot}}$ recovers so that the envelope of the curve appears continuous.

Finally, the 16 precipitate computation takes 15 CPU hours on the Cray C90.

7. CONCLUSIONS

In this paper, an efficient and spectrally accurate numerical method based on boundary integrals has been developed to study the evolution of multiphase microstructure in elastically stressed alloys. The method is based on solving diffusion and elasticity integral equations and tracking the positions of the precipitate–matrix interfaces. The elasticity and diffusion problems are coupled through a generalized Gibbs–Thomson condition. The precipitate and matrix phases are isotropic and linear elastic. The precipitate and matrix may have different elastic constants. Both misfit strains and applied fields are considered.

To solve the integral equations for diffusion, we use the approach of Greenbaum, Greengard, and McFadden [11], which removes the ill-conditioning associated with multiple particles. The integral equations for elasticity are much more difficult to solve. To solve them, we develop a new preconditioning technique based on small-scale decomposition of the elasticity integral equations. This decomposition explicitly removes the ill-conditioning of the discretized linear system and greatly reduces the number of iterations required to find a solution (using GMRES). To update the interface positions, we use the approach of Hou, Lowengrub, and Shelley [17], which removes the stiffness associated with tracking an interface with surface energy [11]. Thus, we are able to track the motion of many precipitate–matrix interfaces.

Simulations of a single precipitate indicate that growing and equilibrating precipitates have vastly different shapes. Growth shapes are dendritic and equilibrated shapes are squarish. This agrees qualitatively with recent experiments on nickel-based alloys. Simulations of multiparticle systems show that complicated interactions involving elastic inhomogeneities, misfit strains, and applied fields occur. For example, alignment, translation, merging, and coarsening of precipitates is seen.

The shapes we observe in both the single and multiparticle simulations are qualitatively similar to those calculated in elastically anisotropic, homogeneous systems. However, we find that inhomogeneity can play a crucial role in the details of the evolution.

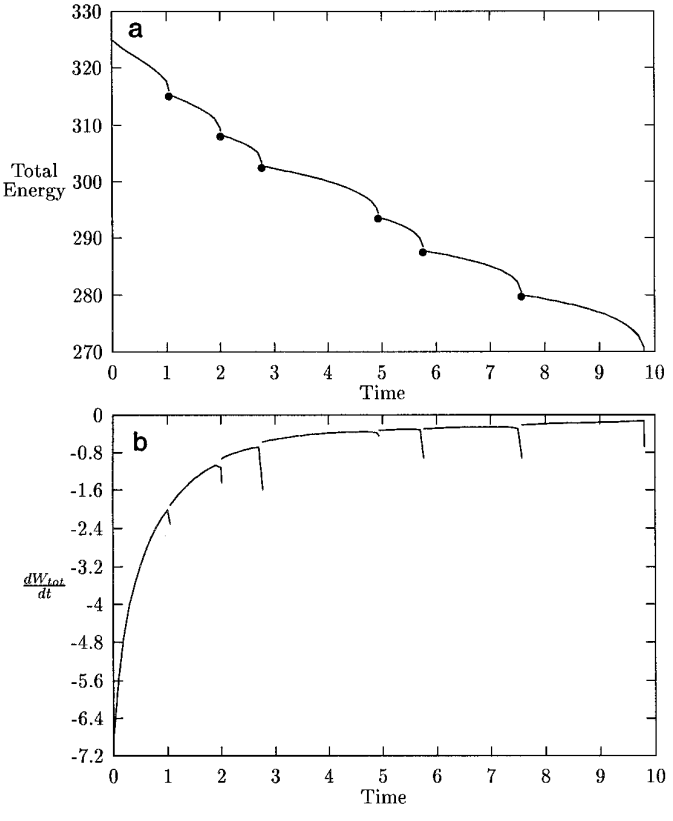

FIG. 24. The total energy and the time derivative of the total energy for the 16-particle computation shown in Fig. 22. In (b), we omit the filled circles to better show the discontinuities.

In future work, we will consider both elastic anisotropy and surface energy anisotropy. We will also implement the fast multipole method [12] to increase computational performance; this will allow us to examine the kinetics of large, multiparticle systems.

ACKNOWLEDGMENTS

It is a pleasure to thank L. Greengard, R. James, R. Kohn, D. Meiron, M. Shelley, T. Shield, and P. Voorhees for interesting discussions. We also thank P. Voorhees for sending us his anisotropic, homogeneous elasticity solver. This work was supported in part by the Minnesota Supercomputer Institute, the McKnight Foundation (J.S.L.), the National Science Foundation through Grants CMS-9503393 (P.H.L.) and DMS-940004310 (J.S.L.). A large part of this work is contained in the Ph.D. thesis of H.-J. Jou in the department of Aerospace Engineering and Mechanics at the University of Minnesota.

APPENDIX A: NONDIMENSIONALIZATION

In this appendix we give the dimensional equations for the diffusion and elasticity problems and present the nondimensionalization that leads to Eqs. (2.1)–(2.4) for diffusion and (2.13)–(2.21) for elasticity. We use tildes to denote dimensional quantities and we drop the tildes for dimensionless quantities.

Consider the diffusion problem first. The dimensional system of equations that applies to this problem is

$$\tilde{\nabla}^2 C^{\mathrm{M}} = 0, \tag{A.1}$$

$$\lim_{\tilde{R}_\infty \to \infty} \int_{\tilde{\Gamma}_\infty} (-\tilde{D}\tilde{\nabla} C^{\mathrm{M}} \cdot n)\, d\tilde{s} = \tilde{j}_\infty, \tag{A.2}$$

$$C^{\mathrm{M}} = C^{\mathrm{MI}} = C_0[1 + \tilde{\zeta}\tilde{\sigma}\tilde{\kappa} + \tilde{\zeta}\tilde{G}^{\mathrm{el}}] \quad \text{on } \tilde{\Gamma}, \tag{A.3}$$

$$\tilde{V} = \left(\frac{\tilde{D}}{C^{\mathrm{P}} - C^{\mathrm{MI}}} \tilde{\nabla} C^{\mathrm{M}} \cdot n \right) \quad \text{on } \tilde{\Gamma}. \tag{A.4}$$

In these equations, C^{M} is the (dimensionless) mole fraction of the diffusing species in the matrix. Recall that we assume diffusion occurs in the matrix phase only. C_0 is a reference composition in the matrix corresponding to a flat two-dimensional interface in the absence of elasticity [34]. The dimensional compositions (mole/length^2) can be found by multiplying C^{M} and C_0 by the alloy density $\tilde{\rho}$ (mole/length^2).[4] Consistent with these definitions, $\tilde{\rho}\tilde{j}_\infty$ (mole/time) is the *total* flux into a fictitious circular outer boundary $\tilde{\Gamma}_\infty$ with radius $\tilde{R}_\infty$ and inward pointing unit normal n. Therefore, $\tilde{j}_\infty$ (length^2/time) corresponds to the time rate of change of the precipitate area. In Eq. (A.3), $\tilde{\kappa}$ (length^{-1}) is the curvature of the interface, $\tilde{\sigma}$ (energy/length) is the surface tension, and $\tilde{G}^{\mathrm{el}}$ (energy/length^2) is the elastic energy density on the interface given by Eq. (A.9) below. The term

$$\tilde{\zeta} = \frac{1 - C^{\mathrm{P}}}{\tilde{\rho}\tilde{k}_g \tilde{T}(C^{\mathrm{P}} - C_0)} \tag{A.5}$$

is a thermodynamic parameter. $\tilde{T}$ is the absolute temperature, C^{P} is the constant composition of the precipitate, and $\tilde{k}_g$ (energy/mole-K) is the gas constant. Therefore $\tilde{\zeta}$ has units length^2/energy. Finally, in Eq. (A.4), $\tilde{V}$ is the normal velocity of the precipitate–matrix interface and $\tilde{D}$ (length^2/time) is the diffusivity.

Our nondimensionalization of the diffusion problem is based on choosing an externally determined length scale $\tilde{L}_0$ for the problem. $\tilde{L}_0$ could, for example, be determined from the initial conditions through an average precipitate radius. We then scale the composition C^{M} in the matrix by

$$U = \frac{C^{\mathrm{M}} - C_0}{\Lambda}, \tag{A.6}$$

where

$$\Lambda = \frac{C_0 \tilde{\zeta}\tilde{\sigma}}{\tilde{L}_0}. \tag{A.7}$$

We also take a time scale

$$\tilde{T} = \frac{\tilde{L}_0^2 (U_{\mathrm{P}} - U_{\mathrm{I}})}{\tilde{D}}, \tag{A.8}$$

where $U_{\mathrm{P}} = (C^{\mathrm{P}} - C_0)/\Lambda$ and $U_{\mathrm{I}} = (C^{\mathrm{MI}} - C_0)/\Lambda$.

We must also choose a nondimensionalization for the elastic energy density $\tilde{G}^{\mathrm{el}}$, where

$$\tilde{G}^{\mathrm{el}} = \tfrac{1}{2}\tilde{\sigma}_{ij}^{\mathrm{P}}(\varepsilon_{ij}^{\mathrm{P}} - \varepsilon_{ij}^{\mathrm{T}}) - \tfrac{1}{2}\tilde{\sigma}_{ij}^{\mathrm{M}}\varepsilon_{ij}^{\mathrm{M}} + \tilde{\sigma}_{ij}^{\mathrm{M}}(\varepsilon_{ij}^{\mathrm{M}} - \varepsilon_{ij}^{\mathrm{P}}) \tag{A.9}$$

is found from the stresses $\tilde{\sigma}_{ij}$ (force/length or energy/length^2) and strains ε_{ij} (dimensionless) on both sides of the precipitate–matrix interface. We scale both $\tilde{G}^{\mathrm{el}}$ and the stresses $\tilde{\sigma}_{ij}$ by the shear modulus of the matrix, $\tilde{\mu}^{\mathrm{M}}$. That is,

$$\sigma_{ij} = \tilde{\sigma}_{ij}/\tilde{\mu}^{\mathrm{M}} \tag{A.10}$$

$$G^{\mathrm{el}} = \tilde{G}^{\mathrm{el}}/\tilde{\mu}^{\mathrm{M}}. \tag{A.11}$$

With this scaling, an isotropic two-phase system can be characterized by the dimensionless Poisson ratios ν^{M} and ν^{P} and by the single dimensionless shear moduli

$$\mu^{\mathrm{P}} = \tilde{\mu}^{\mathrm{P}}/\tilde{\mu}^{\mathrm{M}} \tag{A.12}$$

since

[4] C^M and C_0 could also be taken as a mass fraction, in which case $\tilde{\rho}$ would be mass density.

$$\mu^{\mathrm{M}} = \tilde{\mu}^{\mathrm{M}}/\tilde{\mu}^{\mathrm{M}} \equiv 1. \tag{A.13}$$

Also, the elasticity equations (2.13)–(2.21) follow trivially by scaling the stresses by $\tilde{\mu}^{\mathrm{M}}$ and both the displacements and the gradient operator by $\tilde{L}_0$.

Given these scalings, we define a dimensionless flux

$$J = \frac{\tilde{j}_\infty}{2\pi \tilde{D}\Lambda} \tag{A.14}$$

and the dimensionless quantities

$$\begin{aligned} &\Gamma = \tilde{\Gamma}/L_0, \quad s = \tilde{s}/\tilde{L}_0, \quad R_\infty = \tilde{R}_\infty/\tilde{L}_0, \quad \nabla = \tilde{L}_0\tilde{\nabla}, \\ &\nabla^2 = \tilde{L}_0^2\tilde{\nabla}^2, \quad \kappa = \tilde{L}_0\tilde{\kappa}, \quad V = \tilde{T}\tilde{V}/\tilde{L}_0. \end{aligned} \tag{A.15}$$

We immediately find the dimensionless equations for diffusion,

$$\nabla^2 U = 0, \tag{A.16}$$

$$U = \kappa + ZG^{\mathrm{el}} \quad \text{on } \Gamma, \tag{A.17}$$

$$\lim_{R_\infty \to \infty} \frac{1}{2\pi} \int_{\Gamma_\infty} \nabla U \cdot n \, ds = -J \tag{A.18}$$

$$V = \nabla U \cdot n|_\Gamma = \frac{\partial U}{\partial n}, \tag{A.19}$$

where

$$Z = \tilde{\mu}^{\mathrm{M}} \tilde{L}_0/\tilde{\sigma} \tag{A.20}$$

characterizes the relative contribution of elastic and surface energies to the matrix composition at the interface.

In all our calculations, we choose a prototypical system with a length scale $\tilde{L}_0 = 10^{-7}\ m$, which is consistent with particle sizes observed in [57]. We also take $\tilde{\zeta} = 10^{-8}\ m^2/N$, $\tilde{D} = 10^{-15}\ m^2/s$, $C^{\mathrm{P}} = 0.3$, and $C_0 = 0.1$. Finally, we vary the surface tension $\tilde{\sigma}$, shear modulus $\tilde{\mu}^M$, and far-field flux $\tilde{j}_\infty$ so that $Z = 3000 \sim 15000$ and $J = 0 \sim 100$.

APPENDIX B: FAR-FIELD CONTRIBUTION TO THE ELASTIC ENERGY

In this appendix, we derive an explicit formula for I_∞ given in Section 2.3. I_∞ is the far-field contribution to the elastic energy and is given by

$$I_\infty = \lim_{R_\infty \to \infty} \int_{\Gamma_\infty} t_i^0 \overline{u}_i \, ds', \tag{B.21}$$

where Γ_∞ is a circular outer boundary with radius R_∞ that encloses all the precipitates. Further, $t_i^0 = \sigma_{ij}^0 n_j$ are the components of the far-field traction on Γ_∞ and $\overline{u}_i$ are the components of the displacement on Γ_∞ in the *absence* of applied fields.

Given the solutions u_k and t_k to the integral equations (2.37)–(2.42), $\overline{u}_l$ is given by

$$\begin{aligned} \overline{u}_l(z) = &\int_\Gamma (u_k(s') - u_k^0(s')) t_{lk}^{M*}(z, z(s'))\, ds' \\ &- \int_\Gamma (t_k(s) - t_k^0(s')) u_{lk}^{M*}(z, z(s'))\, ds' \end{aligned} \tag{B.22}$$

for $z \in \Omega^M$, and u_{lk}^{M*} and t_{lk}^{M*} are given by Kelvin's solution with the elastic constants of the matrix. The explicit expression for I_∞ is obtained by letting $z = R_\infty e^{i\alpha}$ and expanding Eq. (B.22) in powers of $1/R_\infty$.

Motivated by the explicit expressions for u_{lk}^{M*} and t_{lk}^{M*}, and letting $v = (v_1, v_2)$ we define the notation

$$D[v]_l(z) = \int_\Gamma v_l(s') \frac{1}{r} \frac{\partial r}{\partial n'} \, ds', \tag{B.23}$$

$$E[v]_l(z) = \int_\Gamma v_k(s') \frac{1}{r} \frac{\partial r}{\partial n'} r_{,l'} r_{,k'} \, ds', \tag{B.24}$$

$$F[v]_l(z) = \int_\Gamma v_k(s') \frac{1}{r} (n_l' r_{,k'} - n_k' r_{,l'}) \, ds', \tag{B.25}$$

$$L[v]_l(z) = \int_\Gamma v_l(s') \log r \, ds', \tag{B.26}$$

$$M[v]_l(z) = \int_\Gamma v_k(s') r_{,l'} r_{,k'} \, ds', \tag{B.27}$$

where $v_j(s') = v_j(z(s'))$ for $j = 1, 2$ and

$$r = |z(s') - z|, \tag{B.28}$$

$$r_{,l'} = \frac{\partial r}{\partial x_l(s')}, \tag{B.29}$$

$$n' = (x_{2,s'}, -x_{1,s'}). \tag{B.30}$$

Using this notation, $\overline{u}_l$ is written as

$$\begin{aligned} \overline{u}_l(z) = &- \frac{1 - 2\nu^M}{4\pi(1 - \nu^M)} D[u - u^0]_l(z) \\ &- \frac{2}{4\pi(1 - \nu^M)} E[u - u^0]_l(z) \\ &- \frac{1 - 2\nu^M}{4\pi(1 - \nu^M)} F[u - u^0]_l(z) \\ &+ \frac{3 - 4\nu^M}{8\pi(1 - \nu^M)} L[t - t^0]_l(z) \\ &- \frac{1}{8\pi(1 - \nu^M)} M[t - t^0]_l(z). \end{aligned} \tag{B.31}$$

Let $z = R_\infty e^{i\alpha}$. We expand each term in Eq. (B.31) in powers of $1/R_\infty$ separately. We explicitly perform the

expansion only for the operator L. The others follow similarly and we state the results below. For any v, we get

$$L[v]_l(z) = \int_\Gamma v_l(s') \log|z(s') - z)|\, ds' \tag{B.32}$$

$$= \int_\Gamma v_l(s') \log|z(s') - R_\infty e^{i\alpha}|\, ds' \tag{B.33}$$

$$= \int_\Gamma v_l(s') \log\left(|R_\infty e^{i\alpha}| \left|1 - \frac{z(s')}{R_\infty e^{i\alpha}}\right|\right) ds' \tag{B.34}$$

$$= \log R_\infty \int_\Gamma v_l(s')\, ds' + \int_\Gamma v_l(s') \log\left|1 - \frac{z(s')}{R_\infty e^{i\alpha}}\right| ds'. \tag{B.35}$$

Now, taking $v_l = t_l - t_l^0$ as in Eq. (B.31), the first integral in Eq. (B.35) vanishes because of mechanical equilibrium. The logarithm is expanded in powers of $1/R_\infty$ using $|z(s')/R_\infty e^{i\alpha}| \ll 1$. We obtain

$$\log\left|1 - \frac{z(s')}{R_\infty e^{i\alpha}}\right| = \mathrm{Re}\left\{\log\left(1 - \frac{z(s')}{R_\infty e^{i\alpha}}\right)\right\} = -\frac{1}{R_\infty}\mathrm{Re}\left\{\frac{z(s')}{e^{i\alpha}}\right\} + O(R_\infty^{-2}). \tag{B.36}$$

Since $\mathrm{Re}\{z(s')/e^{i\alpha}\} = x_1(s')\cos\alpha + x_2(s')\sin\alpha$, we obtain

$$L[t]_l(z) = -\frac{\cos\alpha}{R_\infty}\int_\Gamma x_1(s') t_l(s')\, ds' - \frac{\sin\alpha}{R_\infty}\int_\Gamma x_2(s') t_l(s')\, ds' + O(R_\infty^{-2}) \tag{B.37}$$

with $z = R_\infty e^{i\alpha}$.

Corresponding expansions for D, E, and F are as follows:

$$D[v]_l(z) = -\frac{\cos\alpha}{R_\infty}\int_\Gamma x_{2,s'}(s') v_l(s')\, ds' + \frac{\sin\alpha}{R_\infty}\int_\Gamma x_{1,s'}(s') v_l(s')\, ds' + O(R_\infty^{-2}), \tag{B.38}$$

$$E[v]_l(z) = -\frac{\mathrm{cs}_l\alpha \mathrm{cs}_k\alpha\cos\alpha}{R_\infty}\int_\Gamma x_{2,s'}(s') v_k(s')\, ds' + \frac{\mathrm{cs}_l\alpha \mathrm{cs}_k\alpha\sin\alpha}{R_\infty}\int_\Gamma x_{1,s'}(s') v_k(s)\, ds' + O(R_\infty^{-2}), \tag{B.39}$$

$$F[v]_l(z) = -\frac{\mathrm{cs}_k\alpha}{R_\infty}\int_\Gamma n_l(s') v_k(s')\, ds' + \frac{\mathrm{cs}_l\alpha}{R_\infty}\int_\Gamma n_k(s') v_k(s')\, ds' + O(R_\infty^{-2}). \tag{B.40}$$

Finally, with $v_l = t_l - t_l^0$, M is given by

$$M[v]_l(z) = -\frac{\mathrm{cs}_l\alpha}{R_\infty}\int_\Gamma x_k(s') v_k(s')\, ds' - \frac{\mathrm{cs}_k\alpha}{R_\infty}\int_\Gamma x_l(s') v_k(s')\, ds' + \frac{2\mathrm{cs}_l\alpha\, \mathrm{cs}_k\alpha\cos\alpha}{R_\infty}\int_\Gamma x_1(s') v_k(s')\, ds' + \frac{2\mathrm{cs}_l\alpha \mathrm{cs}_k\alpha\sin\alpha}{R_\infty}\int_\Gamma x_2(s') v_k(s')\, ds' + O(R_\infty^{-2}). \tag{B.41}$$

In the above equations, $z = R_\infty e^{i\alpha}$ and

$$\mathrm{cs}_l\alpha = \begin{cases}\cos\alpha & \text{for } l = 1\\ \sin\alpha & \text{for } l = 2.\end{cases} \tag{B.42}$$

Plugging Eqs. (B.35)–(B.42) into Eq. (B.31) yields the expansion for $\overline{u}_i$. We evaluate the integral $\int_{\Gamma_\infty} t_i^0 \overline{u}_i\, ds'$ by using this expansion, together with the facts that on Γ_∞, $t_i^0 = -\sigma_{ij}^0 \mathrm{cs}_j$ and $ds' = R_\infty\, d\alpha$. Taking the limit as $R_\infty \to \infty$, we obtain

$$\begin{aligned}
I_\infty = &-\frac{\sigma_{ij}^0}{4\pi(1-\nu^M)}[(1-2\nu^M)\,\delta_{ik}B_{j1} + 2A_{ijk1}]\int_\Gamma x_{2,s'}(u_k - u_k^0)\, ds'\\
&+\frac{\sigma_{ij}^0}{4\pi(1-\nu^M)}[(1-2\nu^M)\,\delta_{ik}B_{j2} + 2A_{ijk2}]\int_\Gamma x_{1,s}(u_k - u_k^0)\, ds'\\
&-\frac{\sigma_{ij}^0(1-2\nu^M)}{4\pi(1-\nu^M)}B_{jk}\int_\Gamma n_i(u_k - u_k^0)\, ds'\\
&+\frac{\sigma_{ij}^0(1-2\nu^M)}{4\pi(1-\nu^M)}B_{ij}\int_\Gamma n_k(u_k - u_k^0)\, ds'\\
&+\frac{\sigma_{ij}^0}{8\pi\mu^M(1-\nu^M)}[(3-4\nu^M)\,\delta_{ik}B_{j1} + 2A_{ijk1}]\int_\Gamma x_1(t_k - t_k^0)\, ds'\\
&+\frac{\sigma_{ij}^0}{8\pi\mu^M(1-\nu^M)}[(3-4\nu^M)\,\delta_{ik}B_{j2} + 2A_{ijk2}]\int_\Gamma x_2(t_k - t_k^0)\, ds'\\
&-\frac{\sigma_{ij}^0}{8\pi\mu^M(1-\nu^M)}B_{jk}\int_\Gamma x_i(t_k - t_k^0)\, ds'\\
&-\frac{\sigma_{ij}^0}{8\pi\mu^M(1-\nu^M)}B_{ij}\int_\Gamma x_k(t_k - t_k^0)\, ds',
\end{aligned} \tag{B.43}$$

where

$$B_{ij} = \pi\,\delta_{ij}, \tag{B.44}$$

$$A_{ijkl} = \left(\frac{\pi}{4} + \frac{\pi}{2}\,\delta_{ik}\right)\delta_{kl}\,\delta_{ij} + \frac{\pi}{4}(1-\delta_{ij})(1-\delta_{kl}) \quad \text{(no sum)}. \tag{B.45}$$

In summary, the finite part of the total elastic energy is

$$W_{\text{el}} = \frac{1}{2}\int_\Gamma (t_i u_i^0 - t_i^0 u_i)\, ds' - \frac{1}{2}\int_\Gamma t_i^{\text{T}}(u_i - u_i^{\text{T}})\, ds' - I_\infty \tag{B.46}$$

with I_∞ given in Eq. (B.43).

APPENDIX C: SMALL-SCALE DECOMPOSITION FOR ELASTICITY

In this appendix we present the explicit formulas (in Fourier space) for the small-scale decomposition of the elasticity integral equations presented in Section 3. Recall that the elasticity system (2.37) is given as

$$\mathscr{A}[u,t](\alpha,t) = b(\alpha,t), \tag{C.47}$$

where $u = (u_1, u_2)$, $t = (t_1, t_2)$, and $\mathscr{A} = (\mathscr{A}_{1,1,1}, ..., \mathscr{A}_{1,1,p}, \mathscr{A}_{1,2,1} ..., \mathscr{A}_{1,2,p}, \mathscr{A}_{2,1}, \mathscr{A}_{2,2})$ with the components $\mathscr{A}_{1,l,j}$ coming from the jth precipitate equation and $\mathscr{A}_{2,l}$ from the matrix equation; i.e.,

$$\mathscr{A}_{1,l,j}[u,t] = \tfrac{1}{2}u_l + T^P_{lkj}[u_k] - U^P_{lkj}[t_k] \quad \text{for } l = 1,2;\ j = 1, ..., p, \tag{C.48}$$

$$\mathscr{A}_{2,l}[u,t] = -\tfrac{1}{2}u_l + T^M_{lk}[u_k] - U^M_{lk}[t_k] \quad \text{for } l = 1,2. \tag{C.49}$$

The operators T and U are given by

$$T^\chi_{lkj}[\mu](s,t) = \int_{\Gamma_j} \mu(s') t^{\chi *}_{lk}(z(s), z(s'))\, ds';$$
$$U^\chi_{lkj}[\sigma](s,t) = \int_{\Gamma_j} \sigma(s') u^{\chi *}_{lk}(z(s), z(s'))\, ds', \tag{C.50}$$

where u^χ_{lk} and $t^{\chi *}_{lk}$ are the fundamental solutions given by Eqs. (2.24) with $\chi = P, M$. Further, if $\chi = M$, then Γ_j is replaced by Γ and the additional subscript j is dropped.

In Section 3.2, we showed that

$$\mathscr{A} = \mathscr{L} + R, \tag{C.51}$$

where $R = \mathscr{A} - \mathscr{L}$ is an infinite order smoothing operator and

$$\mathscr{L} = (\mathscr{L}_{1,1,1}, ..., \mathscr{L}_{1,1,p}, \mathscr{L}_{1,2,1}, ..., \mathscr{L}_{1,2,p}, \mathscr{L}_{2,1}, \mathscr{L}_{2,2}) \tag{C.52}$$

with components given by

$$\mathscr{L}_{1,l,j}[u,t] = \tfrac{1}{2}u_l - D^P \pi \varepsilon_{lk3}\mathscr{H}[u_k] - C^P \pi \delta_{lk}\mathscr{H}[\tilde{T}_k], \tag{C.53}$$

$$\mathscr{L}_{2,l}[u,t] = -\tfrac{1}{2}u_l - D^M \pi \varepsilon_{lk3}\mathscr{H}[u_k] - C^M \pi \delta_{lk}\mathscr{H}[\tilde{T}_k], \tag{C.54}$$

where $\tilde{T}_{k,\alpha} = L_j t_k / 2\pi$ and C^χ and D^χ are given in Eqs. (C.59) and (C.60). In Section 3, we also formally inverted $\mathscr{L}$ to get

$$(I + \mathscr{L}^{-1}R)[u,t] = \mathscr{L}^{-1}b. \tag{C.55}$$

In this appendix, we show explicitly how $\mathscr{L}$ is inverted in Fourier space.

Although $\mathscr{L}$ is nonlocal, the Fourier transform diagonalizes each term and, so, $\mathscr{L}$ and $\mathscr{L}^{-1}$ are easily computed in Fourier space. On each interface Γ_j, we define $\hat{\mathscr{L}}(k)$ to be the 4×4 matrix that takes the 4-tuple $(\hat{u}_1(k), \hat{u}_2(k), \hat{t}_1(k), \hat{t}_2(k))$ to $(\hat{\mathscr{L}}_{1,1,j}, \hat{\mathscr{L}}_{1,2,j}, \hat{\mathscr{L}}_{2,1}, \hat{\mathscr{L}}_{2,2})[u, t](k)$. For $k = 0$, we have

$$\hat{\mathscr{L}}(0) = \begin{pmatrix} 1/2 & 0 & 0 & 0 \\ 0 & 1/2 & 0 & 0 \\ -1/2 & 0 & 0 & 0 \\ 0 & -1/2 & 0 & 0 \end{pmatrix}, \tag{C.56}$$

and for $k \geq 1$

$$\hat{\mathscr{L}}(k) = \begin{pmatrix} 1/2 & \pi D^P i & L_j C^P/2k & 0 \\ -\pi D^P i & 1/2 & 0 & L_j C^P/2k \\ -1/2 & \pi D^M i & L_j C^M/2k & 0 \\ -\pi D^M i & -1/2 & 0 & L_j C^M/2k \end{pmatrix}. \tag{C.57}$$

As this is implemented with the discrete Fourier transform of real functions, it is sufficient to consider $k \geq 0$.

Clearly, $\hat{\mathscr{L}}^{-1}(0)$ does not exist. This is because $\mathscr{H}(\text{const}) = 0$. It is easy to modify the small scale decomposition so that $\hat{\mathscr{L}}^{-1}(0)$ *is* invertible, but we found it sufficient to simply solve the $k = 0$ system using the least squares technique.

For $k \geq 1$, direct calculation shows that

$$\hat{\mathscr{L}}^{-1}(k) = \begin{pmatrix} z_1 & iz_2 & z_3 & iz_4 \\ -iz_2 & z_1 & -iz_4 & z_3 \\ z_5 2\pi k/L_j & iz_6 2\pi k/L_j & z_7 2\pi k/L_j & iz_8 2\pi k/L_j \\ -iz_6 2\pi k/L_j & z_5 2\pi k/L_j & -iz_8 2\pi k/L_j & z_7 2\pi k/L_j \end{pmatrix}, \tag{C.58}$$

where

$$z_0 = 2\pi \ln(2),$$
$$z_1 = 2C^M(C^P + C^M)/\det,$$
$$z_2 = 4\pi C^M(C^P D^M - D^P C^M)/\det,$$
$$z_3 = 2C^P(C^P + C^M)/\det,$$
$$z_4 = -4\pi C^P(C^P D^M - D^P C^M)/\det,$$
$$z_5 = [(C^P + C^M)/\pi - 4\pi D^M(C^P D^M - D^P C^M)]/\det,$$
$$z_6 = -2C^M(D^P + D^M)/\det,$$
$$z_7 = [(C^P + C^M)/\pi + 4\pi D^P(C^P D^M - D^P C^M)]/\det,$$
$$z_8 = 2C^P(D^P + D^M)/\det,$$
$$\det = (C^P + C^M)^2 - 4\pi^2(C^P D^M - D^P C^M)^2,$$
$$C^\chi = \frac{4\nu^\chi - 3}{8\pi\mu^\chi(1-\nu^\chi)} \tag{C.59}$$
$$D^\chi = \frac{2\nu^\chi - 1}{4\pi(1-\nu^\chi)} \tag{C.60}$$

are constants that depend on elastic properties only. The invertibility of $\hat{\mathscr{L}}(k)$ is ensured if $(C^P + C^M)^2 - 4\pi^2(C^M D^P - C^P D^M)^2 \neq 0$, which is generally true.

APPENDIX D: LINEAR STABILITY CALCULATION

In this appendix we briefly present the equations that result from a linear analysis about a growing circle of the coupled diffusion–elasticity system given in Section 2. This calculation is done in [33] for a fixed far-field composition rather than a fixed far-field flux. The differences are relatively minor and we refer the reader to [33] for additional details.

Consider the shape

$$r(\alpha, t) = R(t) + \mathrm{Re}\left[\sum_{k=1}^{\infty} b_k(t) e^{ik\alpha}\right],$$

where $|b_k(t)/R(t)| \ll 1$ for all k and all quantities are calculated to first order in b_k/R. We find the normal velocity V of the interface to be

$$V = \dot{r}(\alpha, t) = \dot{R}(t) + \mathrm{Re}\left[\sum_{k=1}^{\infty} \dot{b}_k(t) e^{ik\alpha}\right],$$

where

$$\begin{aligned}
\dot{R} &= a_{00}R + a_{02}b_2 + a_{04}b_4 \\
\dot{b}_1 &= a_{11}b_1 + a_{13}b_3 + a_{15}b_5 \\
\dot{b}_2 &= a_{20}R + a_{22}b_2 + a_{24}b_4 + a_{26}b_6 \\
\dot{b}_3 &= a_{31}b_1 + a_{33}b_3 + a_{35}b_5 + a_{37}b_7 \\
\dot{b}_4 &= a_{40}R + a_{42}b_2 + a_{44}b_4 + a_{46}b_6 + a_{48}b_8 \\
&\vdots \\
\dot{b}_k &= a_{k,k-4}b_{k-4} + a_{k,k-2}b_{k-2} \\
&\quad + a_{k,k}b_k + a_{k,k+2}b_{k+2} + a_{k,k+4}b_{k+4} \\
&\vdots
\end{aligned} \tag{D.61}$$

We write this in matrix form as $\dot{x} = Ax$. The coefficients that appear in Eq. (D.61) are given by

$$a_{00} = J/R^2$$
$$a_{11} = \frac{Z}{R^2}[G_2 - G^*_{n-2} - G_n], \quad \text{where } n = 1,$$
$$a_{22} = \frac{1}{R^2}[J - 6/R + Z(2G_4 - 2G^*_{n-4} - 2G_2)], \quad \text{where } n = 2,$$
$$a_{20} = -2ZG_2/R^2$$
$$a_{40} = -4ZG_4/R^2$$
$$a_{02} = ZG^*_2/R^2$$
$$a_{04} = 2ZG^*_4/R^2$$
$$a_{13} = \frac{Z}{R^2}[2G_4 - G^*_{(n+2)-4} - G_{(n+2)-2} - G^*_2], \quad \text{where } n = 1,$$
$$a_{31} = \frac{Z}{R^2}[2G_4 - 3G^*_{(n-2)-4} - 3G_{(n-2)+2} + G_2], \quad \text{where } n = 3,$$
$$a_{n,n} = \frac{1}{R^2}[(n-1)J - n(n^2-1)/R - nZG_n]$$
$$a_{n,n-4} = \frac{Z}{R^2}[2G_4 - nG_{(n-4)+4}]$$
$$a_{n,n-2} = \frac{Z}{R^2}[G_2 - nG_{(n-2)+2}]$$
$$a_{n,n+2} = \frac{Z}{R^2}[(1-2n)G^*_2 - nG_{(n+2)-2}]$$
$$a_{n,n+4} = \frac{Z}{R^2}[(2-3n)G^*_4 - nG_{(n+4)-4}].$$

The G_i are elastic energy densities computed from G^{el} for the perturbed shape. The superscript "*" indicates complex conjugation. The G_i are $O(n)$ and their formulae are given in [33].

Although it is difficult in general to determine the growth rates explicitly due to the complicated mode coupling, the case with n large simplifies considerably. In this case, the leading term in A is $O(n^3)$ and is given by the surface tension contribution in the diagonal entry $a_{n,n}$. This term is

$$-n(n^2-1)/R. \tag{D.62}$$

Therefore, for large n, the leading eigenvalue of A is given by Eq. (D.62). Thus, the equations for the perturbation amplitudes b_n simplify to

$$\frac{\dot{b}_n = -n(n^2-1)}{R}\, b_n. \tag{D.63}$$

Since n is the perturbation wavenumber, this suggests that explicit numerical integration schemes using general initial data must satisfy the time step stability constraint $\Delta t \leq Ch^3$, where h is the spatial grid size.

REFERENCES

1. T. A. Abinandanan and W. C. Johnson, Coarsening of elastically interacting coherent particles. II. Simulations of preferential coarsening and particle migrations, *Acta Metall.* **41,** 27 (1993).
2. T. A. Abinandanan and W. C. Johnson, Coarsening of elastically interacting coherent particles. I. Theoretical formulation, *Acta Metall.* **41,** 17 (1993).
3. R. Almgren, W. Dai, and V. Hakim, Scaling behavior in an anisotropic Hele–Shaw flow, *Phys. Rev. Lett.* **71,** 3461 (1993).
4. A. J. Ardell and R. B. Nicholson, On the modulated structure of aged Ni–Al alloys, *Acta Metall.* **14,** 1295 (1966).
5. G. Baker and A. Nachbin. Stable methods for vortex sheet motion with surface tension, preprint.
6. J. T. Beale, T. Y. Hou, and J. S. Lowengrub, Convergence of boundary integral methods for water waves, *SIAM J. Num. Anal.* **33,** 1797 (1996).
7. C. A. Brebbia, J. C. F. Telles, and L. C. Wrobel, *Boundary Element Techniques* (Springer-Verlag, Berlin, 1984).
8. R. M. Christensen, *Mechanics of Composite Materials* (Wiley, New York, 1979).
9. J. Conley, M. E. Fine, and J. R. Weertman, Effect of lattice disregistry variation on the late stage phase transformation behavior of precipitate in Ni–Al–Mo alloys, *Acta Metall.* **37,** 1251 (1989).
10. J. D. Eshelby, The elastic energy-momentum tensor, *J. Elasticity* **5,** 321 (1975).
11. A. Greenbaum, L. Greengard, and G. B. McFadden, Laplace's equation and the Dirichlet-Neumann map in multiply connected domains, *J. Comput. Phys.* **105,** 267 (1993).
12. L. Greengard, private communication.
13. L. Greengard and V. Rokhlin, A fast algorithm for particle summations, *J. Comput. Phys.* **73,** 325 (1987).
14. J. Helsing, An integral equation method for elastostatics of periodic composites, preprint.
15. W. Hort and W. C. Johnson, Coarsening of tetragonally misfitting second phase particles domain building and applied stress, in *Solid–Solid Phase Transformations,* edited by W. C. Johnson, J. M. Howe, D. E. Laughlin, and W. A. Soffa (Minerals, Metals, and Materials Society, Pennsylvania, 1994), p. 629.
16. T. Y. Hou, J. S. Lowengrub, and M. J. Shelley, The long-time motion of vortex sheets with surface tension, *Phys. Fluids A,* submitted.
17. T. Y. Hou, J. S. Lowengrub, and M. J. Shelley, Removing the stiffness from interfacial flows with surface tension, *J. Comput. Phys.* **114,** 312 (1994).
18. Y. Jeon, An indirect boundary integral equation method for the biharmonic equation, *SIAM J. Num. Anal.* **34,** 461 (1994).
19. W. C. Johnson, Precipitate shape evolution under applied stress—Thermodynamics and kinetics, *Metall. Trans. A* **18,** 233 (1987).
20. W. C. Johnson, T. A. Abinandanan, and P. W. Voorhees, The coarsening kinetics of two misfitting particles in an anisotropic crystal, *Acta Metall.* **38,** 1349 (1990).
21. W. C. Johnson and J. I. D. Alexander, Interfacial conditions for thermomechanical equilibrium in two-phase crystal, *J. Appl. Phys.* **59,** 2735 (1986).
22. W. C. Johnson, M. B. Berkenpas, and D. E. Laughlin, Precipitate shape transitions during coarsening under uniaxial stress, *Acta Metall.* **36,** 3149 (1988).
23. W. C. Johnson and P. W. Voorhees, Elastically-induced precipitate shape transitions in coherent solids, *Solid State Phenom.* **23,** 87 (1992).
24. W. C. Johnson, P. W. Voorhees, and D. E. Zupon, The effects of elastic stress on the kinetics of ostwald ripening: the two-particle problem, *Metall. Trans. A* **20,** 1175 (1989).
25. H.-J. Jou, P. H. Leo, and J. S. Lowengrub, Numerical simulations of diffusional evolution in inhomogeneous elastic media, in preparation.
26. H.-J. Jou, P. H. Leo, and J. S. Lowengrub, Numerical calculation of precipitate shape evolution in elastic media, in *Solid–Solid Phase Transformations,* edited by W. C. Johnson, J. M. Howe, D. E. Laughlin, and W. A. Soffa (Minerals, Metals and Materials Society, Pennsylvania, 1994), p. 635.
27. A. G. Khachaturyan, S. V. Semenovskaya, and J. W. Morris Jr., Theoretical analysis of strain-induced shape changes in cubic precipitates during coarsening, *Acta Metall.* **36,** 1563 (1988).
28. R. Krasny, A study of singularity formation in a vortex sheet by the point vortex approximation, *J. Fluid Mech.* **167,** 65 (1986).
29. F. C. Larchè and J. W. Cahn, Thermochemical equilibrium of multiphase solids under stress, *Acta Metall.* **26,** 1579 (1978).
30. F. C. Larchè and J. W. Cahn, The interactions of composition and stress in crystalline solids, *Acta Metall.* **33,** 331 (1985).
31. J. K. Lee, A study on coherency strain and precipitate morphology via a discrete atom method, *Metall. Trans. A,* **27,** 1449 (1996).
32. J. K. Lee, Coherency strain analysis via a dicrete atom method, *Scripta Met.* **32,** 559 (1995).
33. P. H. Leo and H.-J. Jou, Shape evolution of an initially circular precipitate growing by diffusion in an applied stress field, *Acta Metall.* **41,** 2271 (1993).
34. P. H. Leo and R. F. Sekerka, The effect of elastic fields on the morphological stability of a precipitate grown from solid solution, *Acta Metall.* **37,** 3139 (1989).
35. P. H. Leo and R. F. Sekerka, The effect of surface stress on crystal–melt and crystal–crystal equilibrium, *Acta Metall.* **37,** 3119 (1989).
36. A. Maheshwari and A. J. Ardell, Morphological evolution of coherent

misfitting precipitates in anisotropic elastic media, *Phys. Rev. Lett.* **70,** 2305 (1993).

37. M. McCormack, A. G. Khatchaturyan, and J. W. Morris, A two-dimensional analysis of the evolution of coherent precipitates in elastic media, *Acta Metall.* **40,** 325 (1992).
38. S. G. Mikhlin, *Integral Equations and Their Applications to Certain Problems in Mechanics, Mathematical Physics, and Technology* (Pergamon, New York, 1957).
39. T. Miyazaki, K. Hakamura, and H. Mori, Experimental and theoretical investigations on morphological changes of *gamma′* precipitates in Ni–Al single crystals during uniaxial stress-annealing, *J. Mater. Sci.* **14,** 1827 (1979).
40. W. Mullins and R. Sekerka, Morphological stability of a particle growing by diffusion or heat flow, *J. Appl. Phys.* **34,** 323 (1963).
41. T. Mura, *Micromechanics of Defects in Solids* (Nijhoff, Boston, 1987).
42. M. Reed and B. Simon, *Functional Analysis,* vol. 1 of *Methods of Modern Mathematical Physics* (Academic Press, New York, 1980).
43. J. Rubenstein and P. Sternberg, Nonlocal reaction–diffusion equations and nucleation, *I.M.A. J. Appl. Math.* **48,** 249 (1992).
44. Y. Saad and M. R. Schultz, GMRES: A generalized minimum residual method for solving nonsymmetric linear systems, *SIAM J. Sci. Stat. Comput.* **7,** 856 (1986).
45. A. Sidi and M. Israeli, Quadrature methods for periodic singular and weakly singular Fredholm integral equations, *J. Sci. Comput.* **3,** 201 (1988).
46. S. Socrate and D. M. Parks, Numerical determination of the elastic driving force for directional coarsening in Ni-superalloys, *Acta Metall.* **41,** 2185 (1993).
47. C. H. Su and P. W. Voorhees, Dynamics of precipitate evolution in elastically stressed solids. I. Inverse coarsening, *Acta Mater.* **44,** 1987 (1996).
48. C. H. Su and P. W. Voorhees, Dynamics of precipitate evolution in elastically stressed solids. II. Particle alignment, *Acta Mater.* **44,** 2001 (1996).
49. M. E. Thompson, C. S. Su, and P. W. Voorhees, The equilibrium shape of a misfitting precipitate, *Acta Metall.* **42,** 2107 (1994).
50. J. K. Tien and S. M. Copley, The effect of uniaxial stress on the periodic morphology of coherent gamma prime precipitates in nickel-base superalloy crystals, *Met. Trans.* **2,** 215 (1971).
51. P. W. Voorhees, The theory of Ostwald ripening, *J. Stat. Phys.* **38,** 231 (1985).
52. P. W. Voorhees, R. F. Boisvert, G. B. McFadden, and D. I. Meiron, Numerical simulation of morphological development during Ostwald ripening, *Acta Metall.* **36,** 207 (1988).
53. P. W. Voorhees, G. B. McFadden, and W. C. Johnson, On the morphological development of second-phase particles in elastically-stressed solids, *Acta Metall.* **40,** 2979 (1992).
54. Y. Wang, L. Q. Chen, and A. G. Khachaturyan, Kinetics of strain-induced morphological transformation in cubic alloys with a miscibility gap, *Acta Metall.* **41,** 279 (1993).
55. Y. Wang, L. Chen, H. Wang, and A. G. Khachaturyan, Shape evolution of a coherent tetragonal precipitate in partially stabilized cubic ZrO_2: A computer simulation, *J. Am. Ceram. Soc.* **76,** 3029 (1993).
56. Y. Wang and A. G. Khachaturyan, Shape instability during precipitate growth in coherent solids, *Acta Metall.* **43,** 1837 (1995).
57. Y. S. Yoo, D. Y. Yoon, and M. F. Henry, The effect of elastic misfit strain on the morphological evolution of γ'-precipitates in a model Ni-base superalloy, *Metals and Mat.* **1,** 47 (1995).